27
1-16-78
25 to NTIS

ORNL/TM-6351

Effects of Alternate Fuels Refractory Test Facility (RTF)

Test 1

Analysis of Selected Aluminosilicate Refractory Bricks, Mortars, and Fibrous Insulations Degraded by Domestic Residual Oil Combustion Products

A. E. Pasto
V. J. Tennery

OAK RIDGE NATIONAL LABORATORY
OPERATED BY UNION CARBIDE CORPORATION · FOR THE DEPARTMENT OF ENERGY

MASTER

DISCLAIMER

Printed in the United States of America. Available from
National Technical Information Service
U.S. Department of Commerce
5285 Port Royal Road, Springfield, Virginia 22161
Price: Printed Copy $6.00; Microfiche $3.00

ORNL/TM-6351

Contract No. W-7405-eng-26

METALS AND CERAMICS DIVISION

EFFECTS OF ALTERNATE FUELS REFRACTORY TEST FACILITY (RTF) TEST 1

ANALYSIS OF SELECTED ALUMINOSILICATE REFRACTORY BRICKS, MORTARS, AND FIBROUS INSULATIONS DEGRADED BY DOMESTIC RESIDUAL OIL COMBUSTION PRODUCTS

A. E. Pasto and V. J. Tennery

Prepared for
Division of Industrial Energy Conservation
Department of Energy

Date Published: June 1978

OAK RIDGE NATIONAL LABORATORY
Oak Ridge, Tennessee 37830
operated by
UNION CARBIDE CORPORATION
for the
DEPARTMENT OF ENERGY

THIS PAGE

WAS INTENTIONALLY

LEFT BLANK

CONTENTS

Page

LIST OF FIGURES v

LIST OF TABLES vii

ABSTRACT 1

INTRODUCTION 2
    General Background 2
    Materials and Test Conditions Selection 3

DESCRIPTION OF RTF 4
    General Considerations 4
    RTF Specifications 5

SPECIMEN SELECTION AND PREPARATION 8
    Selection 8
    Preparation 8
        Archive and Pretest Characterization Specimens 8
        Test Specimens 9

DESCRIPTION OF TEST 12
    Specimen Arrangement 12
    Fuel Oil 12
    Operational Parameters 16

RESULTS OF RTF TEST 1 17
    High Alumina Brick (HAB) 17
    Phosphate-Bonded Mortar (PBM) 33
    Mullite-Based Brick (MBB) 35
    Mullite-Based Mortar (MBM) 48
    High-Alumina Fiber (HAF) 51
    Medium-Alumina Fiber (MAF) Insulation 64

SUMMARY AND INTERPRETATION OF RESULTS 71
    Summary of Results 71
    Interpretation of Results 72

CONCLUSIONS 78

ACKNOWLEDGMENTS 80

REFERENCES 81

THIS PAGE

WAS INTENTIONALLY

LEFT BLANK

LIST OF FIGURES

Figure Page

1 The Refractory Test Facility 6

2 Interior of the RTF Chamber Showing the Burner at the Back, Cooling Tube Penetrations, Sight Port, and Refractory Castable Lining 7

3 High Alumina Brick Specimen, Pretest 10

4 Mullite-Based Brick Specimen, Pretest 11

5 High Alumina Fiber Specimen, Pretest 13

6 Medium Alumina Fiber Specimen, Pretest 14

7 Schematic of Specimen Arrangement, as Viewed From Burner End of Chamber 14

8 Test Panel at Conclusion of 500+ Hr Exposure, Flame-Side . . . 18

9 Test Panel at Conclusion of 500+ Hr Exposure, Back-Side . . . 19

10 HAB and PBM Specimens, Posttest, Flame-Side Face 20

11 HAB and PBM Specimens, Posttest, Back-Side Face 21

12 Flame-Side Face of HAB and PBM Specimens as Removed From Brick and Sectioned for Analysis 22

13 SEM Photographs of Pretest HAB Specimen 27

14 SEM Photographs of Slag Surfaced on HAB Specimen 28

15 SEM Photographs of HAB Specimen Showing Cross Section of Slag Zone 29

16 Polished Section of HAB Specimen, As-Received 31

17 Micrographs of Polished Sections of HAB Specimens After Exposure in RTF Test 1 32

18 SEM Micrographs of PBM Mortar-Brick Joint Pretest 36

19 SEM Photographs of PBM Specimen Posttest 37

20 Micrographs of Polished Sections of PBM Mortar Posttest . . . 38

21 Visual Appearance of MBB Brick and MBM Mortar Specimens After Test 39

Figure		Page
22	SEM Micrographs of Pretest MBB Specimen	43
23	Fracture Face and Slag Surface on MBB Posttest	44
24	Fracture Area Through MBB Brick and Slag	45
25	Optical Micrographs of Pretest MBB Specimen	46
26	Micrographs of MBB and Slag Layer Near Hot Face	47
27	SEM Photographs of Pretest MBM Specimen	49
28	SEM Micrographs of MBM Specimen, Posttest	52
29	Optical Micrograph of Polished Section of Mullite-Based Mortar (MBM) Specimen, Pretest	53
30	Optical Micrographs of MBM Specimen, Posttest	54
31	Visual Appearance of HAF Specimen Posttest	55
32	SEM Micrographs of HAF Specimen Pretest	59
33	SEM Micrographs of Slag Layer in HAF Flame-Side Posttest Specimen	60
34	SEM Micrographs of HAF Specimen, Posttest, Back Side	61
35	SEM Micrographs of HAF Specimen, Back Side Posttest	62
36	Optical Micrographs of Polished Sections Through the HAF Flame-Side Posttest Specimen	63
37	Visual Appearance of MAF Specimen, Posttest	65
38	SEM Micrographs of MAF Specimen, Pretest	68
39	SEM Micrographs of Posttest MAF Specimen	69
40	Optical Micrographs of a Polished Section of Posttest Flame-Side MAF Specimen	70
41	$ZnO-Al_2O_3-SiO_2$ Equilibrium Diagram	75

LIST OF TABLES

Table		Page
1	RTF Test 1 Specimen Designations	8
2	Impurity Content of Domestic Residual Oil Used in RTF Test 1	15
3	Chemical Analysis Results From HAB Specimens	24
4	Results of X-Ray Diffraction Analysis of (HAB) Specimens . . .	25
5	Chemical Analysis Results From PBM Specimens	34
6	Results of X-Ray Diffraction Analysis of PBM Specimens	35
7	Chemical Analysis Results From MBB Specimens	41
8	Results of X-Ray Diffraction Analysis of MBB Specimens	42
9	Chemical Analysis Results From MBM Specimens	50
10	Results of X-Ray Diffraction Analysis of MBM Specimens	51
11	Chemical Analysis Results From HAF Specimens	57
12	Results of X-Ray Diffraction Analysis of HAF Specimens	58
13	Chemical Analysis Results From MAF Specimens	66
14	Results of X-Ray Diffraction Analysis of MAF Specimens	67
15	Summary of Changes in Chemical Constituents of Materials Tested in RTF Test 1	72
16	Summary of Phases Present in Materials Tested in RTF Test 1	73

EFFECTS OF ALTERNATE FUELS REFRACTORY TEST FACILITY (RTF) TEST 1

ANALYSIS OF SELECTED ALUMINOSILICATE REFRACTORY BRICKS, MORTARS, AND FIBROUS INSULATIONS DEGRADED BY DOMESTIC RESIDUAL OIL COMBUSTION PRODUCTS

A. E. Pasto and V. J. Tennery

ABSTRACT

Industrial conversion in the U.S. to alternate fuels from natural gas is presently underway and is anticipated to accelerate rapidly in the next few years. Currently the prime alternate fuels are distillate and residual oils. Conversion to residual oils for high-temperature process heat applications is anticipated to result in accelerated refractory and insulation corrosion and degradation due to reactions between fuel impurities and the ceramic linings of high-temperature equipment. Understanding the nature of such reactions and identification of means for preventing or retarding them will be of considerable assistance to both refractory manufacturers and users in the shift from natural gas to alternate fuels.

This report is the first of a series that will cover analyses of several generic types of refractories and fibrous insulations which have been exposed to residual oil combustion products under well-controlled conditions for times ranging from hundreds to thousands of hours in a Refractory Test Facility (RTF) designed to simulate industrial process heat combustors.

This report presents analyses of aluminosilicate refractory firebricks, mortars, and refractory fibrous insulations following exposure to domestic residual oil combustion for 500 hr at temperatures near 1375°C (2500°F). For all three types of refractory material, compositions with two different Al_2O_3 contents were included. The fuel oil impurities included Fe, Ca, Zn, Ni, Pb, and S in concentrations from tens to hundreds of weight ppm. Some of these impurities reacted with the refractory samples by producing a slag layer on the exposed surfaces followed by penetration into the materials. The more reactive impurities were Fe, Ca, and Zn. These impurity elements formed a glassy phase when in contact with the major silicate phases in the test samples. Reaction products include an Fe-Zn-Al oxide spinel and hercynite ($FeAl_2O_4$). Test samples with considerable porosity reacted more extensively with the slag.

Fibrous insulation materials evaluated in this test underwent extensive shrinkage and other structural changes during the test due to reactions with the fuel oil impurities. Accumulations of slag readily penetrate into the voids between the fibers and result in continual material degradation. The denser refractory bricks and mortars form coherent slag layers by reaction with fuel impurities and exhibit much slower degradation than the insulations.

INTRODUCTION

General Background

A recent assessment[1] of industrial near-term (∿5 year) fuel-usage planning concluded that many energy-intensive industries will of necessity be forced to convert from use of natural gas to distillate and/or residual fuel oils for high-temperature process fuel requirements. Further, this conversion will probably involve heavy use of No. 6 residual oil because of its cost and availability compared with distillate fuels. Residual oils typically contain impurities (heavy metals, alkalies, S, V, etc.) which interact with the refractory and insulation linings exposed to their combustion, a process that leads to shortening of equipment service life through chemical, structural, and phase content alteration. Available literature on pertinent phase-equilibrium studies and some reports on actual equipment failures incurred through use of heavy fuel oils were also assessed. In general, it was found that an insufficient data base existed concerning the nature of these impurity-refractory interactions to permit refractory users to effectively design and specify refractory systems for future equipment. Consequently a program to provide such a data base was developed and organized into three tasks.

1. Analysis of refractory materials (field samples) exposed to alternate fuel combustion in actual industrial furnaces and the reporting of results.
2. Exposure of selected generic refractory materials classes to alternate fuel combustion under controlled conditions of atmosphere, time, temperature, and fuel impurity level.
3. Possibly large-scale industrial tests with alternate fuels using refractory types identified from tasks 1 and 2 as more resistant to deterioration.

The authors were involved in task 1 early in the program because of the many fuel-related failures brought to our attention during our assessment period. Companies experiencing these failures provided us with numerous refractory specimens for analysis. Results of these analyses have been reported, notably at meetings sponsored by the American Ceramic

Society. Publication of the results has also been proceeding rapidly with several reports now available.[2-4] As analyses are completed, further reports will be issued.

A common feature of the refractory field samples is the fact that most of the respondents to this effort are unable to document the actual time-temperature history of the degraded refractory specimens. Further, the source and nature of the residual fuel oil is usually unknown. Interpretation of the chemical, mineralogical, and other analytical results of the used refractories is often complicated due to these unknowns. These deficiencies in the field sample-related data provided justification for proceeding into task 2, the systematic controlled-condition combustor tests. This report is the result of test 1. Future test results will be similarly reported.

Materials and Test Condition Selection

The general philosophy of this portion of the program is to evaluate alternate fuel combustion effects on materials and under firing conditions which closely simulate industrial practice. Suggestions from a wide cross section of firms that use and produce refractory materials were solicited at a meeting whose proceedings were subsequently published.[5]

Because of their wide industrial use, the first generic refractory materials to be studied were aluminosilicate-based refractories and insulations. A test temperature of 1375°C (2500°F) was selected as a compromise between the lower temperature [near 1200-1260°C (2200-2300°F)] common to numerous processes such as steel soaking pits or aluminum reverberatory melting furnaces and the high temperature used in such processes as glass melting. It was anticipated that reaction between the test specimens and fuel impurities would be sufficiently rapid to form a reaction zone of a depth amenable to analysis within several hundred hours. The objective of the analyses was to identify the degradative reactions and from these results to postulate compositional or structural modifications in the materials which would make them more stable with such fuel. It became obvious during this work that results of such analyses obtained at one temperature could only under very limited conditions be used to estimate results at other temperatures.

In many large-scale heating processes, the incoming combustion air is preheated; because this requires expenditure of energy, as little air as possible in excess of stoichiometric is used. However, to ensure complete combustion, burners are normally operated at a slight air excess, and to simulate this practice, we operated the combustor during this test with a small amount of excess air.

Another operating parameter of concern was the time-temperature history. Many processes require frequent thermal cycling, and it was felt that the effect of this cycling should be considered in any test program. The test described herein included several temperature cycles.

DESCRIPTION OF RTF

General Considerations

Ideally selected instrumented specimens should be placed in an operating, full-scale industrial furnace so that test conditions could perfectly match use conditions. However, this approach is impractical for many reasons, and therefore investigators in refractory-slag interaction research ordinarily perform bench-scale experiments such as placing slag (ash) in a hole drilled into a brick and subsequently heat treating the specimen in a controlled atmosphere. This procedure, while perhaps useful as a screening test to quickly identify the least reactive materials, does not always yield results comparable to those obtained from actual service specimens.

The authors concluded that a procedure involving exposing refractory specimens to a suitable combustion atmosphere under controlled conditions would best simulate actual industrial use conditions. The apparatus consisted of a furnace chamber with an oil burner, associated piping, an oil storage tank, and controls. Contacts with manufacturers of oil burners quickly indicated that the chamber would not be small since the smallest No. 6 oil burners available at the time released a minimum of about 2.9×10^5 W (1×10^6 Btu/hr).

RTF Specifications

A conceptual design of the RTF was described in a specification, and vendor solicitation took place in April 1976. The unit was ordered in July, the equipment was delivered in March 1977, and the unit became operational in mid April 1977.

The RTF is shown in Fig. 1. It consists of a carbon steel-shell furnace chamber 2.7 m (9 ft) long by 2 m (6-1/2 ft) OD. The lining consists of 75 mm (3 in.) of 94+% Al_2O_3 refractory castable backed with 150 mm (6 in.) of a lightweight insulating castable refractory. The chamber interior dimensions are about 1.2 m (4 ft) diam by 2.3 m (7-1/2 ft) long. Provision is made to allow water cooling of the interior via metal tubes connected to an exterior-mounted manifold. Penetrations for these tubes are shown in Figs. 1 and 2 surrounding the door opening. A John Zink Co. FFC-10-PL burner assembly is mounted on the back end of the chamber as shown in Fig. 2. This burner provides a flat flame configuration with gas or fuel oils. The heat release rate is variable from 3.2×10^5 W (1.1×10^6 Btu/hr) up to 1.2×10^6 W (4.0×10^6 Btu/hr) depending on air and oil pressure.

Mounted next to the furnace chamber and shown in Fig. 1 is a heated, 7.6-m^3 (2000-gal) oil storage tank. The system also contains a control panel, oil pump, and piping to feed the burner. Combustion air is provided by the blower mounted above the furnace chamber while atomizing air is provided from a laboratory compressed air supply line.

Sight ports are located on top, both sides, and both ends of the chamber. Thermocouple feedthrough penetrations are located on the side and bottom. A flue gas monitor penetration is provided in the stack.

With this system we can heat to a given temperature with natural gas/air combustion and switch to oil/air as desired. With interior cooling, the chamber temperature can be controlled at the desired temperature of 1375°C (2500°F) quite easily. We have attained a maximum temperature of 1550°C (2820°F) in tests. The minimum temperature obtainable is limited by the flame instability which occurs at low fuel flow rates with residual oil.

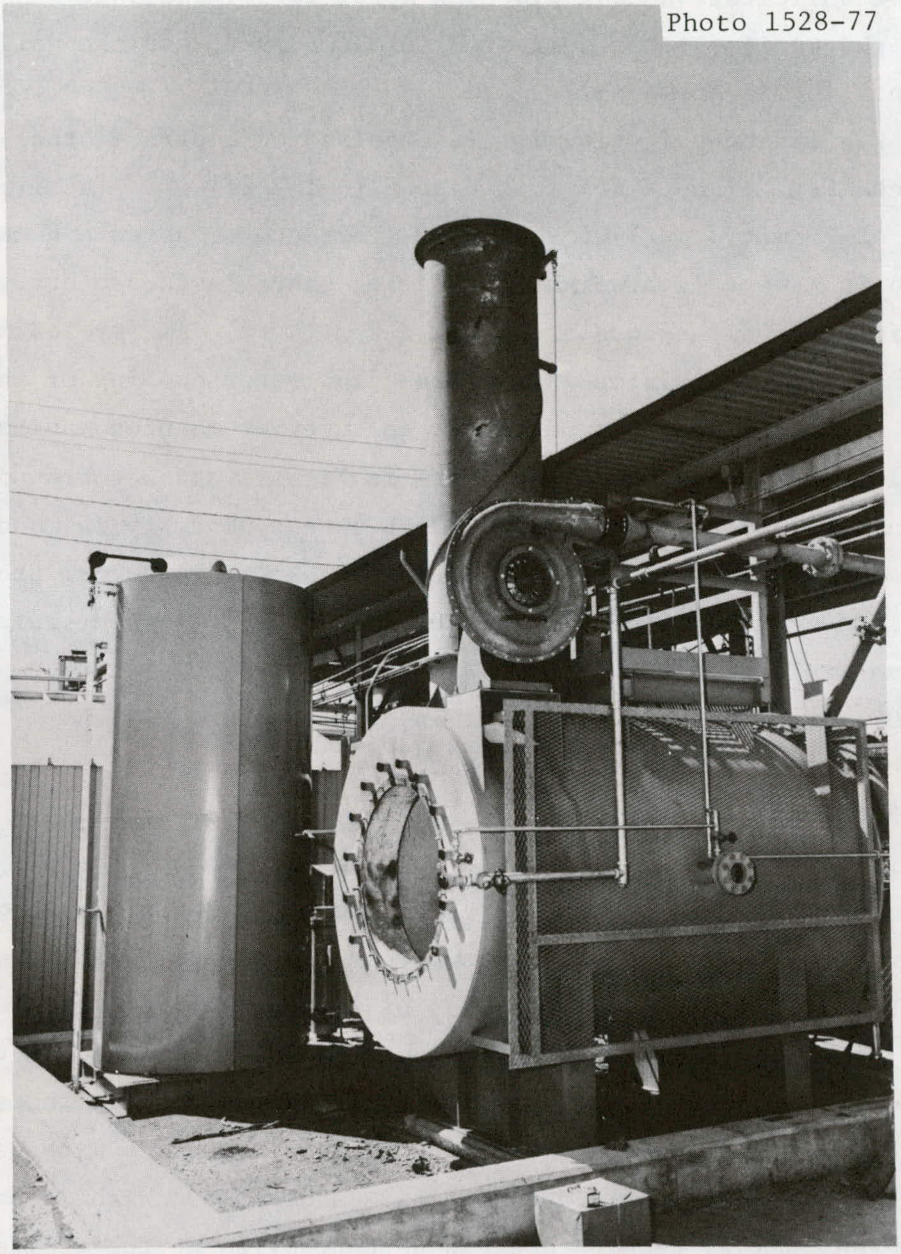

Photo 1528-77

Fig. 1. The Refractory Test Facility (RTF). The oil tank, chamber, stack, and air blower are visible.

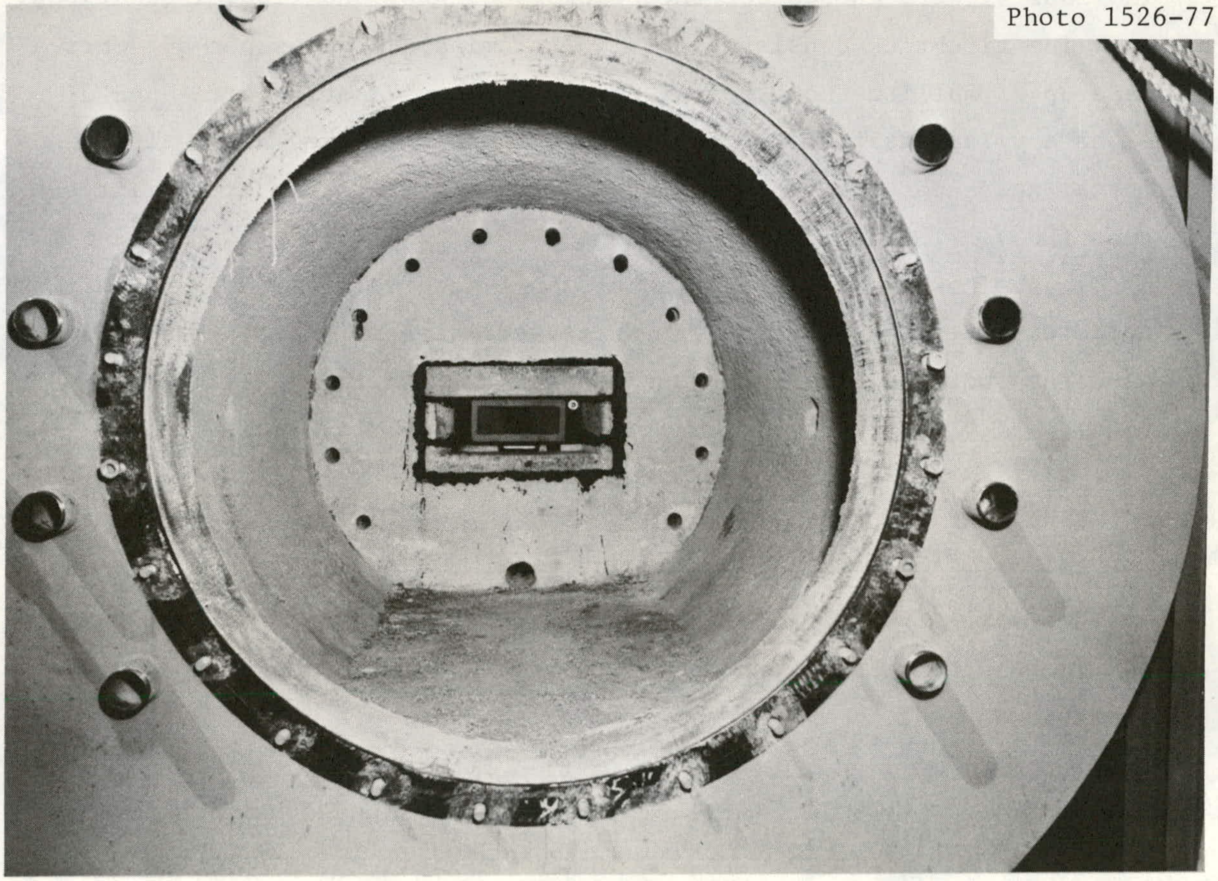

Photo 1526-77

Fig. 2. Interior of the RTF Chamber Showing the Burner at the Back, Cooling Tube Penetrations, Sight Port, and Refractory Castable Lining.

SPECIMEN SELECTION AND PREPARATION

Selection

As mentioned previously, test 1 includes selected aluminosilicate refractories and insulations. Since the previous assessment[1] indicated anticipated better performance with increasing alumina content in aluminosilicate-type material, two levels of Al_2O_3 content widely used in industry were chosen for the bricks, mortars, and fiber insulations.

The firebrick consisted of a 45% alumina content super-duty brick made up of mullite and a 90% Al_2O_3 brick composed of mullite-bonded alpha alumina grain. The mortars were a mullite-based air-setting mortar and a phosphate-bonded air-setting mortar of higher alumina content (80%). The fibrous insulations consisted of 55% Al_2O_3 and a 95% Al_2O_3 aluminosilicate fiber blanket. All materials were purchased from commercial refractory vendors. Characterization of these materials is described more fully in the test results section.

Preparation

Archive and Pretest Characterization Specimens

To simplify the specimen descriptions in the text to follow, the specimens have been given the three-letter abbreviated designations shown in Table 1.

Table 1. RTF Test 1 Specimen Designations

Specimen Type	Distinguishing Phase Characteristic	Designation
Brick	90% Al_2O_3, alumina grains	HAB
Brick	45% Al_2O_3, mullite-based	MBB
Mortar	High alumina, phosphate-bonded	PBM
Mortar	Mullite-based	MBM
Fiber Blanket	95% Al_2O_3	HAF
Fiber Blanket	55% Al_2O_3	MAF

Characterization and archive specimens of the brick and mortar were prepared as follows:

1. Slabs of each brick were sliced off with a diamond cutting wheel.
2. Several of these were crushed to -100 mesh (<150 μm) for chemical and x-ray diffraction analysis.
3. Other brick samples were joined together with appropriate mortars according to mortar preparation instructions supplied by the manufacturer and then dried and fired in air at 1375°C (2500°F) for periods up to 115 hr to evaluate phase and structural changes in a clean atmosphere. These were then analyzed by ceramographic, microprobe, and scanning electron microscopic (SEM) techniques.
4. Slabs of mortar were cast, dried, and fired along with the brick slabs. These were also analyzed by chemical and x-ray diffraction analyses.

The brick slab specimens of HAB were joined with mortar PBM, while brick slab specimens MBB were joined with mortar MBM in step 3.

The fiber specimens were prepared as follows:

1. A 2.5 cm-wide (1 in.) strip was cut from the roll blanket and cut into cubes.
2. Some of these cubes were stored as archives, and some submitted for x-ray diffraction and SEM analysis.
3. Others were heat treated for long times in air with the brick slabs. Some of these were subsequently submitted for x-ray diffraction and SEM evaluation, chemical analysis, or ceramographic or microprobe examination. Others were retained as archives.

Test Specimens

Two standard size brick of type HAB were joined together with a thin layer of PBM, dried and fired 8 hr at 1375°C (2500°F) in air. The resulting composite specimen is shown in Fig. 3. Similarly, two standard MBB brick were joined with MBM mortar (Fig. 4).

The fiber specimens were prepared as follows. Strips 11.4 cm long (4.5 in.) by 2.5 cm thick (1 in.) by 2.5 cm wide (1 in.) were cut from

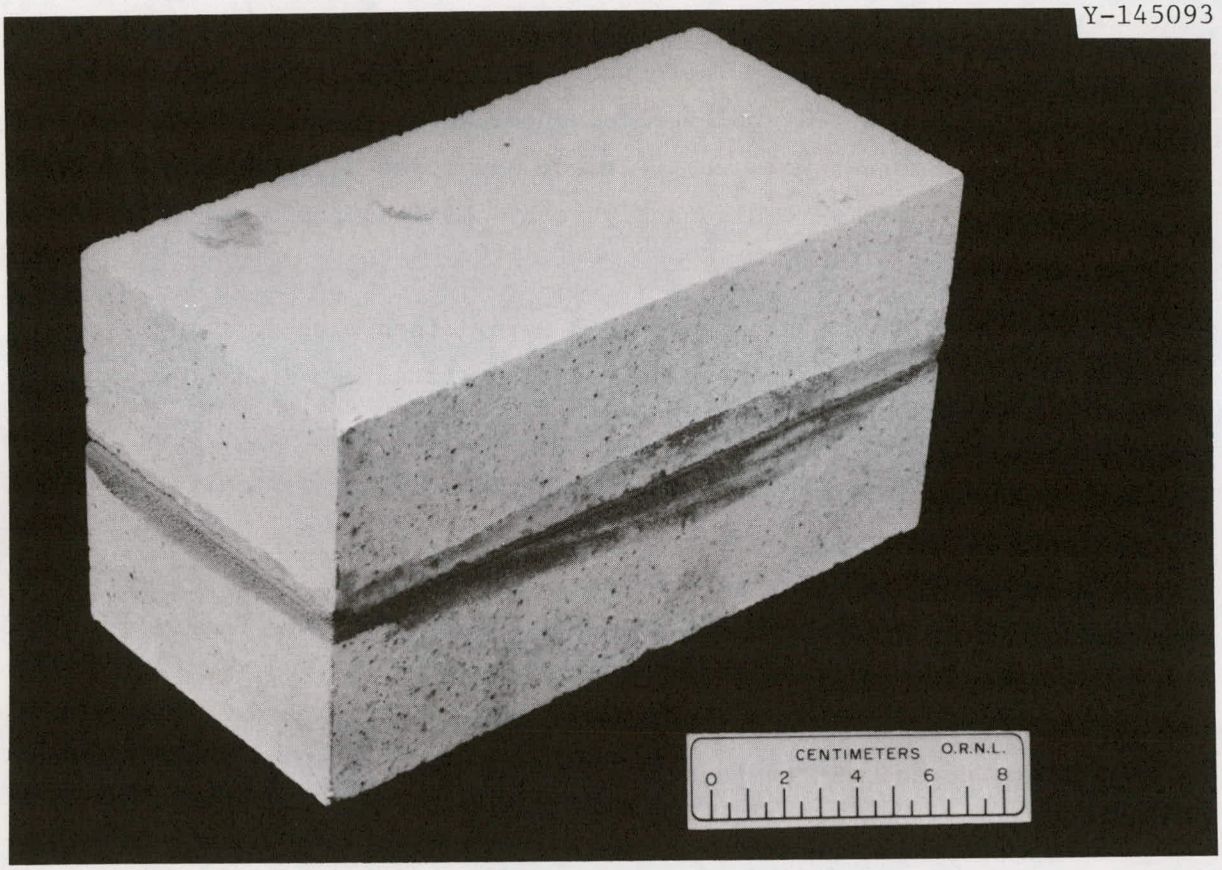
Y-145093

Fig. 3. High Alumina Brick Specimens, Pretest.

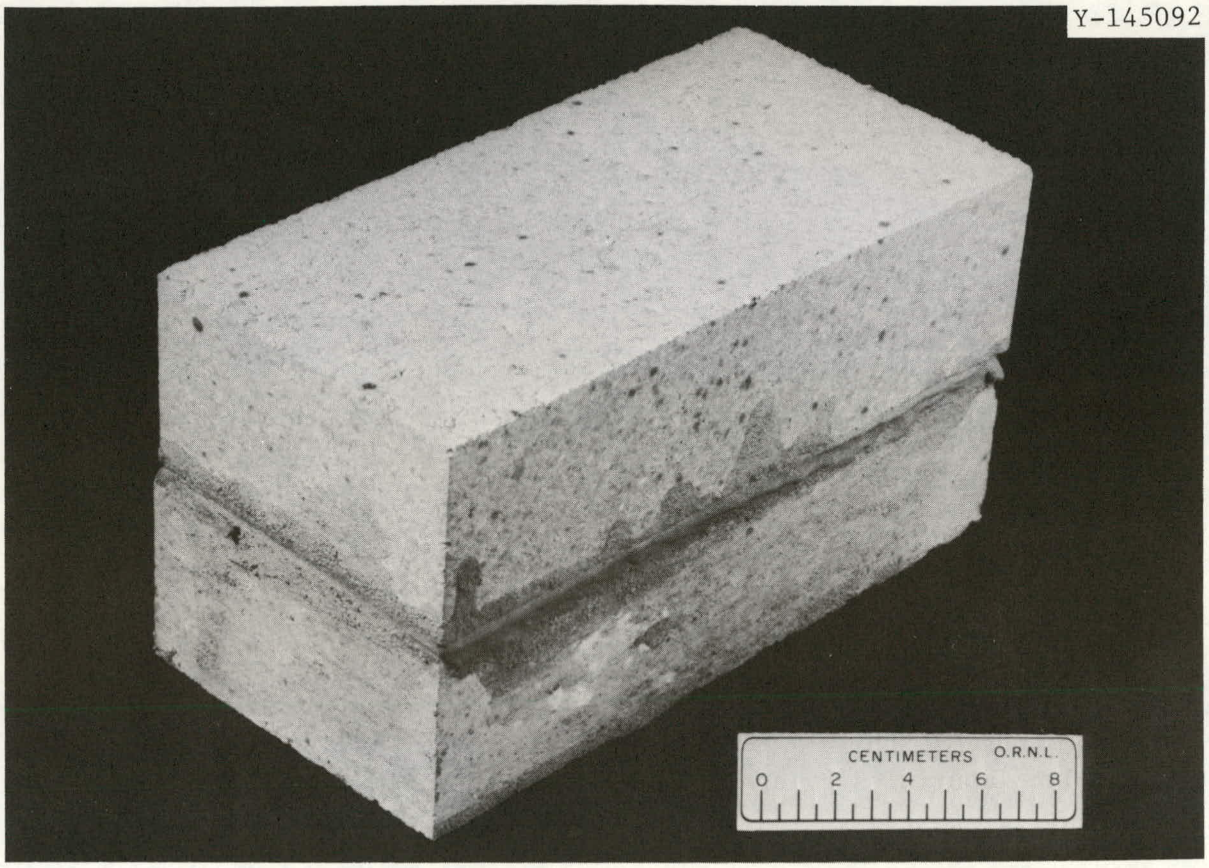

Fig. 4. Mullite-Based Brick Specimens, Pretest.

the roll blanket and joined to a commercial 99% Al_2O_3 standard brick with an air-setting ZrO_2-base cement.[*] This cement was chosen since it would be unlikely to react with the fibers at the test temperatures and would form a strong bond. Fiber strips covered both 11.4-cm (4.5-in.) by 23-cm (9-in.) faces of the bricks. These specimens are shown in Figs. 5 and 6.

DESCRIPTION OF TEST

Specimen Arrangement

To support the test specimens, a platform of 99% Al_2O_3 brick was assembled 1.8 m (6 ft) from the burner along its axis to a height which was just below the central axis of the chamber. The brick and mortar composite specimens were placed on this platform adjacent to each other. The fiber specimens were then placed on top of these so that all specimens had an area facing the burner and an equal area facing away from the flame. The test specimen arrangement is shown schematically in Fig. 7.

Fuel Oil

A domestic No. 6 residual fuel oil was purchased locally,[†] which had been refined from a Kentucky crude oil. Samples delivered on separate dates were drawn from the tank and analyzed for sulfur and metallic impurities by spark source mass spectrometry (SSMS) and atomic absorption spectroscopy. Results are given in Table 2. The elemental values for the SSMS technique are expected to be in the range of one-half to two times the true value based on other analytical experience.

---

[*] Zircar Zirconia Cement, an Y_2O_3-stabilized zirconia cement, Zircar Products, Inc., Florida, N.Y.

[†] Petroleum Recycling Corporation, Knoxville, Tenn.

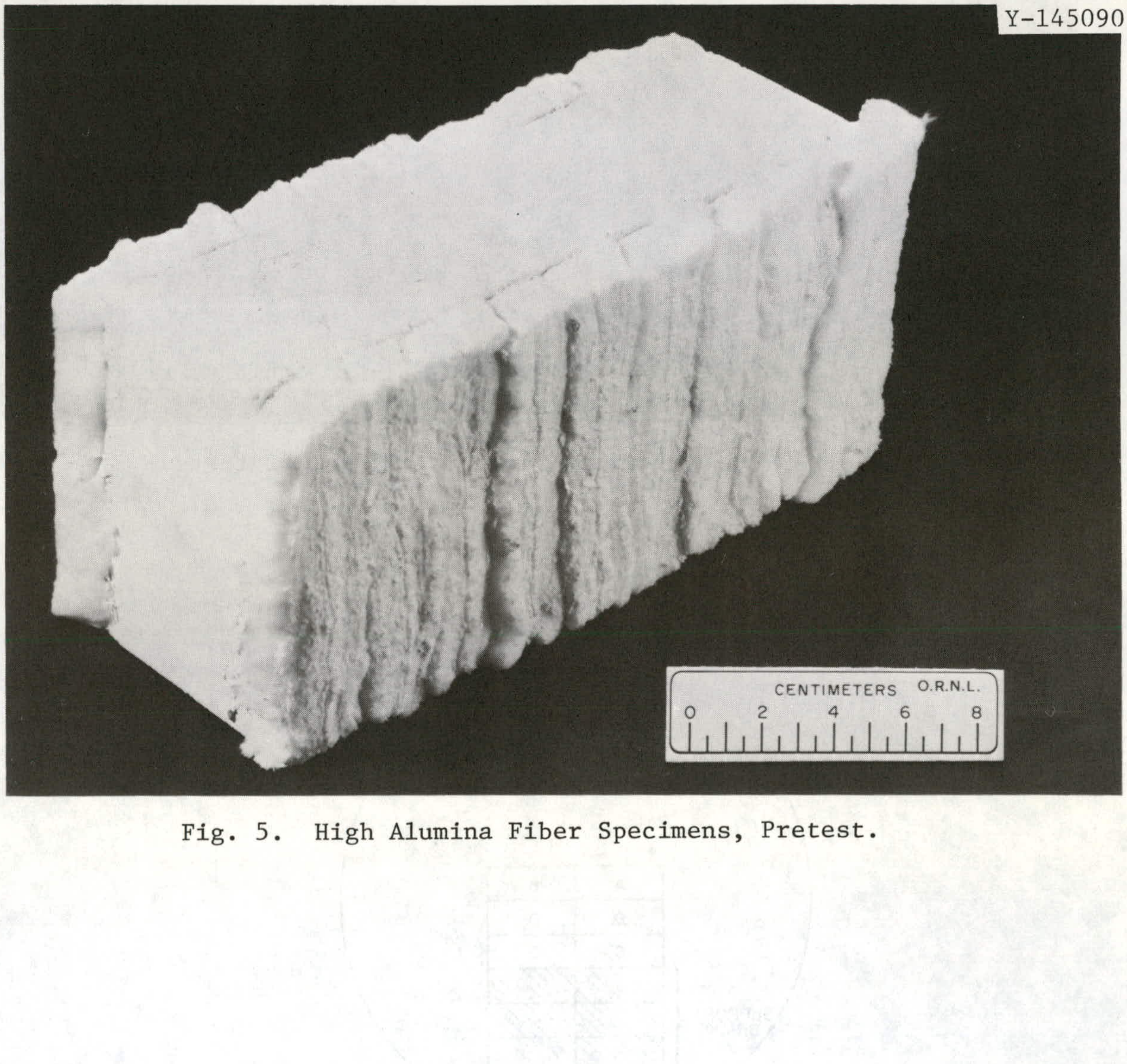

Fig. 5. High Alumina Fiber Specimens, Pretest.

Y-145091

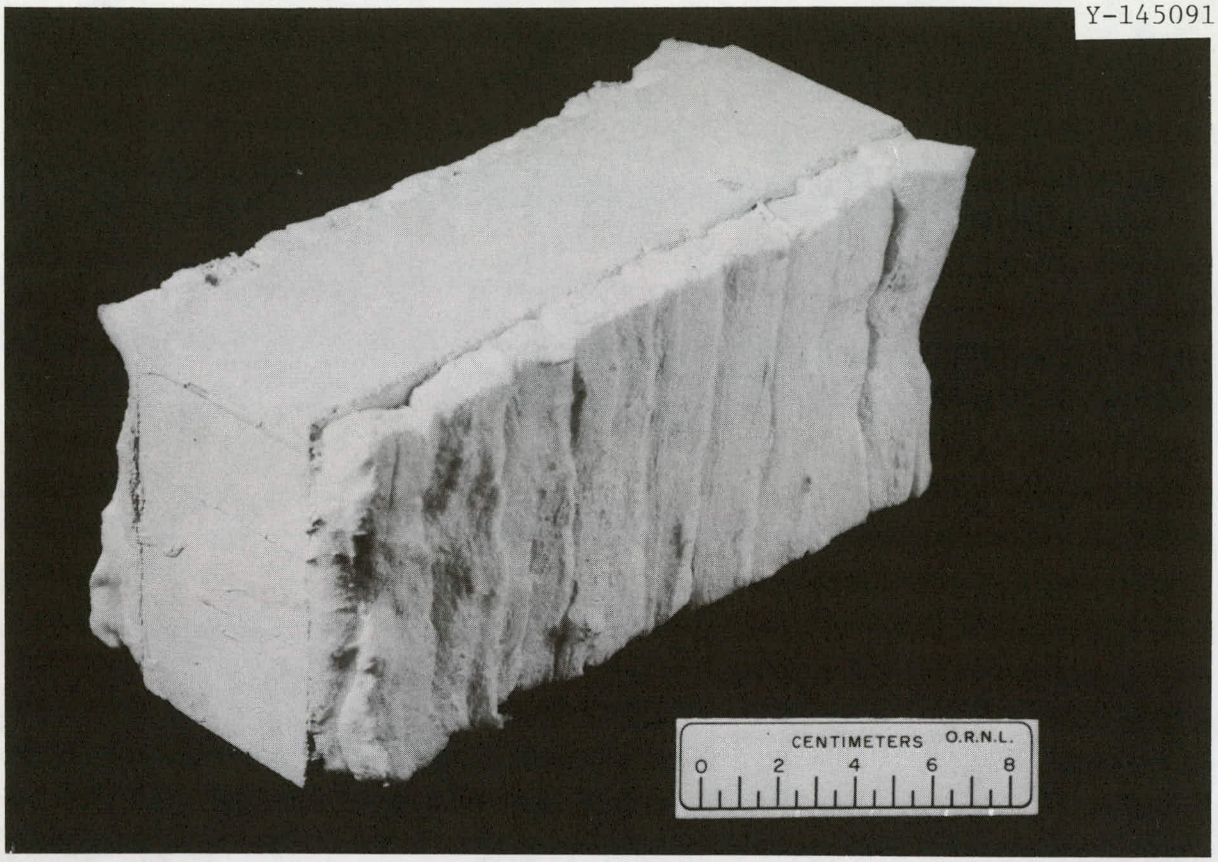

Fig. 6. Medium Alumina Fiber Specimens, Pretest.

ORNL-DWG 78-6279

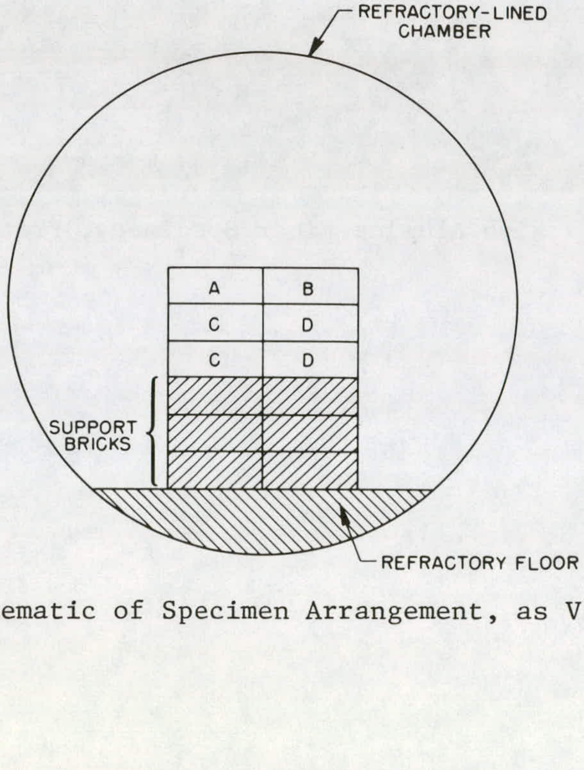

Fig. 7. Schematic of Specimen Arrangement, as Viewed from Burner End of Chamber.

Table 2. Impurity Content of Domestic Residual Oil Used in RTF Test 1

	Concentration (wt ppm)		
Element	SSMS[a] Sample 1	SSMS Sample 2	AAS[b] Sample 3
Si	20	20	300
Ca	3	15	520
Fe	30	100	170
Zn	20	250	400
Ni	1	20	12
V	20	2	50
S	⩾500	⩾500	12,100
Pb	20	500	2,200
Na	25	25	57
Al	20	3	ND[c]
Ba	⩾2	50	ND[c]
Co		⩾0.2	ND[c]
Cr	⩾2	5	ND[c]
Mg	5	20	ND[c]
P	5	20	470
Sb		10	ND[c]
Sn		10	ND[c]
Sr	0.5	2	ND[c]
Ti	0.3	0.7	ND[c]

[a] SSMS — Spark source mass spectrometric method.

[b] AAS — Atomic absorption spectroscopic method.

[c] ND — Not determined.

Values for the atomic absorption spectroscopic (AAS) technique are considered accurate to ±5%.

It is apparent from the reported impurity levels that this oil is much different from fuels derived from Arabian, Venzuelan, or Caribbean crudes, which are usually higher in sulfur, vanadium, and sodium.[1,6,7] Impurity contents of crude oils vary widely with location of source since these impurities derive both from the rock strata associated with the crude and also the organic matter from which the petroleum is formed. The Al, Ca, Fe, Mg, Si, and Na elements are associated with rock strata, while V, Ni, and Zn may be organically derived. Oils are often blended at refineries and foreign crudes may frequently be blended with domestic oils. For this reason, it is extremely important for a residual oil user to obtain analyses of this fuel prior to use so that oils containing high levels of deleterious impurities can be rejected.

Operational Parameters

Thermocouples were inserted into the test panel so that one was located directly below each of the test brick types with the junction about 1 mm back from the hot face. Other thermocouples were placed in the stack and on the furnace floor and walls to provide additional information on the temperature distribution within the chamber during the test. All thermocouples in the specimen stack indicated temperatures within 10°C (18°F) of each other. The floor temperature was lower while the flue gas was considerably hotter. During this test, thermocouple outputs were continuously recorded with a strip chart recorder. The atmosphere within the chamber was monitored by a flue gas analyzer,[*] which gave the %O_2 and combustibles in the stack gas. The atmosphere was maintained hyper-stoichiometric in oxygen, between 4 and 8% excess, and typically at 6%.

Other parameters monitored were oil line pressure and temperature, fuel flow rate, atomizing air pressure, and flow rate.

---

[*] Teledyne Model 980 Portable Flue Gas Analyzer, Teledyne Analytical Instruments, San Gabriel, Calif.

The run started on 19 April 1977. Timekeeping commenced and was recorded when the temperature sensed by the specimen thermocouples exceeded 1300°C (2370°F). When a cool-down cycle was in progress, the oil flow was stopped after reaching about 700°C (1290°F) and natural gas was burned with air to keep the chamber at 500-700°C (930-1290°F) and in an oxidizing condition. This procedure was necessary to provide for rapid startup on the following cycle. Also, the oil burner was unstable at these lower temperatures.

The test was largely uneventful. A total of 521 hr at temperatures of 1300-1400°C (2370-2550°F) was accumulated for the specimens. Sixteen cycles of heating-holding-cooling were experienced by the samples.

The experiment was terminated 16 June 1977. The panel at this time is shown in Fig. 8 (flame-side) and Fig. 9 (back-side).

RESULTS OF RTF TEST 1

High Alumina Brick (HAB)

The posttest specimens are illustrated in Figs. 10 and 11. Cracks which apparently originated at the hot face penetrated into the specimens (Fig. 11). The major crack is continuous through the mortar layer. These cracks are apparently due to the thermal cycling aspect of the test as opposed to stress generated by the formation of low density phases due to impurity reactions. A planar separation between the mortar and brick is shown in Fig. 11. This separation was complete and extended through the specimen through the entire joint.

The color of the brick has changed from white to bluish-black on the front surface and to a lighter blue on the back side.

The major faces of the specimens were sectioned with a diamond saw, yielding a plate roughly 6 mm thick (0.25 in.). This was further cut into pieces for analysis as illustrated in Fig. 12. Selected portions of reacted brick and mortar were crushed for chemical and x-ray diffraction analysis. Other specimen pieces were analyzed by SEM, ceramography, and electron microprobe analysis.

Photo 2969-77

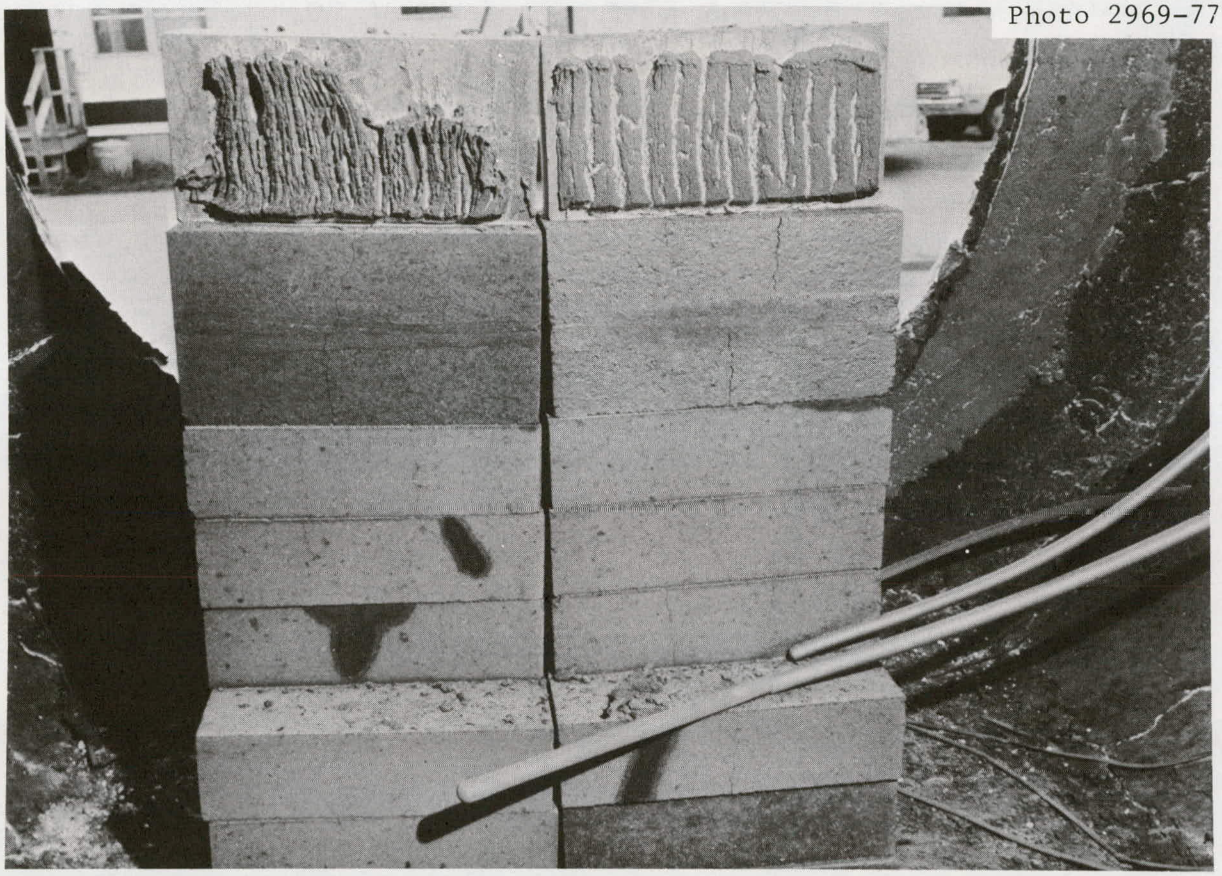

Fig. 8. Test Panel at Conclusion of 500+ Hour Exposure, Flame-Side.


Photo 2970-77

Fig. 9. Test Panel at Conclusion of 500+ Hour Exposure. Back-side.

Y-146878

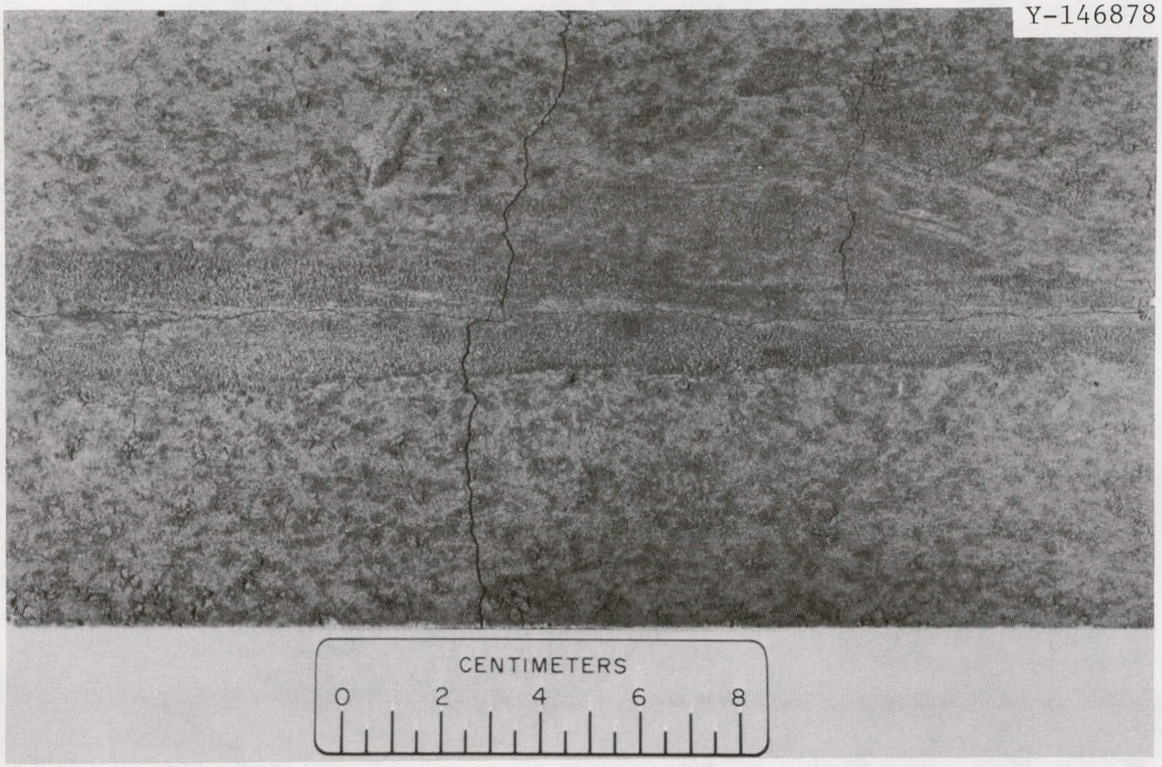

Fig. 10. HAB and PBM Specimens, Post-Test, Flame-Side Face.

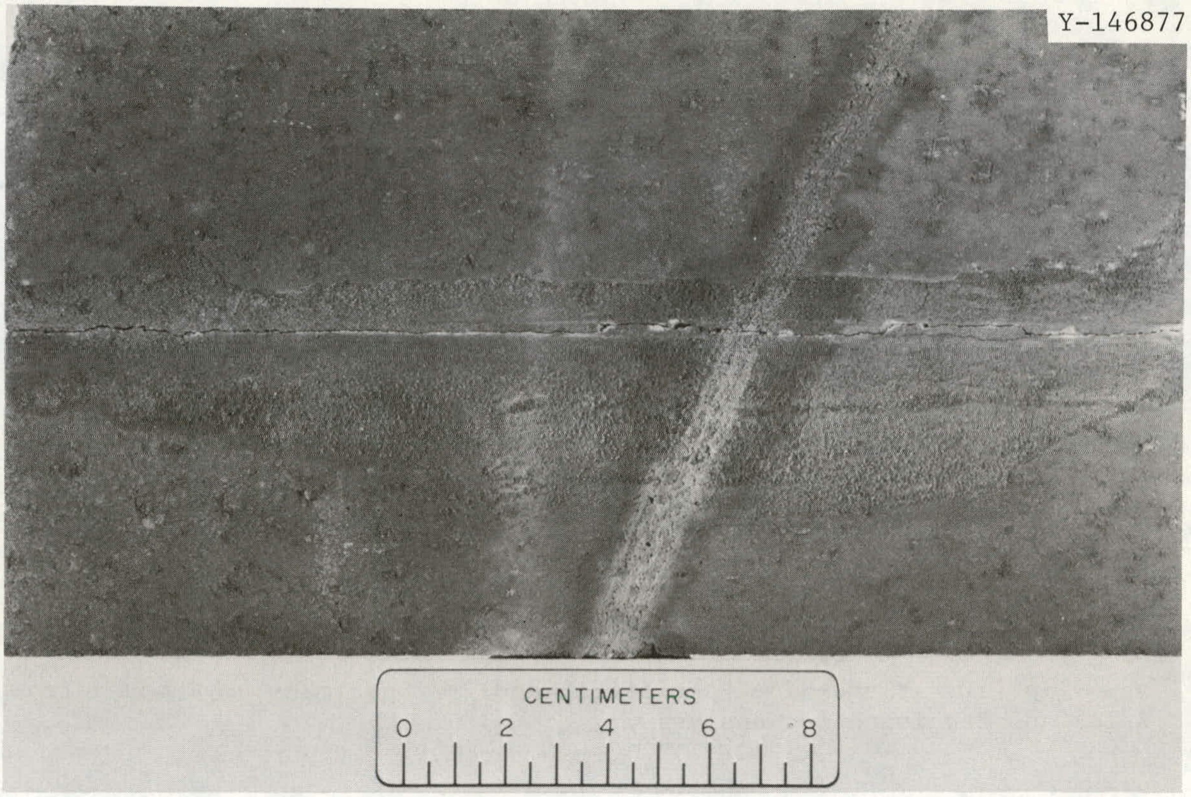

Fig. 11. HAB and PBM Specimens, Post-Test, Back-Side Face.

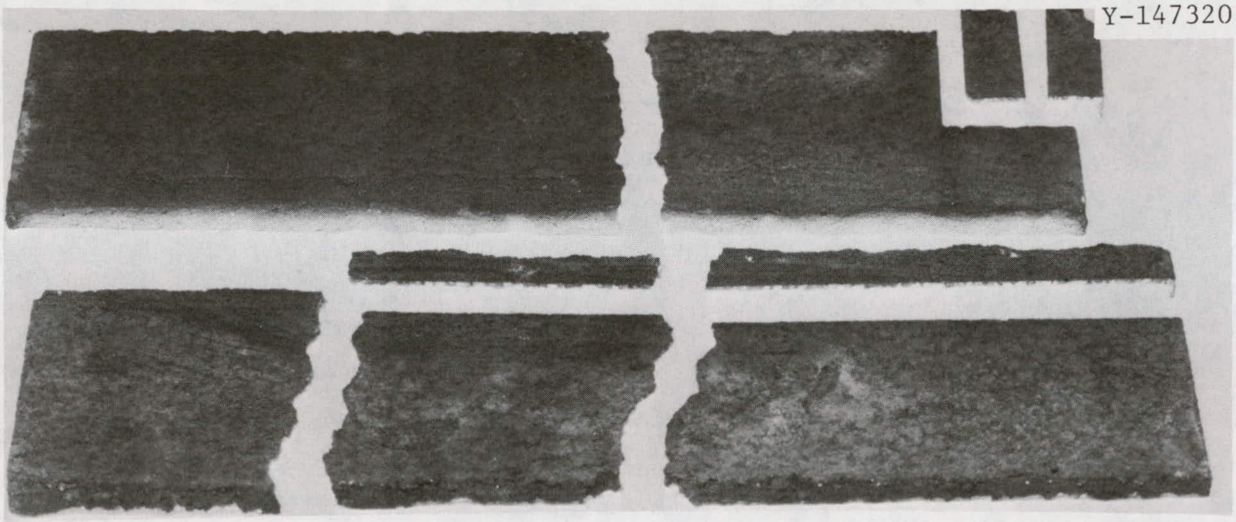

Fig. 12. Flame-Side Face of HAB and PBM Specimens as Removed from Brick and Sectioned for Analysis.

Chemical analyses of the HAB specimen as received and posttest are presented in Table 3. The analysis was performed by a combination of wet-chemistry and emission spectroscopy. The accuracy and precision for these analyses are not available because only one sample of each type was analyzed. Further, the posttest values include a significant portion of unaltered brick material due to the limited extent of the reaction zone following the 500 hr test. Thus, the chemical analysis results serve as general guides to the nature of the impurity pickup in the refractories and do not represent the exact composition of the reaction zone. This statement holds for all subsequent chemical analysis data reported. Pretest specimens were analyzed simultaneously with the posttest specimens by the same laboratory. The data indicate significant increases in Fe, Si, Ca, Zn, and Ni contents of the posttest specimens compared with the as-received brick. This was not unexpected because of the impurity content of the fuel given in Table 2. Also apparent is the greater concentration of impurities in the flame-side face compared with the more protected (back) side. Later discussion of the relative flux of impurities from the oil incident on these sample faces will explain this observation.

Identification of the crystalline phases of the reaction zone was determined by use of x-ray diffraction. Phases identified in the HAB samples are presented in Table 4. The as-received brick consists largely of corundum and mullite. No free silica or other crystalline phases were detected. This technique has a detection limit of the order of 5 wt %.

The difference in major phase content for as-received and posttest specimens is a spinel phase in the reaction zone. More definitive information about this phase was obtained by scraping the surface of the brick originally oriented toward the burner, physically separating dark well-defined crystals from the mass under a stereoscopic microscope. These were analyzed by the Debye-Scherrer x-ray technique. They produced a diffraction pattern that was indexed as belonging to a cubic crystal with lattice parameter of 0.813 to 0.816 nm (8.13 to 8.16 Å). The crystals were observed to be attracted to a magnet. Thus, we concluded that this material was an iron-bearing spinel. Hercynite ($FeAl_2O_4$) has

Table 3. Chemical Analysis Results From HAB Specimens

Element (as oxide equiv.)	Content (wt %)		
	As-Received	Back-Side	Front-Side
L.O.I.	0.05	0.05	0.23
Al_2O_3	90.15	85.89	81.74
Fe_2O_3	0.08	0.70	1.85
SiO_2	9.05	10.80	11.20
CaO	0.06	0.21	1.01
TiO_2	0.34	0.45	0.77
P_2O_5	0.05	0.09	0.25
Na_2O	0.10	0.30	0.20
MgO	0.001	0.001	0.14
MnO	0.010	0.05	0.08
ZnO	0.001	1.0	2.0
NiO	0.003	0.30	0.50
Cr_2O_3	0.03	0.05	0.10
CuO	0.01	0.01	0.01
PbO	0.001	0.01	0.01
MoO_3	0.001[a]	0.001[a]	0.001[a]
V_2O_5	0.001[a]	0.001[a]	0.002
B_2O_3	0.003	0.003	0.005
BaO	0.001[a]	0.001[a]	0.002
Ag_2O	0.003	0.003	0.003
K_2O	0.07	0.09	0.10
Total	100.02	100.01	100.20

[a] Not detected. Number is minimum limit of detection.

Table 4. Results of X-Ray Diffraction Analysis of (HAB) Specimens

	Phases Present and Amounts		
Specimen Type	Major	Medium	Minor
As-Received	α-Al_2O_3	Mullite	
Back-Side, Posttest	α-Al_2O_3	Mullite	Spinel
Front-Side, Posttest	α-Al_2O_3	Mullite	Spinel, Others

a lattice spacing of 0.815 nm (8.15 Å), and based on this evidence, we concluded that the spinel phase is hercynite. However, ceramographic, SEM, and microprobe evidence discussed later will show that hercynite is a minor phase constituent of the total reaction zone. Further, the microprobe and SEM x-ray energy dispersive analysis of crystals on the hot face of the specimens show the presence of a major crystalline phase containing, in addition to oxygen, large amounts of Zn, Al, and Fe, along with minor amounts of Na and Ni. Therefore these crystals are probably an iron-zinc-aluminum oxide spinel with a lattice spacing near that of hercynite. The lattice spacing of $ZnFe_2O_4$ is 0.844 nm whereas that of $ZnAl_2O_4$ is 0.808 nm. A solid solution between these members to yield a $Zn(Al,Fe)_2O_4$ spinel would possess a lattice spacing of 0.813 to 0.815 nm if the spinel has a composition of approximately $Zn(Fe_{0.45}Al_{1.55})O_4$ to $Zn(Fe_{0.27}Al_{1.73})O_4$ and if the lattice parameter is a linear function of the Fe/Al ratio. This is known to be the case[8] for the analog compound $Ni(Fe,Al)_2O_4$. Another tentative explanation could be that this phase was $(Zn,Fe)Al_2O_4$, although this assumption would not provide the lattice parameter observed of 0.813 to 0.816 nm unless the Zn content was extremely low, and this does not agree with the chemical analysis results. The lattice parameter observed could also possibly be produced by a phase possessing a distribution of Fe^{2+} - Fe^{3+} on both octahedral and tetrahedral sites as $(Zn,Fe)(Al,Fe)_2O_4$. Without further confirmatory data, we will state that the slag layer contains an iron-zinc-aluminum spinel, perhaps $Zn(Fe,Al)_2O_4$ and hercynite ($FeAl_2O_4$).

Other diffraction lines not attributable to any known phase were observed in the x-ray diffraction pattern of the material from the flame-side specimen. Microprobe examination of this region showed existence of an oxide phase containing Al, Si, Ca, Fe, Zn, and Ti in close proximity to the hercynite crystals. This material typically had a glassy appearance.

Scanning electron microscopy (SEM) in combination with energy-dispersive x-ray analysis (EDX) of pre- and posttest specimens provided additional detail of the microstructures. A fracture surface through a pretest sample containing HAB brick and the PBM mortar was examined. Two major crystalline features were found in the brick, and these (mullite and alumina) are depicted in Fig. 13. Basically the microstructure of the HAB brick consists of very fine-grained mullite-bonded sintered Al_2O_3 aggregate. This refractory was similarly fractured perpendicular to the slag plane and examined after completion of the test. Fig. 14(a) illustrates the surface of the slag near the fracture. It consists of a dense underlayer above which is located a blocky surface. At higher magnification [Fig. 14(b)] one of these blocky features is seen to be capped by a mound of material, which is shown in side view in Fig. 14(c). EDX analysis of the mound yields the elements, in addition to oxygen, Al, Si, Ca, Fe, and Zn in major amounts with Mn, Ti, Ni, and Pb also present. The shape of these mounds indicates that this material was a liquid at the test temperature. The material below the mound appears to be a highly developed (111) plane, probably of a cubic oxide spinel, containing major amounts of Fe, Al, and Zn and minor Na and Ni. These two features, the mounds and underlying crystals, are common to both faces of all the posttest specimens investigated.

Figure 15 shows an area on the fracture surface encompassing the slag-to-brick region. Fig. 15(a) at low magnification illustrates the location relative to the sample surface which faced the burner. EDX measurements at selected locations on this area, Figs. 15(b),(c), show that the material contains several phases. Residual alumina grains are predominant near EDX locations 2 and 4 along with some Fe and Zn. Spinel crystals are predominant in the area near EDX point 1, while a

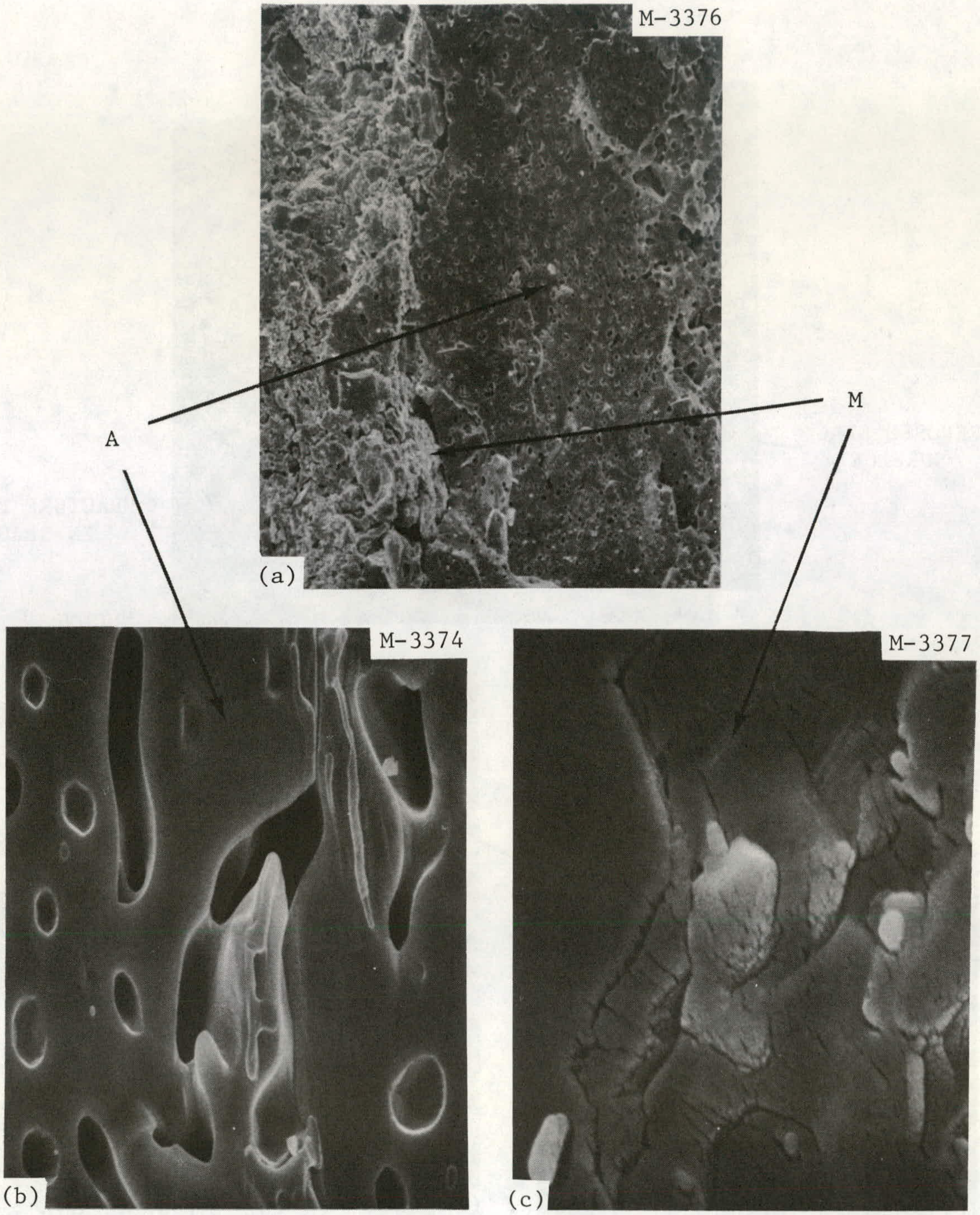

Fig. 13. Scanning Electron Micrograph of Pretest HAB Specimen. A: Al_2O_3 grains. M: mullite matrix. (a) Area containing alumina grains and mullite matrix. 100×. EDX shows only Al and Si. (b) Alumina grain. 1000×. EDX shows only Al. (c) Matrix area. 10,000×. Area scan EDX shows Al and Si.

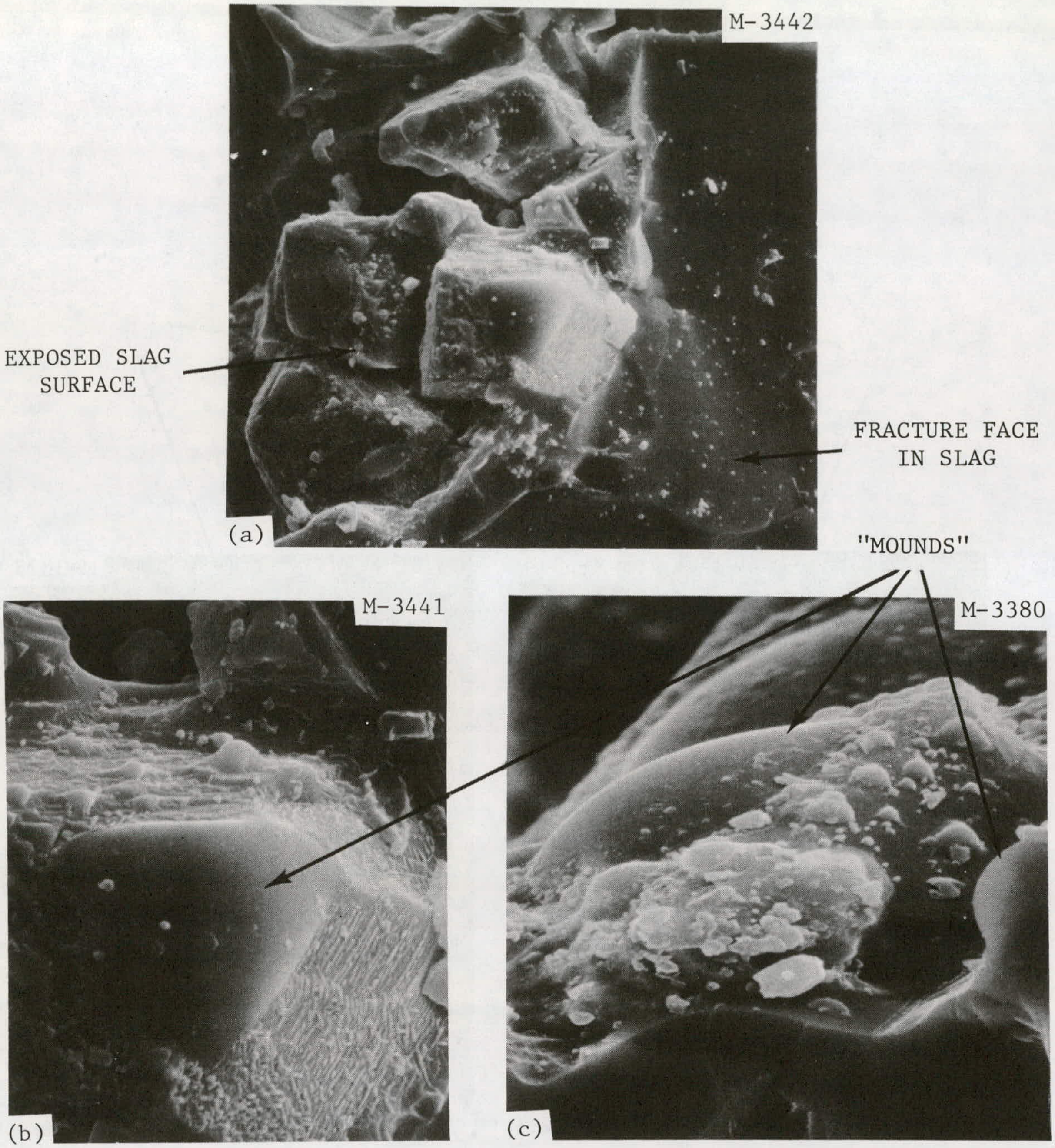

Fig. 14. Scanning Electron Micrographs of Slag Surface on HAB Specimens. (a) Slag surface near fracture area. 1000×. (b) Same area as (a), 3000×. Note "mound" of material underlain by blocky structure. (c) Side view of "mound" showing smoothly curved surface. 3000×.

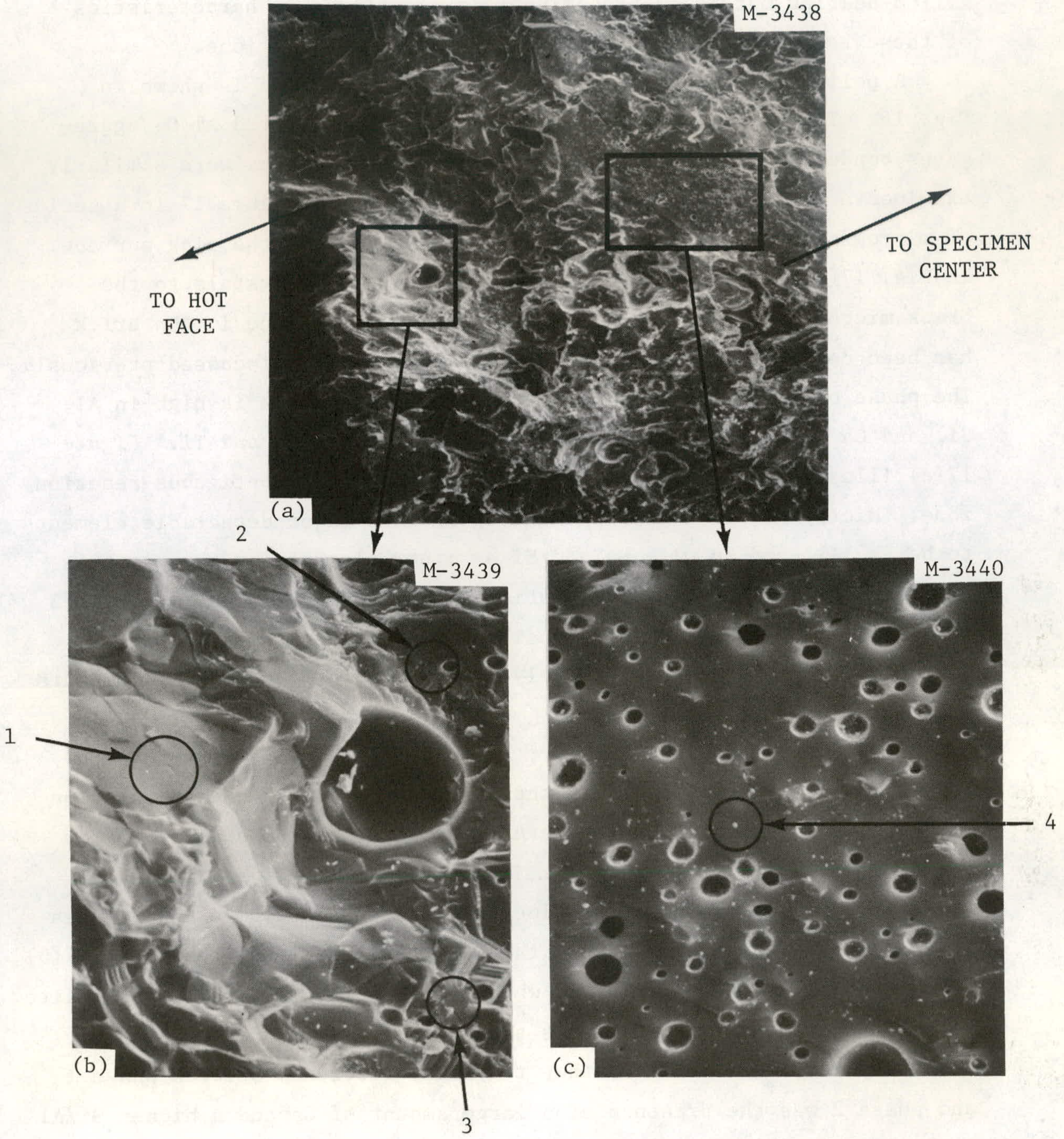

Fig. 15. Scanning Electron Micrograph of HAB Specimen Showing Cross Section of Slag Zone. (a) Fracture area near specimen front face. 1000×. (b) Selected area at 3000×. EDX at location 1: Al, Fe, Zn major; Na, Ni minor. EDX at location 2: Al major; Fe, Zn minor. EDX at location 3: Al, Fe, Zn major; Na, Si, Ca, Mn, Ni minor. (c) Selected area from different direction at 3000×. EDX at location 4: Al major, Fe, Zn minor.

silica-bearing matrix is predominant in location 3. Characteristics of these regions are also illustrated in polished sections.

A polished section of an as-received HAB specimen is shown in Fig. 16. The microstructure consists of large, sintered Al_2O_3 aggregates bonded together with mullite. Posttest specimens were similarly examined after sectioning normal to the hot face. Figure 17 is a series of micrographs illustrating an HAB brick specimen at the slag surface. In Fig. 17(a) the relationship of the spinel-phase crystals to the brick microstructure is shown clearly. A distinct zone in the brick has been converted to the iron-zinc-aluminum spinel discussed previously. The phase of darker color mixed in with these crystals is high in Al, Si, and Ca with additional smaller amounts of Fe, Zn, and Ti. Figure 17(c) illustrates a grain of Al_2O_3 which contains a contiguous reaction zone. Microprobe results for this region show major detectable elements to be Fe, Al, and Zn with Na and Ni as minor elements in the crystals at location 1. The mound at location 2 and the material at location 3 in the spinel are calcium aluminosilicate glass. Within the porous aggregate, crystals consist largely of detectable Al with minor amounts of Fe and Zn at location 4.

Behind the actual slag layer, Fig. 17(b), crystals of hercynite are observed at location 5. In the matrix surrounding these (location 6), Al, Si, Ca, Fe, Ti, and Zn were detected in ratios similar to the matrix at location 3, Fig. 17(c).

A crystalline matrix phase located between the alumina aggregates is not observed near the slag surface where it is glassy [see Fig. 17(b)] but only deeper within the brick where it is no longer primarily mullite. This matrix contains three phases as shown in Fig. 17(d). Microprobe evaluation of these revealed that the main difference between phase 1 and phase 2 was the presence of a large amount of Ca and a higher Si/Al ratio in phase 1. Both of these contained measurable concentrations of iron impurity. Phase identification of the small bright spots (phase 3) could not be accomplished unambiguously and their identity is presently unknown.

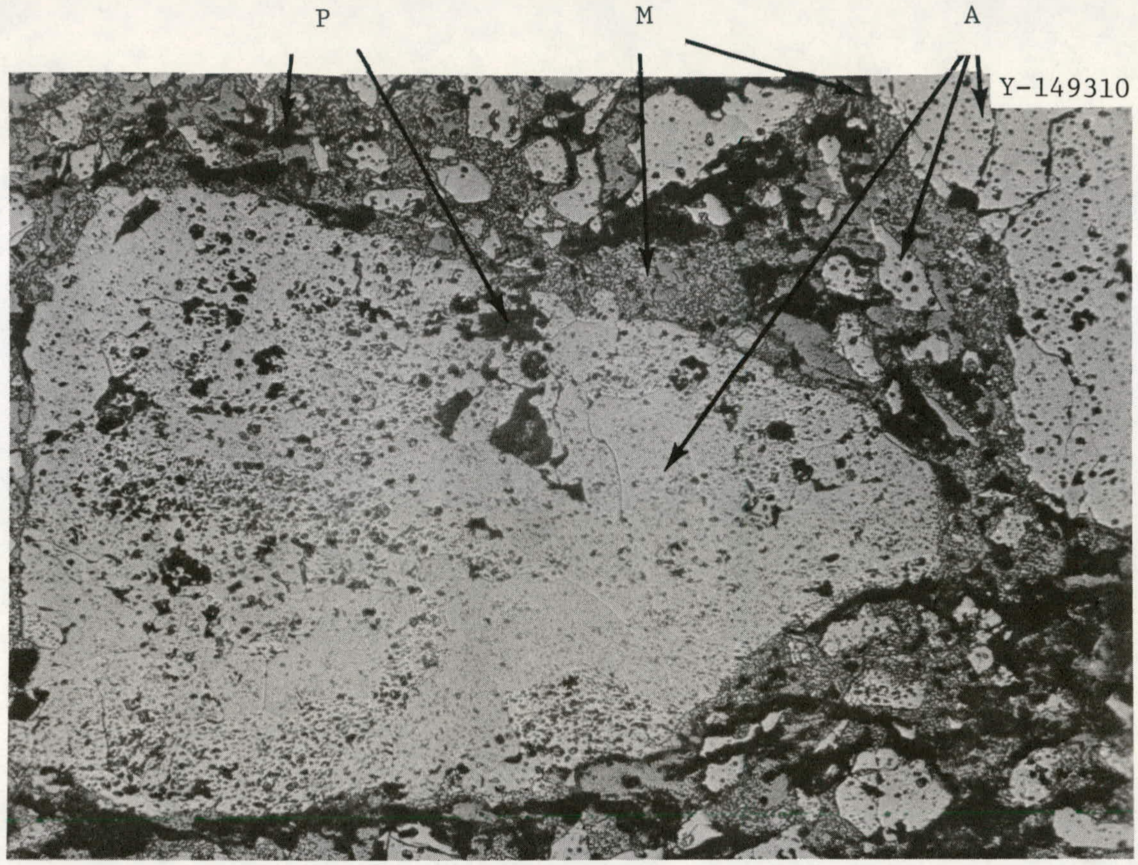

Fig. 16. Polished Section of HAB Specimen. As received, 100×. Large central agglomerate is alumina, darker matrix is mullite. Black areas are porosity. A: alumina; M: mullite; P: porosity.

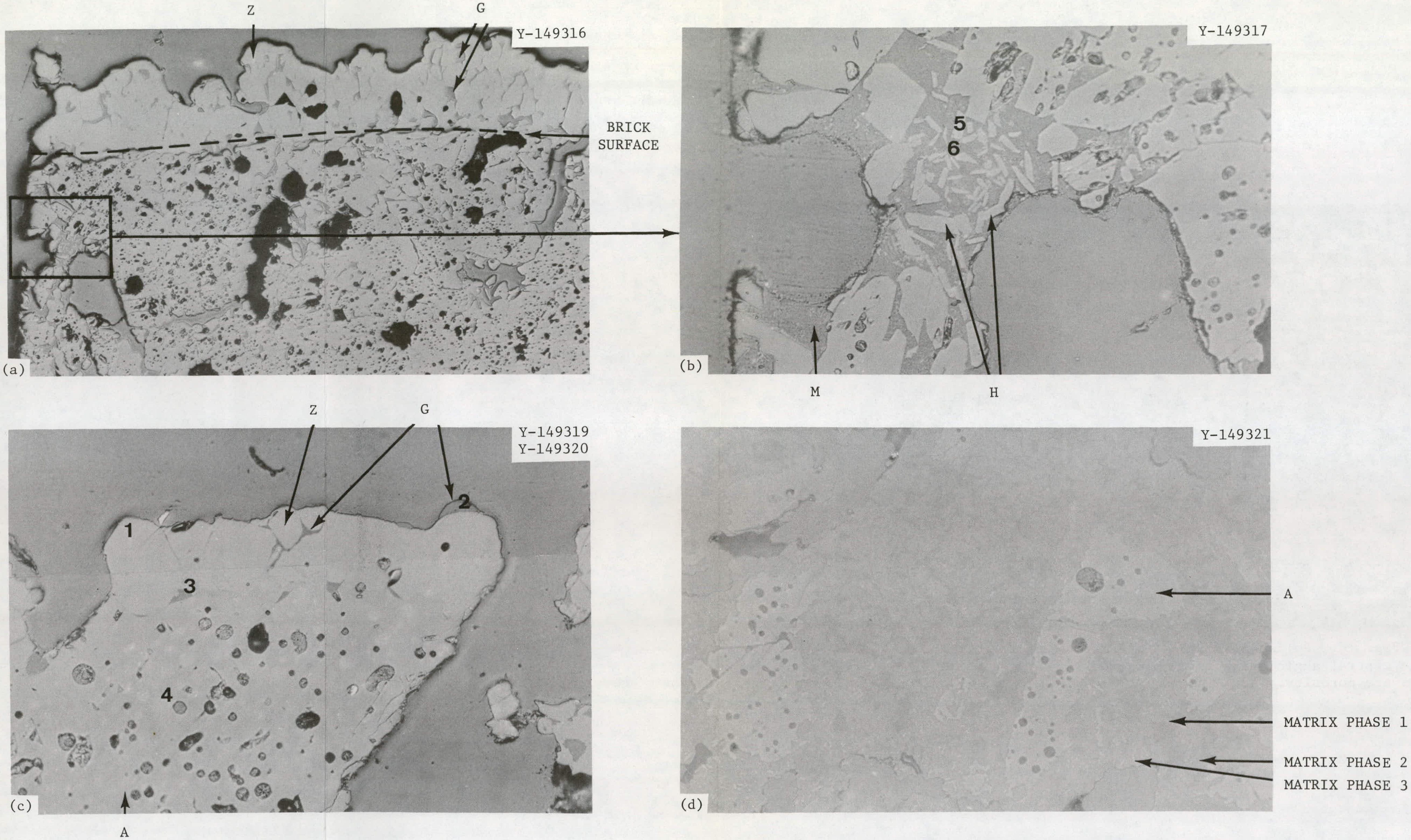

Fig. 17. Polished Sections of HAB Specimens After Exposure in RTF Test I. Z: Zn–Fe–Al spinel; G: glass; H: hercynite; A: Al_2O_3; M: matrix silicate. (a) Hot face of flame-side specimen. Note distinct layer of Zn–Fe–Al spinel crystals on surface. 100×. (b) Selected area from (a), 500×, showing hercynite crystals in fine-grained matrix. (c) Partially converted Al_2O_3 grain showing Zn–Fe–Al spinel phase at slag surface. 500×. (d) Matrix area of brick about 6 mm (1/4 in.) from hot face. Matrix consists of at least three phases. 500×.

Phosphate-Bonded Mortar (PBM)

The characteristics of pre- and posttest mortar samples were similar to those of the brick. Chemical analysis results are presented in Table 5. These were obtained using an emission spectrograph technique, which can have some inaccuracy at high concentrations such as for the case of Al and Si in these samples. Changes observed after Test 1 include significant loss of phosphorus from the original mortar composition as well as increases in the content of Fe, Ca, Zn, and Ni, for example. Since phosphorus is a major element in the bonding phase in this material, this loss of phosphorus should have a pronounced effect on the mortar's strength.

Data presented in Table 6 show the effect of the loss of P, as the $AlPO_4$ bonding phase decreases in concentration. The only detectable new phases related to fuel oil impurities are the spinel(s) described previously in the discussion of the HAB specimens.

SEM results showed the very porous nature of the pretest fired mortar specimens [Fig. 18(c)]. An area scan EDX analysis of the entire field of Fig. 18(a) indicated large Al, medium Si, and low Fe and Ti contents. Phosphorus could not be separately analyzed as its x-ray peak was masked by that from the gold film previously evaporated onto the specimen surface.

Fractured posttest specimens were also examined, and Figs. 19(a)-(c) illustrate the nature of the reaction zone. Several features are similar to those described for the HAB specimens, that is, a dense layer of oxide crystals containing major amounts of Fe, Zn, and Al and minor amounts of Na and Ni. These crystals directly underlie mounds containing the above elements plus large amounts of Ca and Si and a smaller amount of Ti. Deeper in the mortar the phase assemblage is quite different, as shown in Figs. 19(d)-(f). At about 4 mm (0.15 in.) depth from the hot face, the mortar aggregates are larger and denser. These consist of grains of Al_2O_3 and what appears to be fine secondary mullite [Fig. 19(f)]. EDX analysis of the crystal in the center of Fig. 19(f) indicated high concentration of Al, Si, and Ti with smaller

Table 5. Chemical Analysis Results from PBM Specimens

Element (as oxide equiv.)	Content (wt %)		
	Pretest[a]	Back-Side	Front-Side
Al_2O_3	Major	Major	Major
Fe_2O_3	0.50	0.50	1.0
SiO_2	10.0	10.0	10.0
CaO	0.10	0.25	1.0
TiO_2	2.0	1.5	1.5
P_2O_5	5.0	0.15	0.15
Na_2O	0.10	[c]	[c]
MgO	0.10	0.30	1.0
MnO	0.03	0.05	0.10
ZnO	0.001[b]	0.10	1.0
NiO	0.01	0.05	0.10
Cr_2O_3	0.10	0.15	0.15
CuO	0.01	0.01	0.01
PbO	0.002	0.05	0.05
V_2O_5	0.01	0.001	0.002
B_2O_3	0.003	0.10	0.30
BaO	0.001[b]	0.001[b]	0.001[b]
Ag_2O	0.002	0.005	0.003
K_2O	0.10	0.10	0.30
SnO_2	0.001[b]	0.001[b]	0.001[b]
CoO	0.001	0.01	0.03
SrO	0.003	0.005	0.005

[a] Mixed with H_2O, dried, fired 20 hr in air at 1375°C (2500°F).

[b] Not detected. Number is minimum limit of detection.

[c] Masked by Zn interference.

Table 6. Results of X-Ray Diffraction Analysis of PBM Specimens

Specimen Type	Phases Present and Amount	
	Major	Minor
Heated 115 hr in air at 1375°C (2500°F)	$AlPO_4$, α-Al_2O_3, mullite	
Back-Side, Posttest	α-Al_2O_3, mullite	Spinel
Front-Side, Posttest	α-Al_2O_3, mullite	Spinel

amounts of Fe and Zn. Analysis of a mortar specimen originally located ∿6 mm (1/4 in.) from the hot face indicated a significant concentration of Fe from the fuel oil.

Posttest ceramographic and microprobe examination showed phase contents similar to those determined for the HAB samples. Figure 20(a) illustrates the highly porous nature of the mortar and a distinct surface layer. The crystal phase at the surface is the Fe-Zn-Al spinel discussed previously, surrounded by a darker matrix containing high concentrations of Al and Si, medium concentrations of Ca, Fe, and Zn, and small levels of Ti and S. Just behind this layer [Fig. 20(b)] there was an area containing blocky hercynite crystals in a matrix similar in composition to the matrix surrounding the Fe-Zn-Al spinel. The bright areas in Fig. 20(b) are possibly an $Al_2O_3 \cdot TiO_2 - Fe_2O_3 \cdot TiO_2$ (ATFT) phase similar to that observed in an 85% Al_2O_3 brick by Crouch.[9] The crystals were not present in pretest samples. Crystalline siliceous phases are only observed in areas deeper in the mortar and adjacent to the brick.

Mullite-Based Brick (MBB)

The test specimens of MBB are pictured in Fig. 21. During Test 1, the color changed from its original cream to dark blue-black on the front surface and brown on the back surface. The vertical cracks generated during the test ran completely through these brick and were

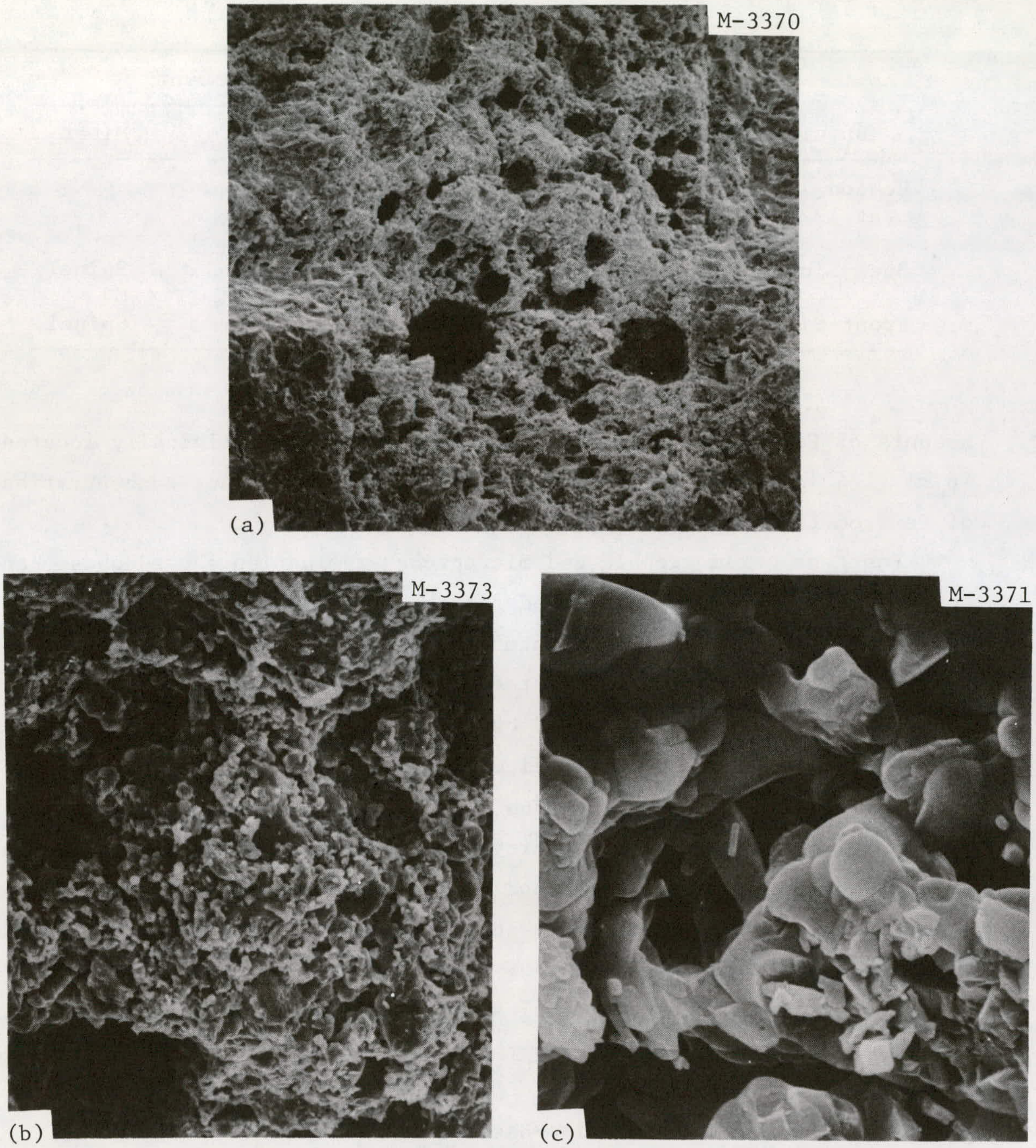

Fig. 18. Pretest Scanning Electron Micrographs of PBM Mortar-Brick Joint. (a) High porosity shown at 55×. (b) and (c) Same area at 300 and 3000× show heterogeneous crystalline nature of mortar.

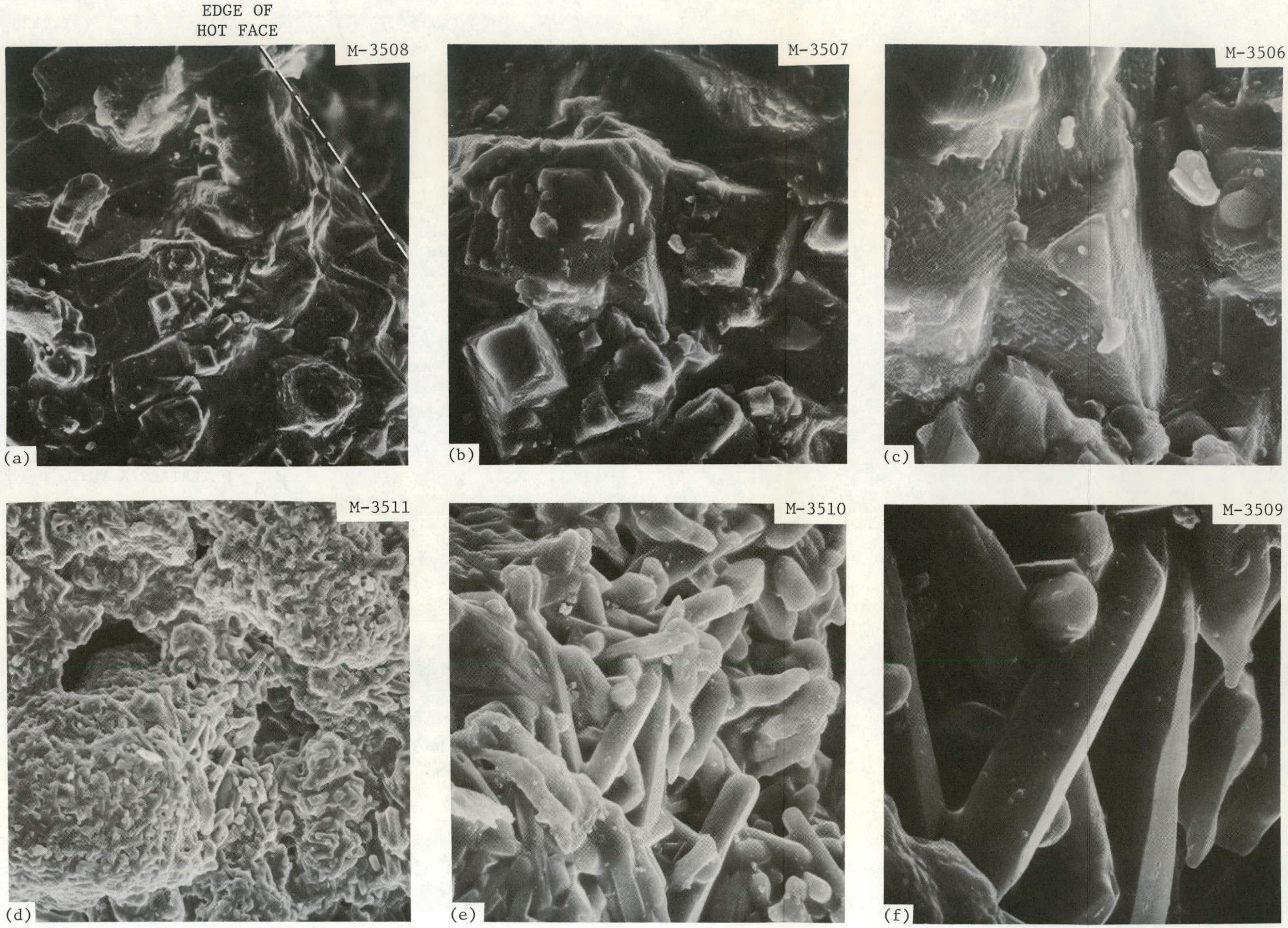

Fig. 19. Scanning Electron Micrographs of PBM Specimens After Test. (a) Dense area near mortar surface. 300×. (b) Crystalline blocks capped by glassy mounds. 1000×. (c) Crystalline blocks capped by glassy mounds. 3000×. (d) Inner region at 300×, showing dense aggregates, large pores. (e) Same area at 1000×, showing mullite (?) crystals. (f) Same area, 3000×.

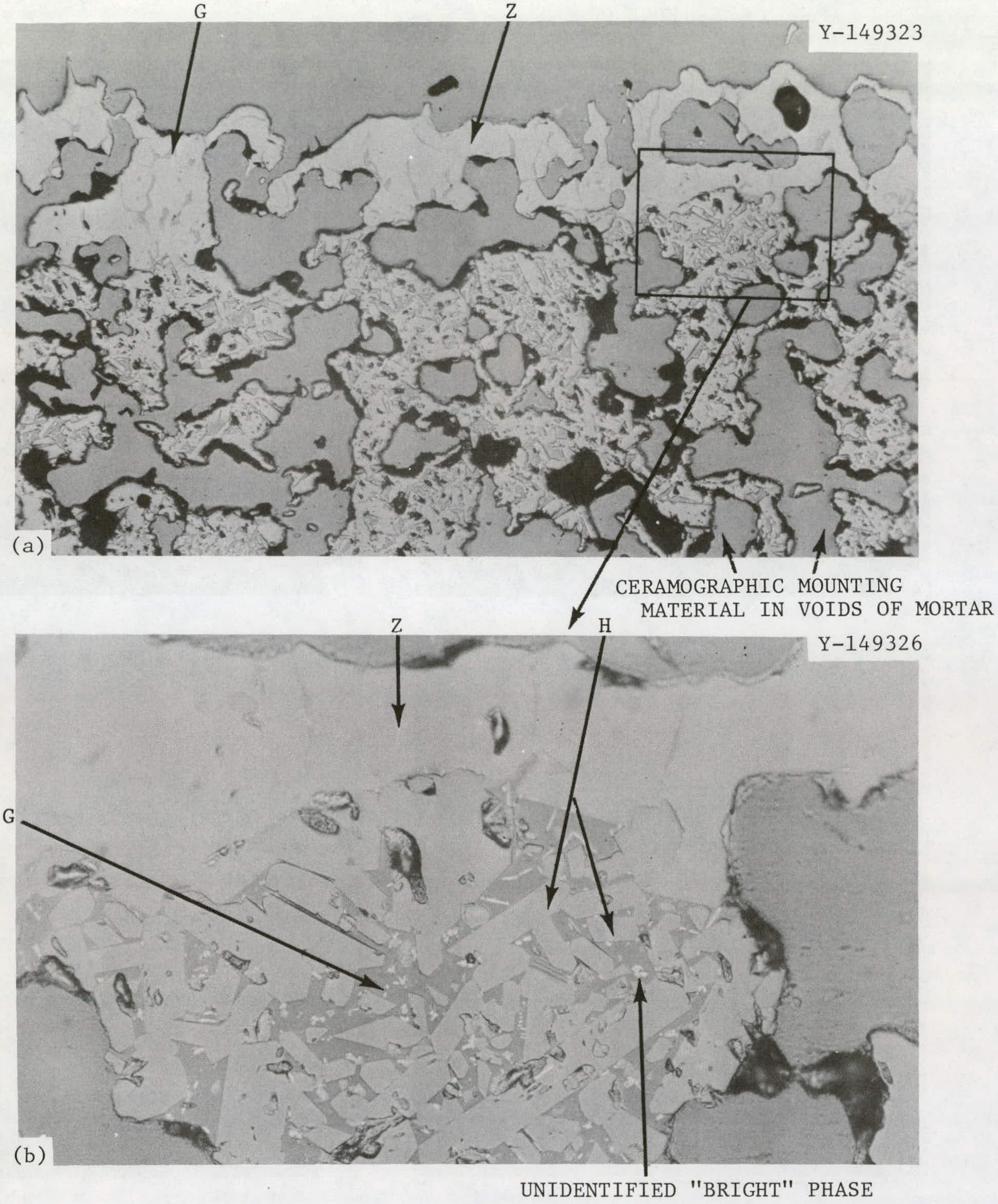

Fig. 20. Polished Sections of PBM Mortar Post-Test. Z: Zn-Fe-Al spinel; G: glass; H: hercynite. (a) Hot surface of flame-side specimen at 100× shows Zn-Fe-Al spinel and glassy matrix at surface. (b) Area behind surface layer at 500× shows hercynite and ATFT crystals in glassy matrix.

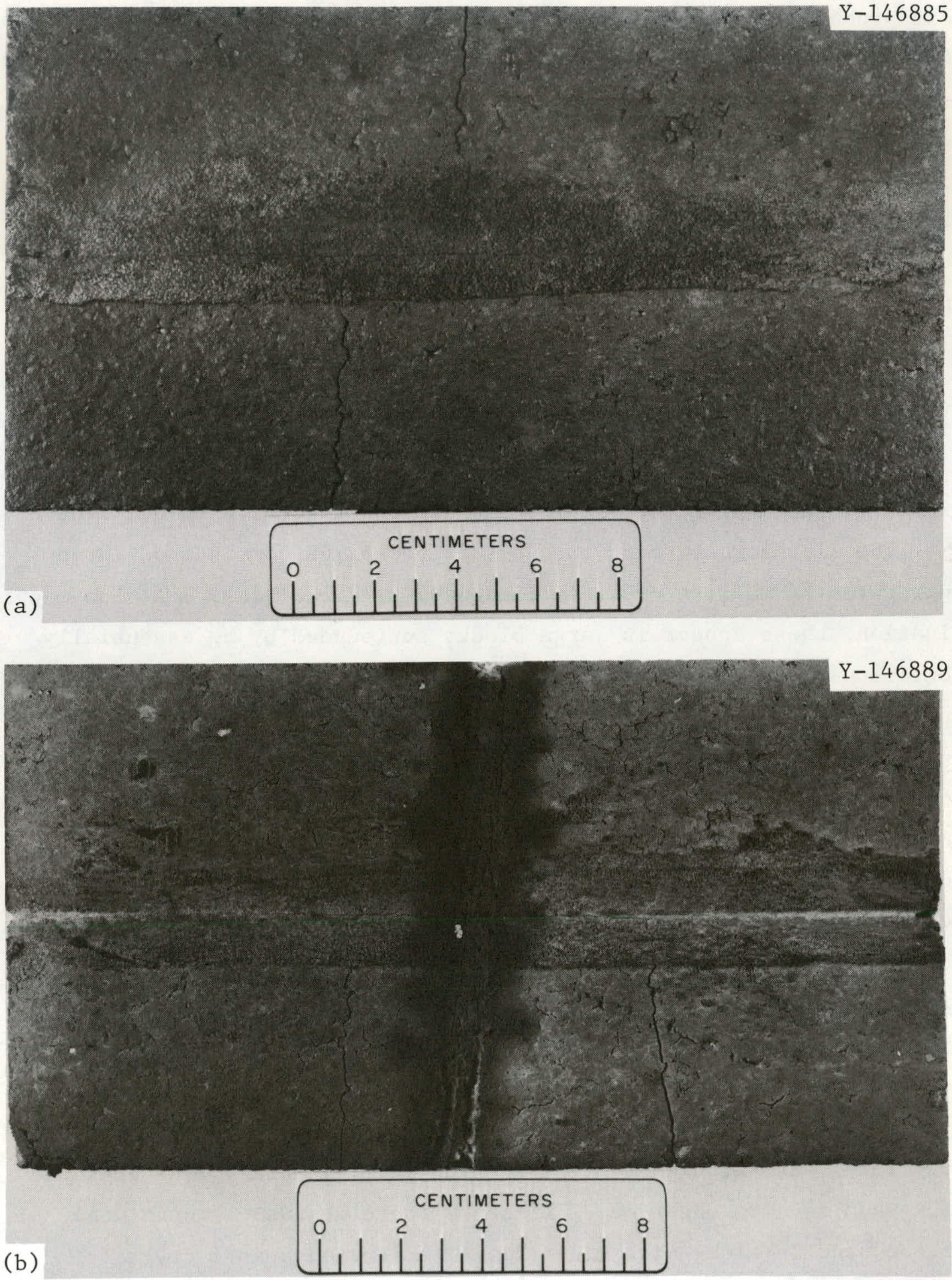

Fig. 21. Visual Appearance of MBB Brick and MBM Mortar Specimens After Test. (a) Flame-side (front) surface. (b) Back side surface.

most probably produced by thermal stresses. A horizontal crack between the mortar and top brick similarly extended completely through the section. The brick was sectioned similarly to the HAB sample, and the specimens were analyzed by procedures described previously.

Results of chemical analyses are presented in Table 7. The Fe_2O_3, TiO_2, and Na_2O equivalent levels are higher in this refractory than in the HAB specimens. After completion of the test, the Fe, Ca, Na, Mg, Zn, Ni, and Pb contents have increased significantly. All of these elements were present in the fuel oil (Table 2).

X-ray diffraction results are presented in Table 8. The as-received brick is largely mullite with a small amount of residual cristobalite plus a glass phase not detectable by x-ray diffraction. After the test exposure, the only new crystalline phase observed is a spinel type.

The microstructure of the as-received brick consists of large aggregates of mullite crystals bonded by silicate glass. At low magnification, these appear in large blocks surrounded by an essentially continuous void [Fig. 22(a)]. At higher magnification needles of mullite are observed [Figs. 22(b),(c)] as expected. Also visible are conchoidal fractures in the cristobalite [Fig. 22(d)]. EDX analysis of the smooth region in the field of Fig. 22(d) indicated only Si as expected for the case of the cristobalite polymorph of SiO_2. The needle-shaped crystals such as those shown in Fig. 22(b) contain detectable Al and Si with minor Ti and Fe. Adjacent to these crystals, the glassy or amorphous area between these crystals contained Al and Si as major detectable elements plus K, Ti, and Fe.

SEM derived pictures of the hot face surface of a posttest specimen are shown in Fig. 23. Like the HAB specimen, the actual surface consists of a dense layer. The fracture area and surface are shown in Fig. 23(a), and at higher magnification in Fig. 23(b). The presence of mounds is also observed. EDX shows these mounds to contain Al, Si, Ca, Fe, and Zn along with minor Ti. The faceted spinel crystals previously observed in HAB specimens are not present in this refractory. Figure 24(a) illustrates the thickness of a slag layer on the MBB specimens after the test. In Fig. 24(b) located just below the slag layer

Table 7. Chemical Analysis Results from MBB Specimens

Element (as oxide equiv.)	Content (wt %) As-Received	Back-Side	Front-Side
L.O.I.	0.30	0.30	0.31
Al_2O_3	46.11	44.95	44.01
Fe_2O_3	1.04	1.07	2.60
SiO_2	50.35	50.51	48.04
CaO	0.015	0.11	1.28
TiO_2	1.78	1.78	1.67
P_2O_5	0.10[a]	0.10[a]	0.10[a]
Na_2O	0.33	1.01	1.21
MgO	0.001	0.001	0.29
MnO	0.005	0.02	0.05
ZnO	0.002	0.05	0.10
NiO	0.01	0.05	0.30
Cr_2O_3	0.05	0.05	0.05
CuO	0.003	0.05	0.10
PbO	0.003	0.05	0.10
MoO_3	0.001[a]	0.001[a]	0.001[a]
V_2O_5	0.03	0.03	0.03
B_2O_3	0.003	0.003	0.003
BaO	0.002	0.002	0.02
Ag_2O	0.003	0.002	0.0005
K_2O	0.20	0.25	0.21
SnO_2	0.001	0.001[a]	0.001
CoO	0.002	0.002	0.005
Total	100.24	100.25	100.29

[a] Not detected. Number is minimum limit of detection.

Table 8. Results of X-Ray Diffraction Analysis of MBB Specimens

Specimen Type	Phases Present and Amounts Major	 Medium	 Minor
As-Received	Mullite		Cristobalite
Back-Side, Posttest	Mullite		Cristobalite, Spinel
Front-Side, Posttest	Mullite		Cristobalite, Spinel

a void is shown, which was found to be lined with mullite-shaped crystals consisting of Al, Si, Ti, Fe, and Zn.

Ceramographic examination and electron microprobe results supported conclusions derived from the SEM data. Fig. 25(a) is a low magnification photograph of a polished section through the pretest MBB brick and MBM mortar. The large mullite aggregates and surrounding cracks are readily apparent. At higher magnification, in Figs. 25(b) and (c), the nature of the mullite and the cristobalite phase is illustrated. Figure 26 illustrates the microstructure of the MBB specimen which faced the burner and includes the slag surface. The oxide crystals containing high levels of Fe, Zn, and Al observed in other specimens were present. The matrix material contains the same elements as observed for other specimens, notably high Al and Si, medium Ca and Fe, and small Zn and S. The highly reflective needle-shaped crystals apparent in Fig. 26(a) were unique to the MBB specimens. These crystals contain the same elements as the matrix plus a significant amount of Ti. They are present in insufficient quantity to analyze by x-ray diffraction. Fig. 26(b) is of the slag area immediately behind the area shown in Fig. 26(a). It contains a light gray phase containing major Al and Si and is therefore probably mullite. Lower concentrations of Fe, Ti, and Zn were also detected. The matrix material in this sample appears to be a glass and contains major concentrations of Al and Si, plus lesser levels

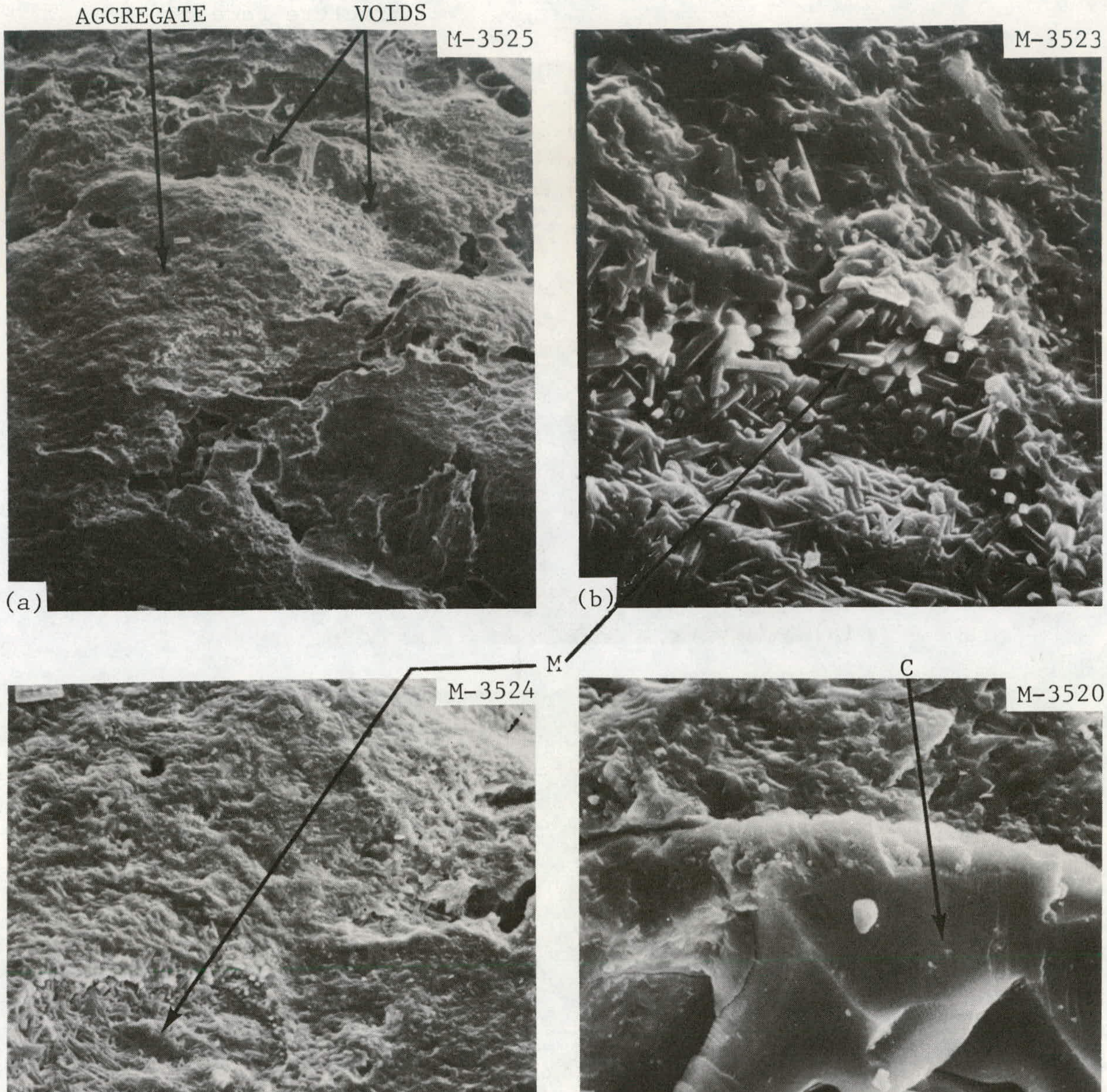

Fig. 22. Scanning Electron Micrographs of PreTest MBB Specimens, M: Mullite; C: Cristobalite. (a) Fracture surface showing mullite aggregates, voids. 300×. (b), (c) Same area at 1000 and 3000× showing mullite needles, glass matrix. (d) Different area of same specimen, showing cristobalite grain. 1000×.

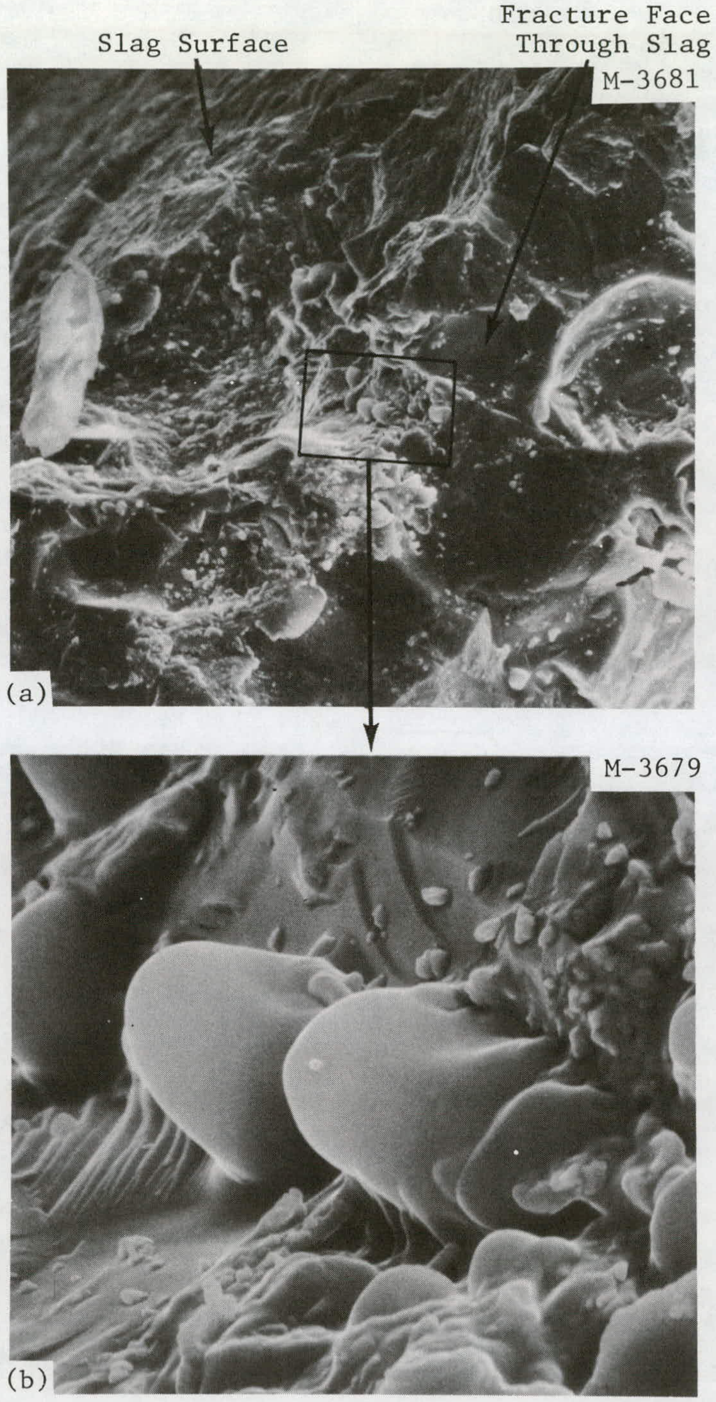

Fig. 23. Fracture Face and Slag Surface on MBB Post-Test. (a) Dense slag region. 300×. (b) Same area at 3000× shows mounds.

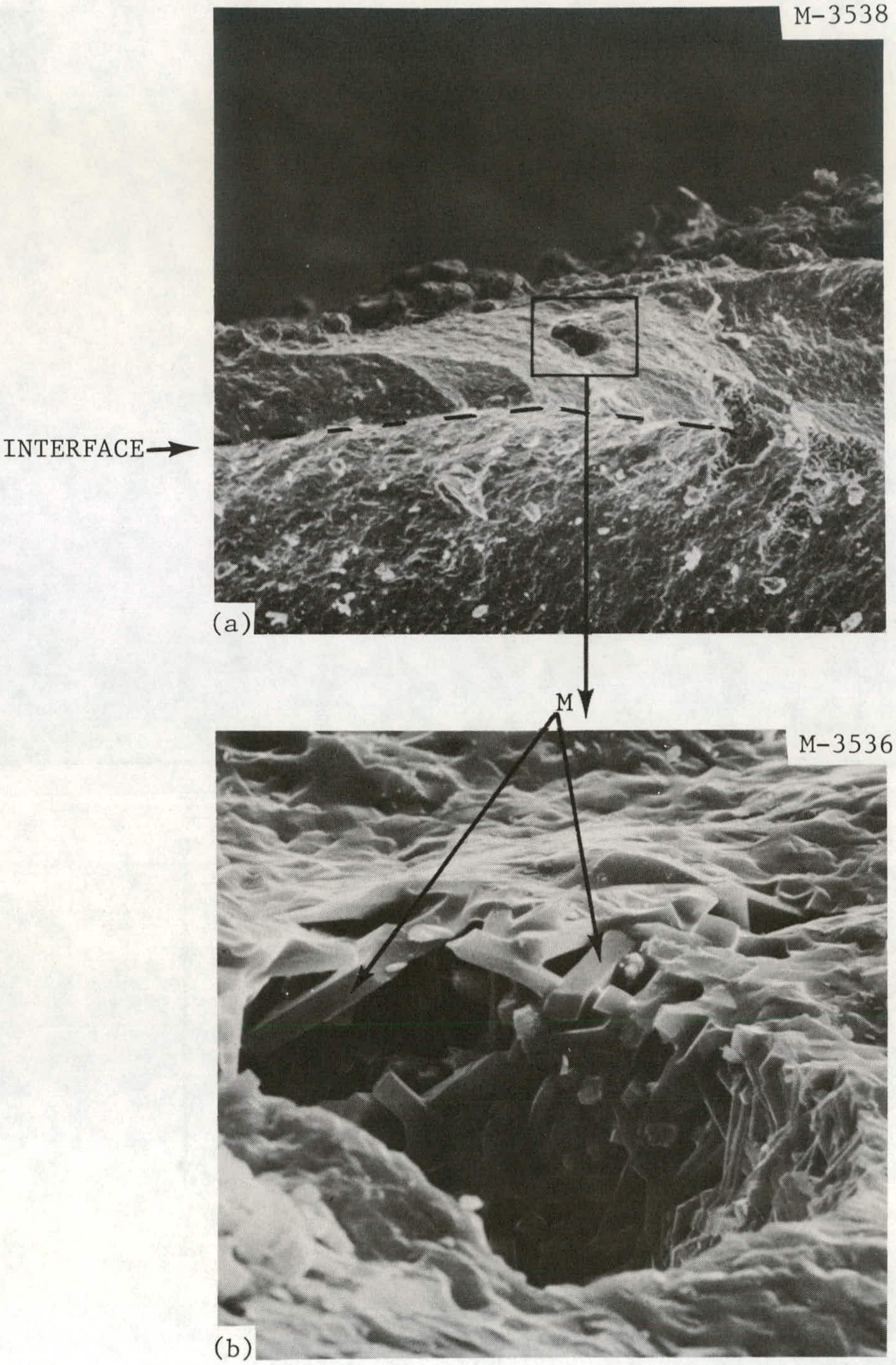

Fig. 24. Fracture Area Through MBB Brick and Slag. M: mullite; B: brick, S: slag layer. (a) Dense slag layer overlays brick surface, contains void. 100×. (b) Void shows mullite needles. 1000×.

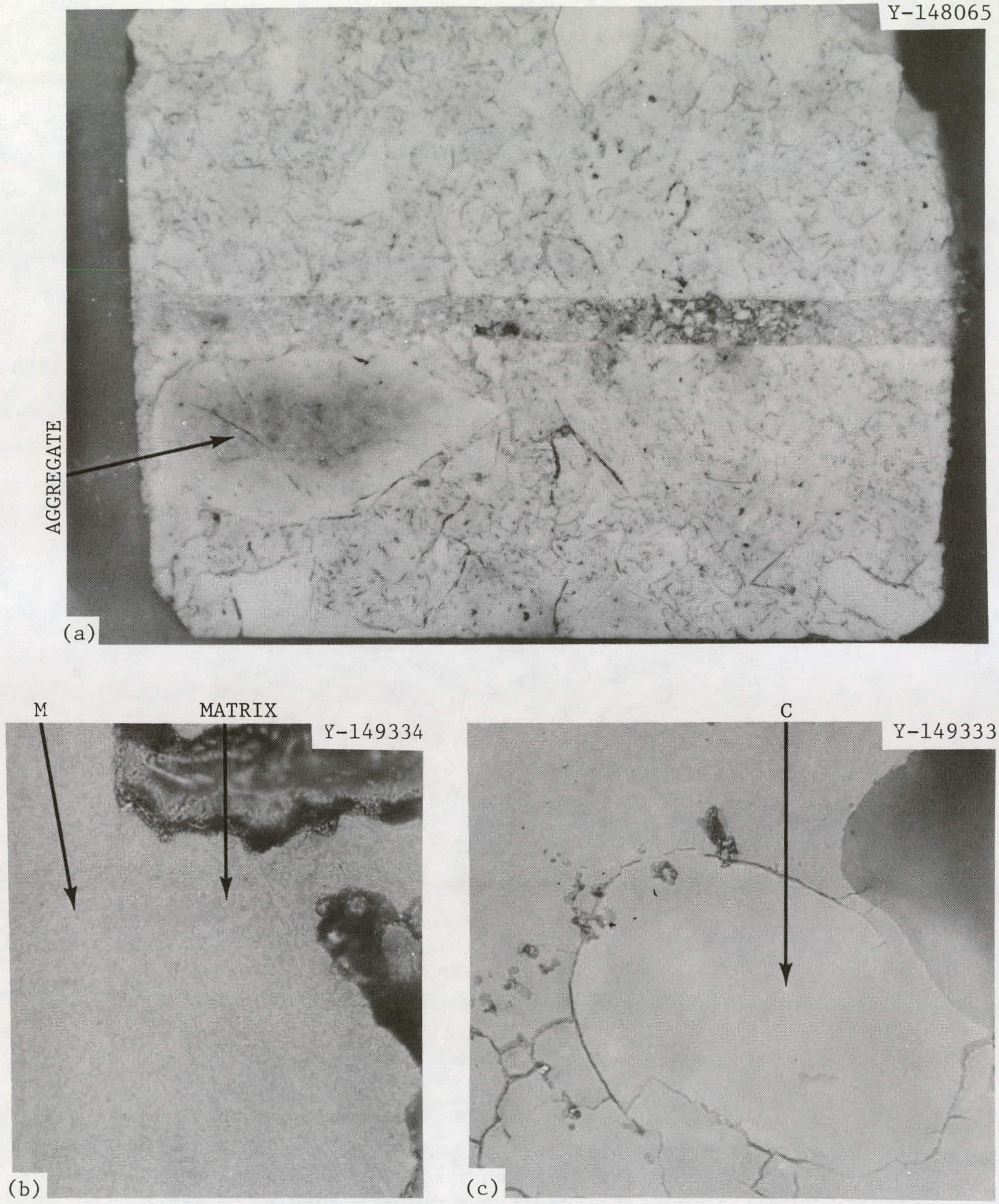

Fig. 25. Pretest MBB Specimens. M: mullite; C: cristobalite. (a) MBM joint between MBB brick specimens. 100×. Mullite aggregates are surrounded by cracks. (b) Polished section of mullite aggregate in MBB specimen shows mullite crystals (light gray) in glassy matrix (darker gray). 500×. Very dark areas are voids and mounting material. (c) Cristobalite remnant in contact with mullite aggregate. 500×.

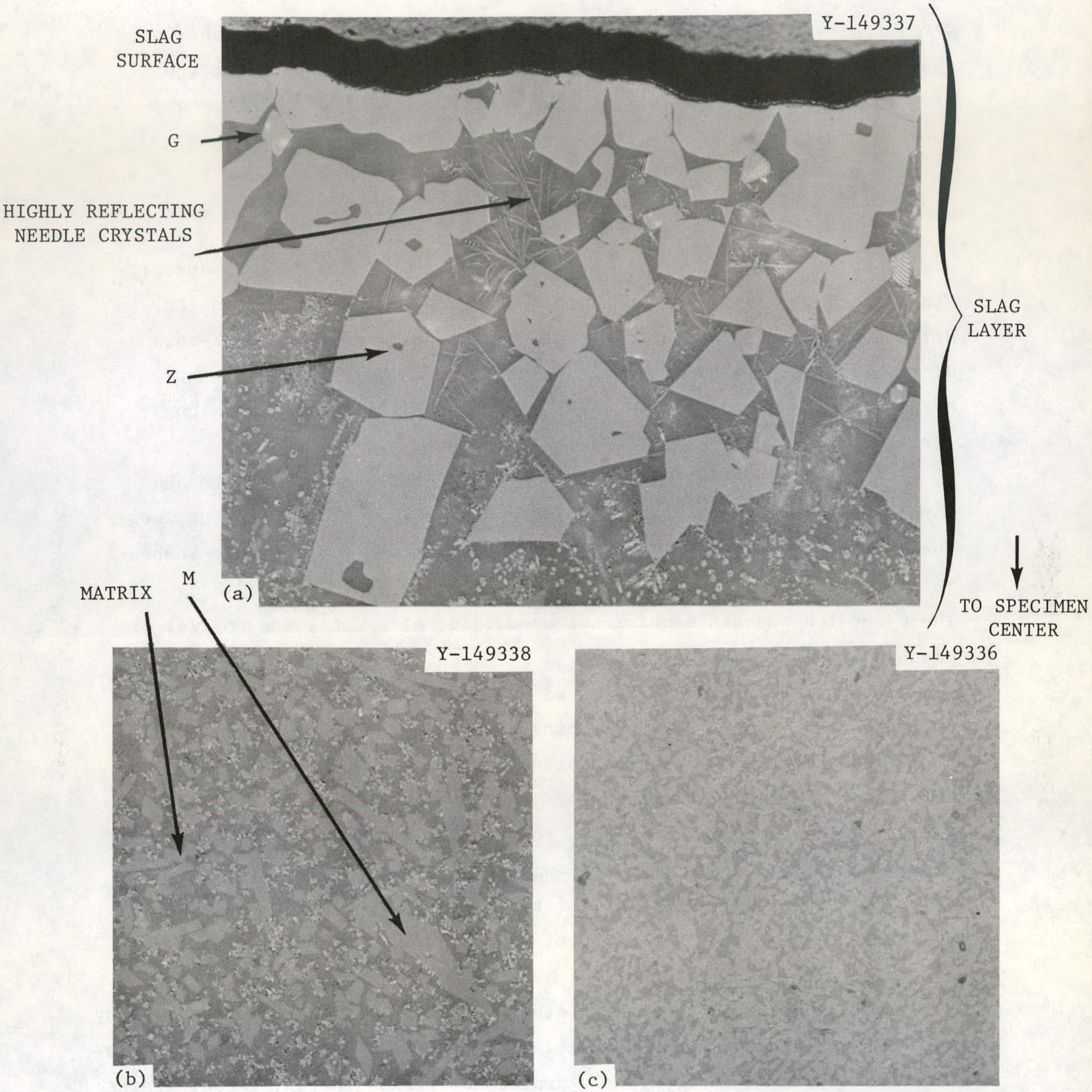

Fig. 26. MBB and Slag Layer Near Hot Face. 500×. Z: Zn-Fe-Al spinel; G: glass; M: mullite. (a) Slag layer containing spinel crystals, silicious matrix, and fibrous inclusions. (b) Slag layer just behind (a), showing contaminated mullite crystals, matrix, and inclusions. (c) Brick just behind (b), showing mullite and matrix. Compare with Fig. 25(b).

of Ca, Fe, Ti, and S. The bright phase contains the same elements as the needle-shaped crystals seen in Fig. 26(a). Going back from the slag into the brick, these disappear [see Fig. 26(c) which shows a location just below the distinct slag layer].

Mullite-Based Mortar (MBM) Specimens

Results of the chemical analyses for the mortar specimens are presented in Table 9. Significant increases in the Ca, Fe, Mg, Mn, Zn, Ni, and Pb contents are attributable to fuel oil impurities. X-ray diffraction results of the reaction zone in Table 10 show that the original α-Al_2O_3 and mullite phases are present after testing along with the new spinel phases described previously.

The mortar microstructure consists of aggregates of mullite and corundum grains. These are visible in Fig. 27(a), along with the large void volume fraction. At very high magnification, small needle-shaped mullite crystals can be seen in the fracture surface [Fig. 27(b)]. These needles contain significant amounts of Al and Si, and smaller amounts of Fe, K, Ca, and Ti.

After exposure to the residual oil combustion, the surface is covered with a dense slag containing blocky Fe-Zn-Al spinel crystals in a glassy matrix as described previously for the other materials. A mass of slag penetrates the mortar joint more deeply than it penetrates the brick, due at least partially to its higher porosity. Within this slag-filled area, voids are lined with well developed mullite crystals (Fig. 28). EDX analysis of one of the crystals in Fig. 28(b) shows the presence of major quantities of Al and Si with minor amounts of Ca, Ti, Fe, and Zn.

The microstructure of the pretest mortar as revealed by ceramography is shown in Fig. 29. This material is multiphase, containing aggregates of fine mullite in a very finely grained or glassy matrix, larger grains of corundum (large light areas in the figure), and porosity (black).

After Test 1, the MBM specimens shown in Fig. 30 possess a highly heterogeneous microstructure. The slag surface contains Zn-Fe-Al spinel

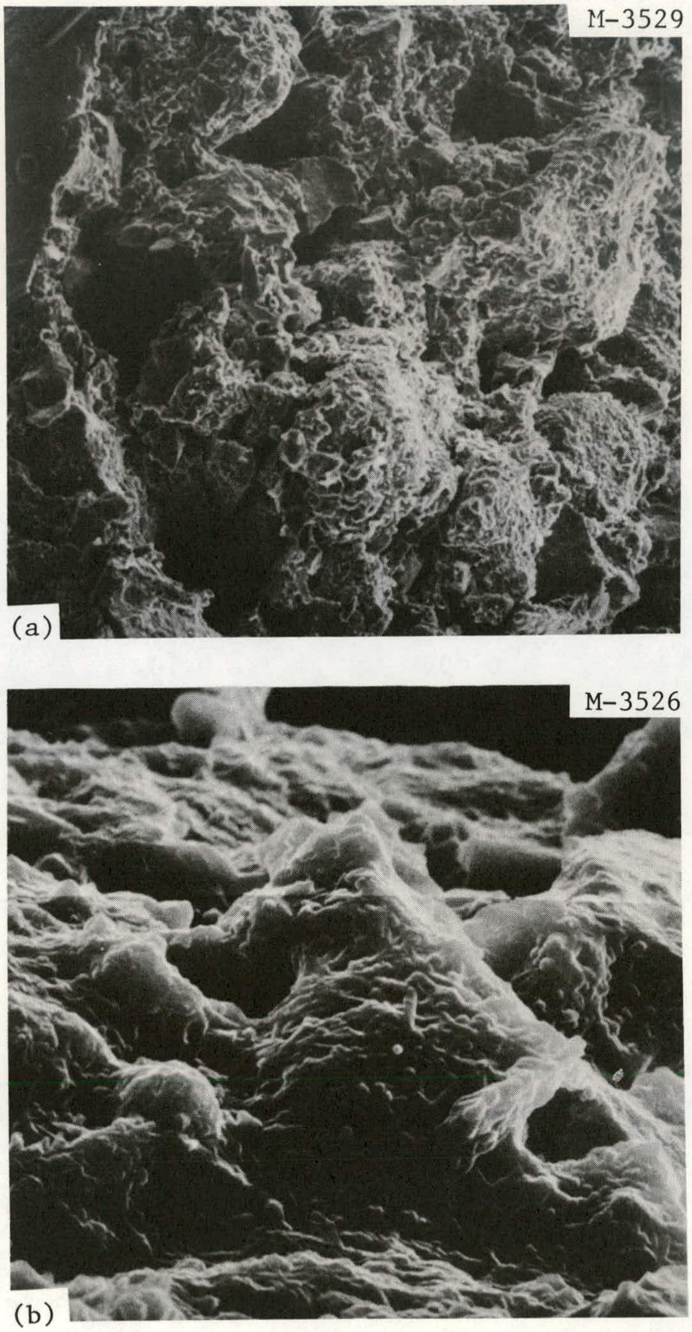

Fig. 27. Scanning Electron Micrographs of Pretest MBM Specimens. (a) Fracture surface through mortar shows aggregates of mullite and α-Al_2O_3 along with voids. 100×. (b) Same area at 3000×, showing very fine mullite crystals.

Table 9. Chemical Analysis Results from MBM Specimens

Element (as oxide equiv.)	Contents (wt %)		
	Pretest[a]	Back-Side	Front-Side
Al_2O_3	Major	Major	Major
Fe_2O_3	0.75	0.75	1.0
SiO_2	Major	Major	Major
CaO	0.50	1.0	3.0
TiO_2	2.0	3.0	3.0
P_2O_5	0.10[b]	0.10[b]	0.10[b]
Na_2O	3.0	2.0	[c]
MgO	0.20	0.50	1.0
MnO	0.01	0.05	0.10
ZnO	0.001	0.10	1.0
NiO	0.03	0.05	0.10
Cr_2O_3	0.15	0.10	0.15
CuO	0.01	0.02	0.03
PbO	0.002	0.10	0.15
V_2O_5	0.05	0.05	0.08
B_2O_3	0.005	0.30	0.50
BaO	0.001[b]	0.002	0.10
Ag_2O	0.003	0.001	0.002
K_2O	0.20	0.50	0.50
SnO_2	0.001	0.001	0.001
CoO	0.002	0.01	0.03
SrO	0.002	0.005	0.005

[a] Mixed with H_2O, dried, fired 115 hr in air at 1375°C (2500°F).

[b] Not detected. Number is minimum limit of detection.

[c] Masked by Zn interference.

Table 10. Results of X-Ray Diffraction Analysis of MBM Specimens

	Phases Present and Amounts		
Specimen Type	Major	Medium	Minor
Heated In Air 115 hr at 1375°C (2500°F)	Mullite	α-Al_2O_3	
Back-Side, Posttest	Mullite		α-Al_2O_3, spinel
Front-Side, Posttest	Mullite		α-Al_2O_3, spinel

crystals (location 1) within a glassy matrix (location 2). The crystal at location 3 is hercynite and is adjacent to needle-shaped crystals. Qualitatively, these latter crystals contain relatively high concentrations of Al and Si, with lesser amounts of Ca, Zn, Ti, and S. The bright phase at location 4 contained largely Al and Si, with lesser amounts of Ca, Fe, Zn, S, K, and Ti. An aggregate of alumina crystals is also visible in Fig. 30(c). The light gray crystals within this aggregate contain Al and less Fe, probably in a solid solution but possible as hercynite. The darker matrix adjacent to the crystals contains Al and Si as the major detectable elements with lesser quantities of Fe and Ti.

High-Alumina Fiber Insulation (HAF)

The nominally 95% Al_2O_3 — 5% SiO_2 fiber insulation specimens are shown in Fig. 31 in the posttest condition and still mounted to the supporting brick. The color of the insulation ranged from dark bluish-black on the surface oriented toward the burner, to dark brown on the surface facing away from the burner. A significant amount of shrinkage has obviously occurred on both sides (compare with Fig. 5) as a result of the combustion product and heat exposure. The front surface has lost a large portion of material, probably due at least in part to poor bonding of the fibers to the supporting refractory brick. The gross

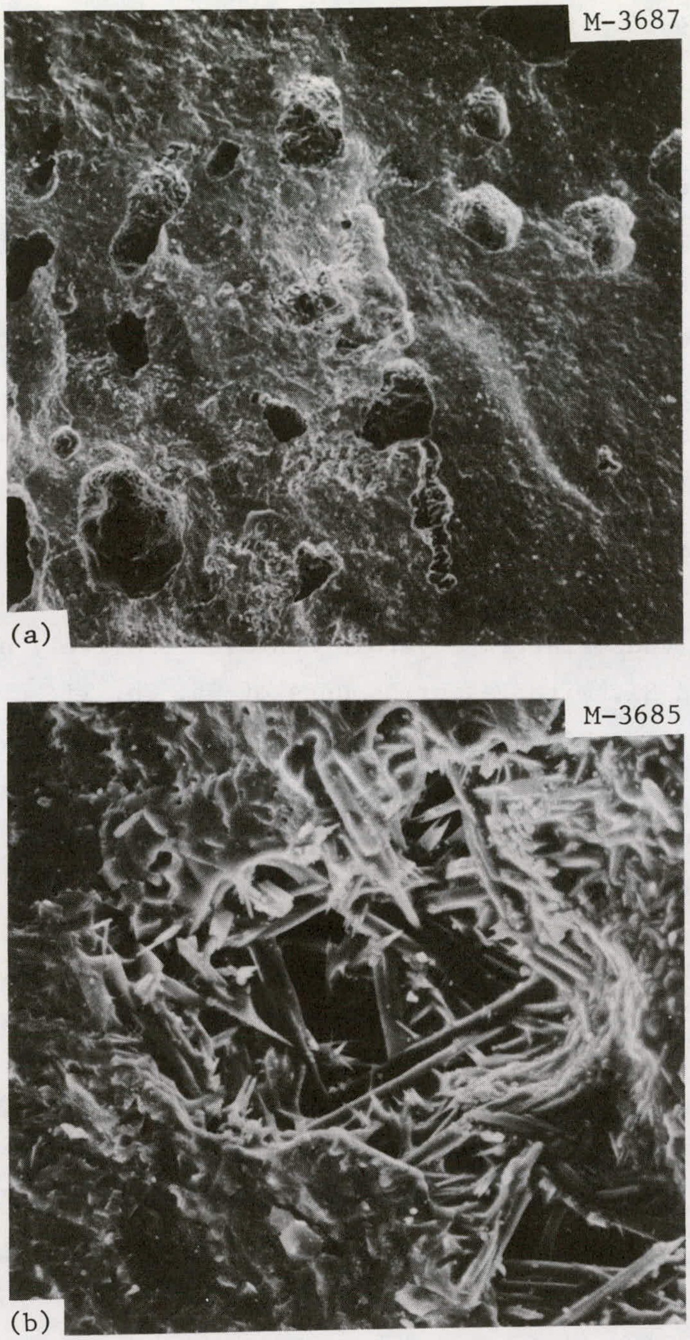

Fig. 28. SEM Micrographs of MBM Specimen, Post Test. (a) Low magnification photograph of fracture surface through MBB brick and MBM mortar shows dense matrix, voids containing needle crystals (mullite?). (b) Same area at higher magnification shows needle shaped crystals.

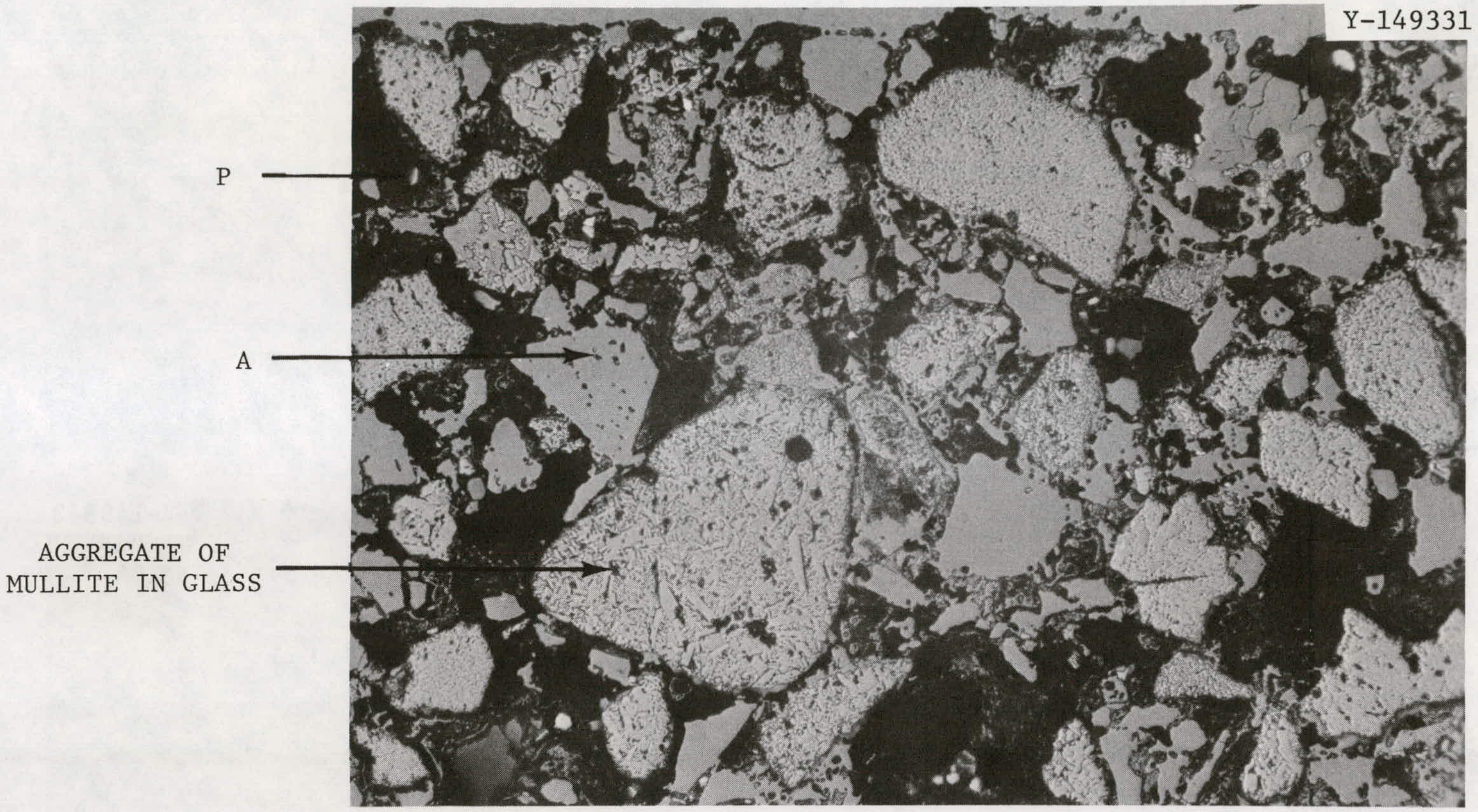

Fig. 29. Pretest Polished Section of Mullite-Based Mortar (MBM) Specimen. 100×. A: Al_2O_3; P: porosity.

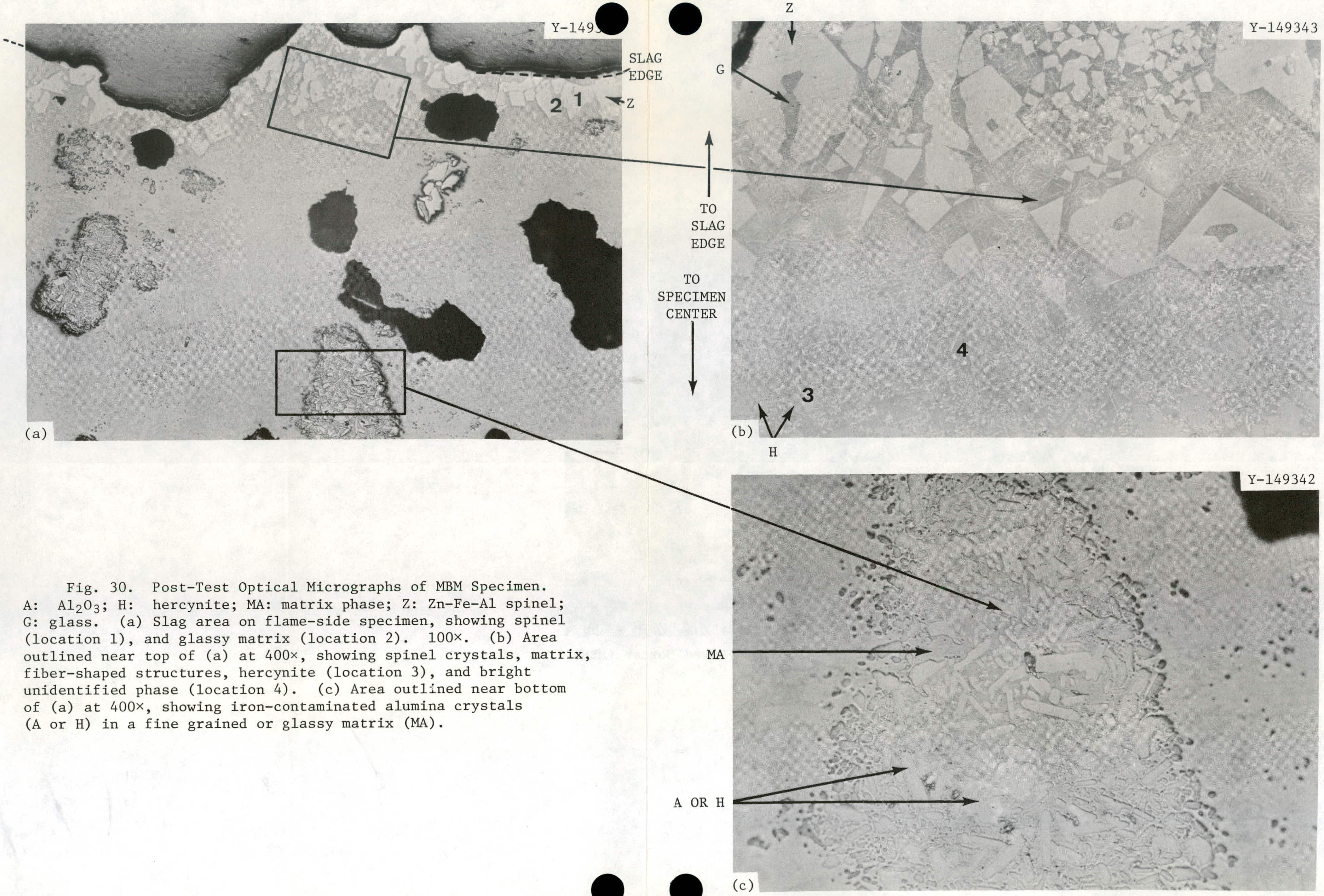

Fig. 30. Post-Test Optical Micrographs of MBM Specimen. A: Al_2O_3; H: hercynite; MA: matrix phase; Z: Zn-Fe-Al spinel; G: glass. (a) Slag area on flame-side specimen, showing spinel (location 1), and glassy matrix (location 2). 100×. (b) Area outlined near top of (a) at 400×, showing spinel crystals, matrix, fiber-shaped structures, hercynite (location 3), and bright unidentified phase (location 4). (c) Area outlined near bottom of (a) at 400×, showing iron-contaminated alumina crystals (A or H) in a fine grained or glassy matrix (MA).

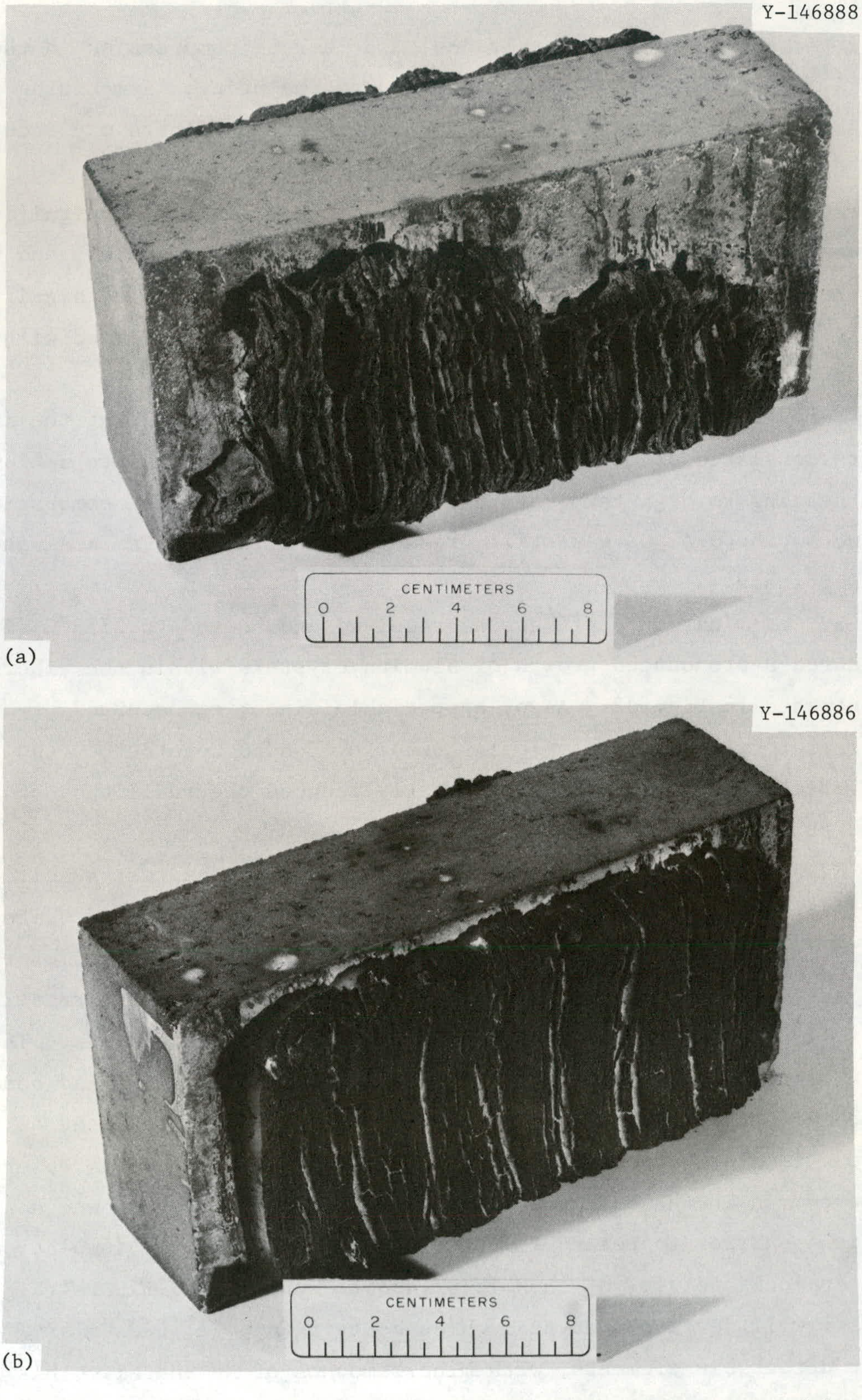

Fig. 31. Visual Appearance of HAF Specimen Post-Test. (a) Flame-side (front) of specimen. (b) Back side.

lateral shrinkage may be partly due to a lack of compression in the fibers when they were originally bonded to the brick. A mounting technique involving increased edge compression for the fibers may reduce some of these edge effects.

Chemical analysis results are presented in Table 11. Significant increases in the concentration of Fe, Si, Ca, Mg, Mn, Zn, Ni, and Cr occurred during the test. The phosphorus content increased significantly in the flame-side specimen. This result was confirmed with microprobe analyses.

X-ray diffraction examination (Table 12) indicated that the initial fibers consisted of metastable aluminas which transformed to α-Al_2O_3 upon heating to high temperatures. After exposure to the combustion products, the α-Al_2O_3 was still present in addition to Fe-Zn-Al and Fe-Al spinels.

SEM examination of fibers as-received and heated to 1375°C (2500°F) indicated a pronounced growth of alumina crystals within the fibers as illustrated in Fig. 32. Also, appreciable sintering occurred at high temperature with fibers typically becoming bonded together as shown in Fig. 32(c),(d). This sintering greatly reduced the resiliency of the fiber strips and made them quite brittle.

Exposure to the combustion atmosphere during the test resulted in the fiber surface being covered with a slag which penetrated quite deeply into the insulation. Figure 33 illustrates the nature of this slag as viewed directly on the hot face. In this case, the reaction layer is not completely dense as in the dense brick specimens. The layer contains definite crystal forms which are intergrown and bonded to each other. Apparently the very low initial silica content of this fibrous insulation retards formation of the siliceous matrix observed to be common in the brick specimen, and consequently there was no physical barrier to retard impurity penetration into the insulation.

An inclined view of this layer and the underlying fibers (Fig. 34) shows a well developed crystal which contains Al, Fe, and Zn as major detectable elements, with minor amounts of Na and Ni. This cyrstal appears to be the cubic Fe-Zn-Al spinel discussed previously

Table 11. Chemical Analysis Results from HAF Specimens

Element (as oxide equiv.)	Contents (wt %)		
	Pretest[a]	Back-Side	Front-Side
L.O.I.	0.09	0.24	0.33
Al_2O_3	97.35	90.54	73.45
Fe_2O_3	0.060	2.79	5.69
SiO_2	1.50	2.10	4.35
CaO	0.16	0.70	6.60
TiO_2	0.46	0.58	0.92
P_2O_5	0.16	0.26	4.08
Na_2O	0.13	0.25	0.09
MgO	0.001	0.07	0.72
MnO	0.03	0.12	0.21
ZnO	0.001	2.0	3.0
NiO	0.002	0.30	0.50
Cr_2O_3	0.05	0.20	0.20
CuO	0.005	0.01	0.01
PbO	0.001[b]	0.003	0.003
MoO_3	0.005	0.001[b]	0.001[b]
V_2O_5	0.001[b]	0.001[b]	0.003
B_2O_3	0.003	0.003[b]	0.003[b]
BaO	0.001[b]	0.002	0.10
Ag_2O	0.001	0.0005	0.0005
Total	100.01	100.17	100.26

[a] Heated 115 hr in air at 1375°C (2500°F).

[b] Not detected. Number is minimum limit of detection.

Table 12. Results of X-Ray Diffraction Analysis of HAF Specimens

Specimen Type	Phases Present and Amounts	
	Major	Minor
As-Received	Metastable Aluminas, α-, Δ-, χ-, Al_2O_3	
Heated 115 hr In Air At 1375°C (2500°F)	α-Al_2O_3	
Back-Side, Posttest	α-Al_2O_3	Spinel
Front-Side, Posttest	α-Al_2O_3	Spinel

for other test materials. Also apparent in this figure is the prevalent coating of the individual fibers with slag-type deposits.

Characterization of the coating on the fibers is difficult, and its composition varies with depth in the sample. The hot face layer is largely converted to spinel, while a few millimeters into the insulation glassy and crystalline phases of other compositions appear. Fig. 35 shows a heavily coated group of fibers and shows a glassy area [left side, Fig. 35(c)] which EDX showed to contain large amounts of Al, Si, and Ca. The elongated crystals on the right side of the group were rich in Al with a minor level of Ca.

Ceramography and microprobe examination verified the SEM and EDX results. Figure 36 illustrates the hot face region of the specimen facing the burner. No residual fibers are observed within 1000 μm of the deposit surface. The appearance of this surface is similar to those described earlier with Fe-Zn-Al spinel crystals containing minor Na and Ni concentrations [Fig. 36(b), location 1] within a glassy matrix (location 2). However, the nature of the matrix material is quite different in this instance. At location 2 the microprobe results show major Ca and P concentrations plus minor levels of Fe and Zn. At other locations this matrix contained varying amounts of Ca, P, and Si or Al, P, Ca, Fe, Zn, and Ni. This matrix thus was a highly variable composition of calcium phosphate glass incorporating Si, Al, Fe, and Zn into its structure.

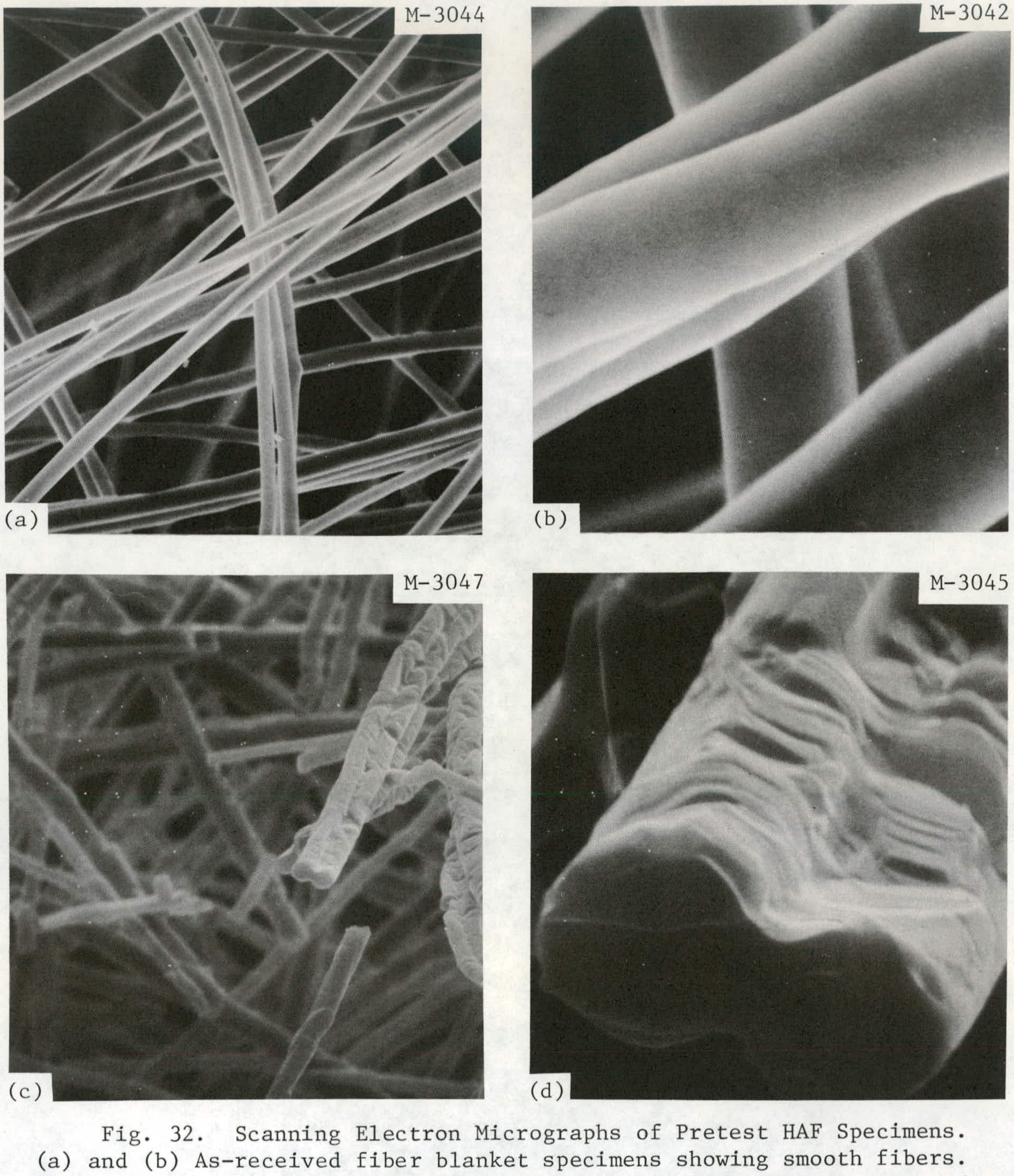

Fig. 32. Scanning Electron Micrographs of Pretest HAF Specimens. (a) and (b) As-received fiber blanket specimens showing smooth fibers. 1000 and 10,000×. (c) and (d) Grain growth and fiber sintering caused by heating to 1375°C (2500°F). 1000 and 10,000×.

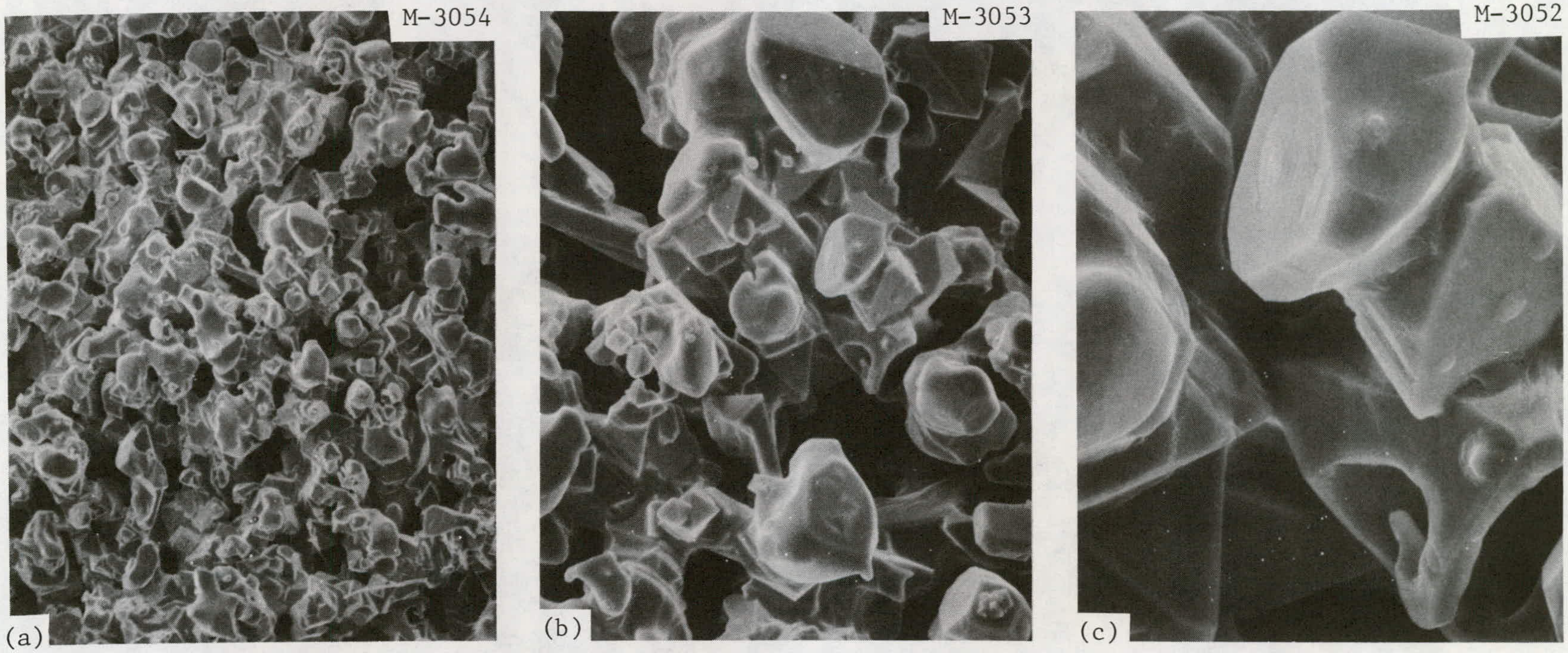

Fig. 33. Scanning Electron Micrographs of Slag Layer on HAF Flame-Side Post-Test Specimens. (a) Slag surface showing high porous layer of material. 100×. (b), (c) Same area at 300 and 1000× showing intergrowth of crytsals.

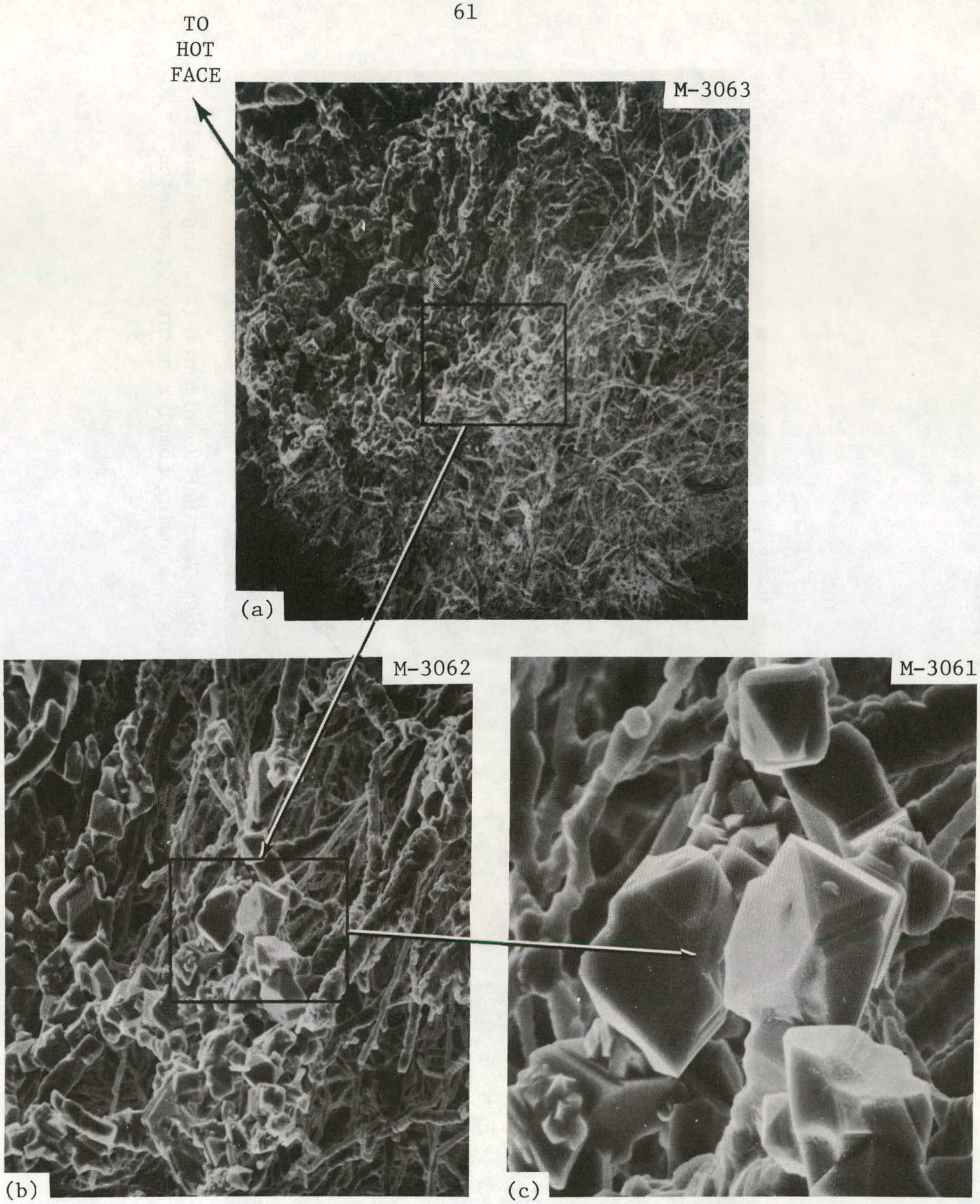

Fig. 34. Post Test Scanning Electron Micrographs of HAF Specimen, back side. (a) Inclined view of specimen indicates deep penetration of combustion products into fiber blanket. 100×. (b) and (c) Same area at 300 and 1000× shows combustion product-coated fibers and spinel crystals.

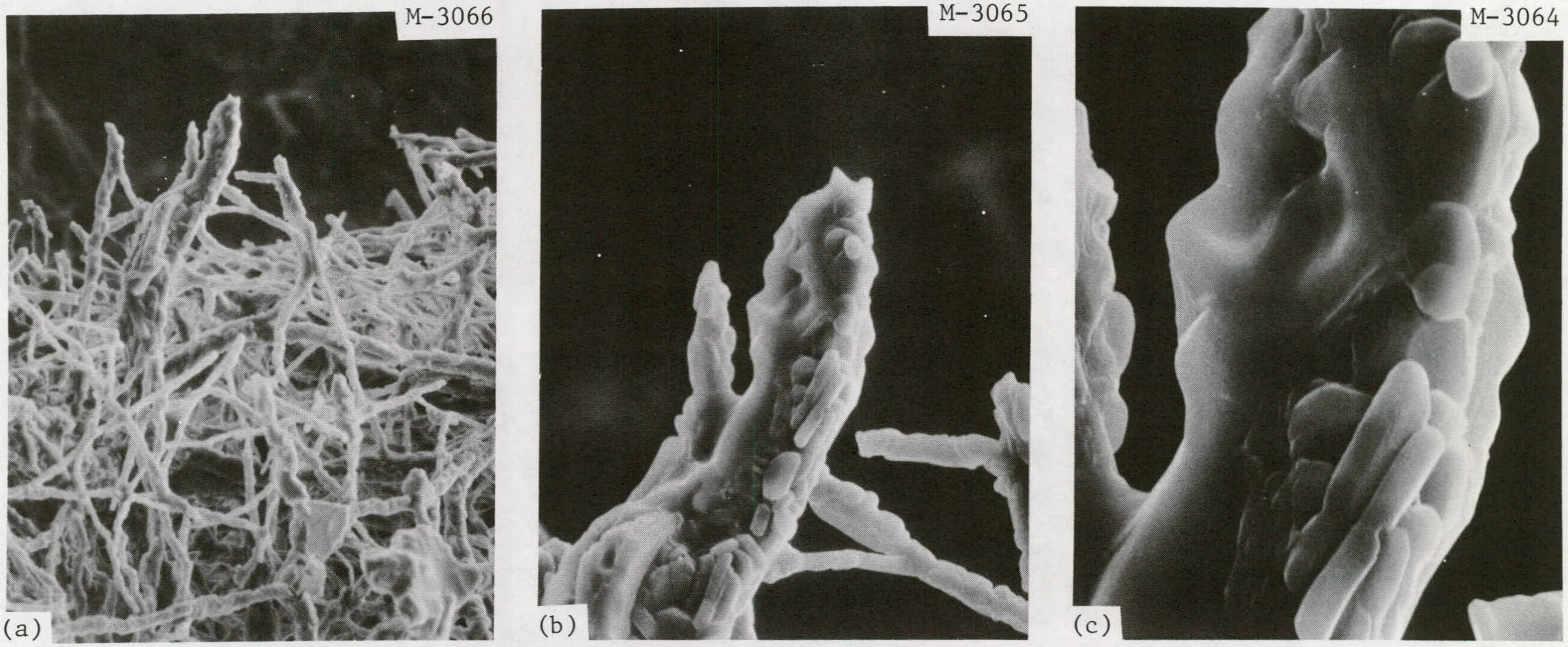

Fig. 35. Scanning Electron Micrographs of Back-Side Post-Test HAF Specimen. (a) Slag deposit coated fibers. 300×. (b), (c) Same area at 1000 and 10,000×, showing complex nature of reacted fibers.

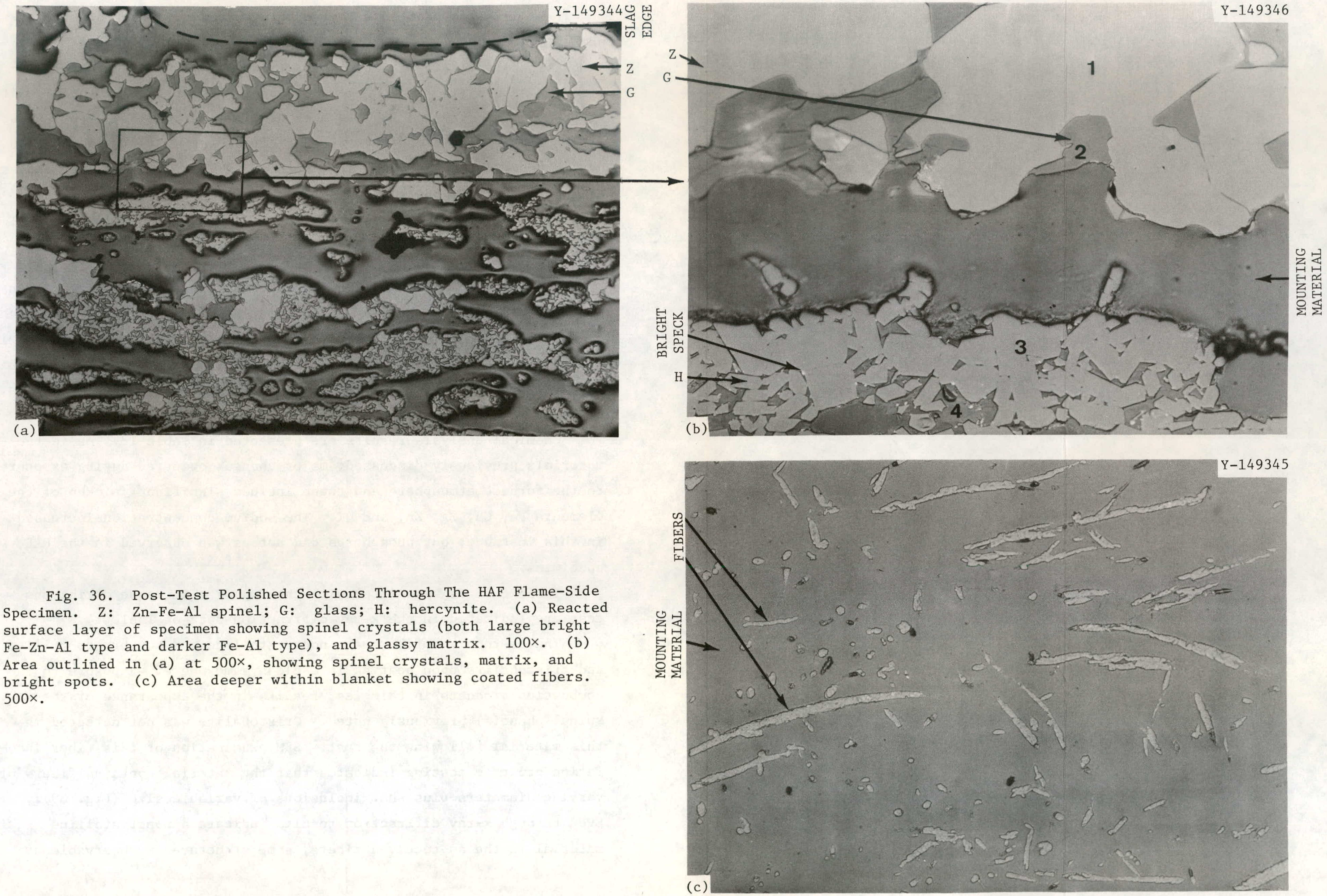

Fig. 36. Post-Test Polished Sections Through The HAF Flame-Side Specimen. Z: Zn-Fe-Al spinel; G: glass; H: hercynite. (a) Reacted surface layer of specimen showing spinel crystals (both large bright Fe-Zn-Al type and darker Fe-Al type), and glassy matrix. 100×. (b) Area outlined in (a) at 500×, showing spinel crystals, matrix, and bright spots. (c) Area deeper within blanket showing coated fibers. 500×.

Immediately behind this layer there appear two other crystalline phases [locations 3, 4, Fig. 36(b)]. The material at location 3 contains iron and aluminum in the form of hercynite while the highly reflecting specks (location 4) contain major elements Al, Si, and Ti with minor amounts of Fe and Zn. Figure 36(c) illustrates the deposit-coated fibers deeper within the network. As noted previously, these contain various species in addition to Al such as Ca, Si, and Fe. Some appear to contain only Fe and Al and may have been converted to hercynite.

Medium Alumina Fiber (MAF) Insulation

The specimens of 55% Al_2O_3 content fiber blanket are shown in the posttest condition in Fig. 37. The color ranged from dark bluish-black on the surface toward the burner to dark brown on the back side. Shrinkage was greater for these specimens than for the HAF material. In this case the fibers did not fall off the surface of the supporting bricks, although debonding occurred from the brick at the edges.

Chemical analysis results are presented in Table 13. As in the materials previously discussed, major changes occurred during exposure to the furnace atmosphere and these include significant pickup of the elements Fe, Ca, Mg, Zn, and Ni. The sodium concentration increased in this instance, but phosphorus did not as was observed in the HAF specimens.

Those changes associated with the impurity increase during the test are indicated in the x-ray diffraction data of Table 14.

The as-received fibers are noncrystalline and convert to mullite and cristobalite upon heating in a clean atmosphere. Exposure to the combustion products in this test results in the appearance of the spinel phase(s) previously noted. Cristobalite was not detected in this material following the test. SEM examination of this fiber insulation prior to testing indicates that the material contains fibers of varying diameters plus shot inclusions of variable size (Fig. 38). Even through x-ray diffraction results indicate a noncrystalline material in the as-received fibers, some structure is observable at

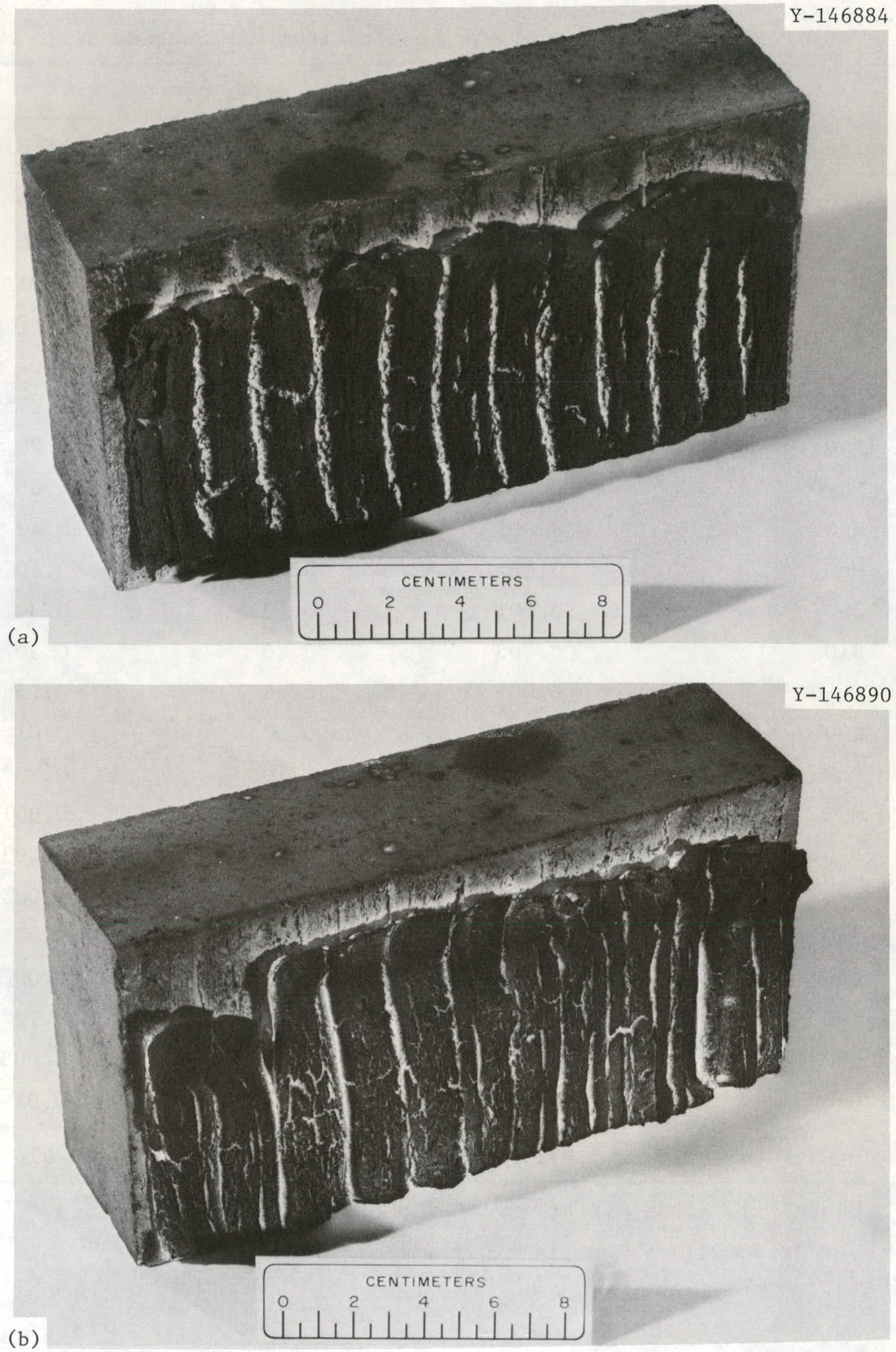

Fig. 37. Visual Appearance of MAF Specimens Post-Test. (a) Flame-side. (b) Back side.

Table 13. Chemical Analysis Results from MAF Specimens

Element (as oxide equiv.)	Contents (wt %)		
	Pretest[a]	Back-Side	Front-Side
L.O.I.	0.02	0.27	0.35
Al_2O_3	54.30	51.69	47.90
Fe_2O_3	0.15	2.80	3.91
SiO_2	44.63	42.00	41.67
CaO	0.003	0.37	3.04
TiO_2	0.031	0.040	0.075
P_2O_5	0.10[b]	0.10[b]	0.20
Na_2O	0.62	2.22	1.65
MgO	0.001	0.001	0.42
MnO	0.001	0.03	0.10
ZnO	0.001[b]	0.10	0.30
NiO	0.003	0.20	0.30
Cr_2O_3	0.005	0.20	0.15
CuO	0.005	0.003	0.01
PbO	0.002	0.10	0.10
MoO_3	0.03	0.001[b]	0.001[b]
V_2O_5	0.001[b]	0.001	0.003
B_2O_3	0.005	0.003[b]	0.003
BaO	0.001[b]	0.001[b]	0.02
Ag_2O	0.002	0.0005	0.0005
K_2O	0.16	0.20	0.12
SnO_2	0.001[b]	0.002	0.003
CoO	0.001[b]	0.003	0.01
Total	99.97	100.24	100.14

[a] Heated 115 hr on air at 1375°C (2500°F).

[b] Not detected. Number is minimum limit of detection.

Table 14. Results of X-Ray Diffraction Analysis of MAF Specimens

	Phases Present and Amounts	
Specimen Type	Major	Minor
As-Received	Glassy	
Heated 115 In Air At 1375°C (2500°F)	Mullite	Cristobalite
Back-Side, Posttest	Mullite	Spinel
Front-Side, Posttest	Mullite	Spinel

high magnification [Fig. 38(b)] which is similar to the morphology of needle-shaped mullite. EDX analysis of various fibers and shot inclusions indicate only Al and Si are present in major amounts, with trace levels of K occasionally detected.

After completion of the test, the surface is covered with a slag deposit considerably denser than the deposit on the HAF material, which contained less initial SiO_2 than this MAF insulation. This surface is seen to be covered with blocky structures [Fig. 39(a),(b)], some with triangular geometry capped by mounds of a glassy phase [Fig. 39(a),(c)]. Immediately underneath the dense surface layer are well-defined crystals of the Fe-Zn-Al spinel which contains minor amounts of Na and Ni [Fig. 39(b)]. Major elements in the mounds include Al, Si, Ca, Fe, and Zn with lesser amounts of Na, Ni, Cr, and Pb. The coated fibers and shot [Fig. 39(d),(e)] contain Al, Si, Fe, Ca, Zn, Na, Ni, Cr, and Pb.

Ceramography and microprobe evaluation supported the SEM and EDX results. Figure 40 depicts the surface region of the flame-side specimen of the MAF insulation. Numerous phases exist in the sample. The large dense crystals are Fe, Zn, and Al oxide (spinel) containing minor amounts of Na and Ni. The long needle-shaped crystals are hercynite ($FeAl_2O_4$). Very close to the surface, the matrix appears glassy and is mostly calcium aluminosilicate glass with Fe, Ti, Zn, S, and P. Just below this surface, remnants of original fibers appear, and under higher

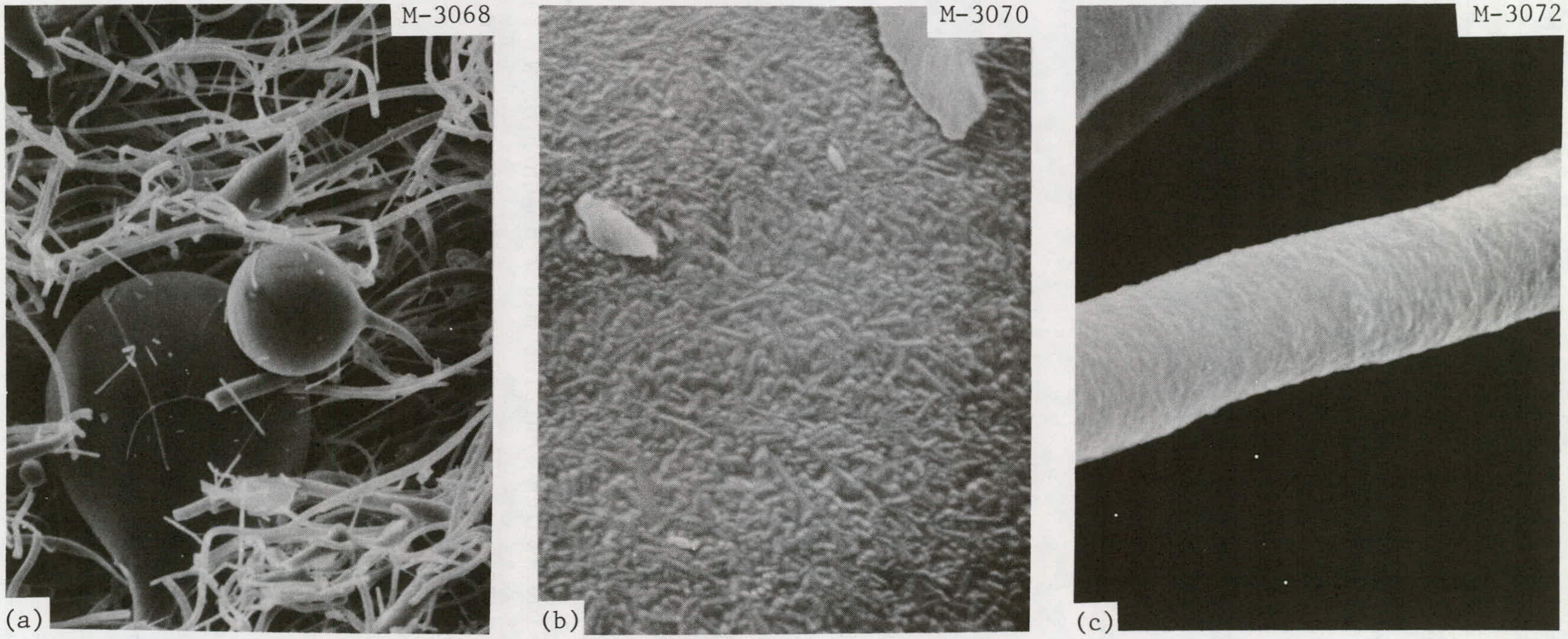

Fig. 38. Scanning Electron Micrographs of Pretest MAF Specimen. (a) Representative area of as-received specimen showing varying fiber diameter, "shot" inclusions. 300×. (b) Very high magnification of "shot" particle in (a) showing structure. 10,000×. (c) Representative fiber after heating 115 hr in air at 1375°C (2500°F) showing essentially no change from as-received condition. 10,000×.

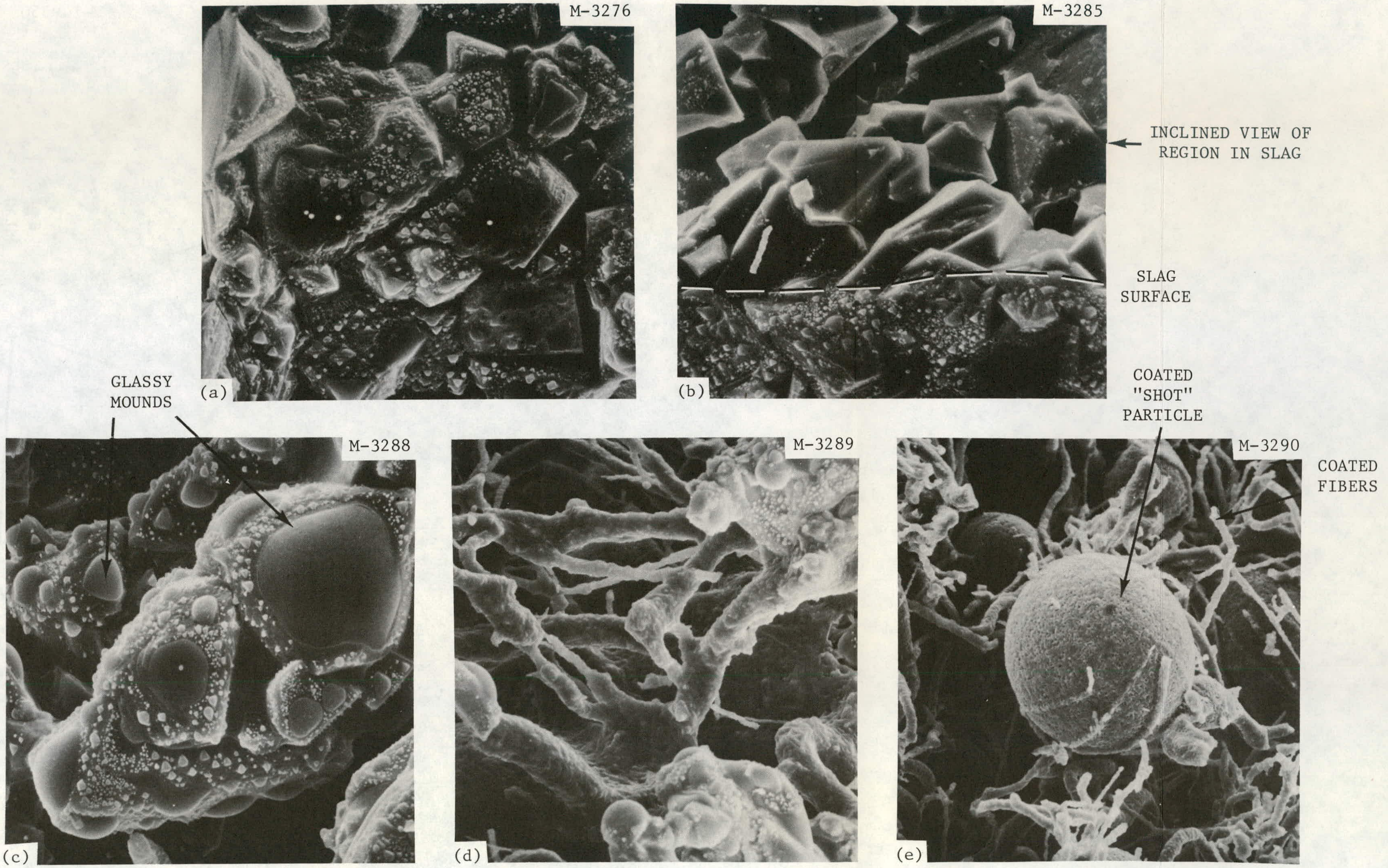

Fig. 39. Scanning Electron Micrographs of Post-Test MAF Specimens. (a) Surface layer, flame-side specimen showing blocky structure, triangular crystal faces, glassy mounds. 1000×. (b) Tilted view adjacent to (a), showing crystals underlying surface deposit. 1000×. (c) Surface layer, back side specimen showing shape of mounds. 1000×. (d) Same specimen as (c), tilted to show coated fibers underneath surface deposit. 500×. (e) Same specimen as (c), showing coated fibers and "shot." 300×.

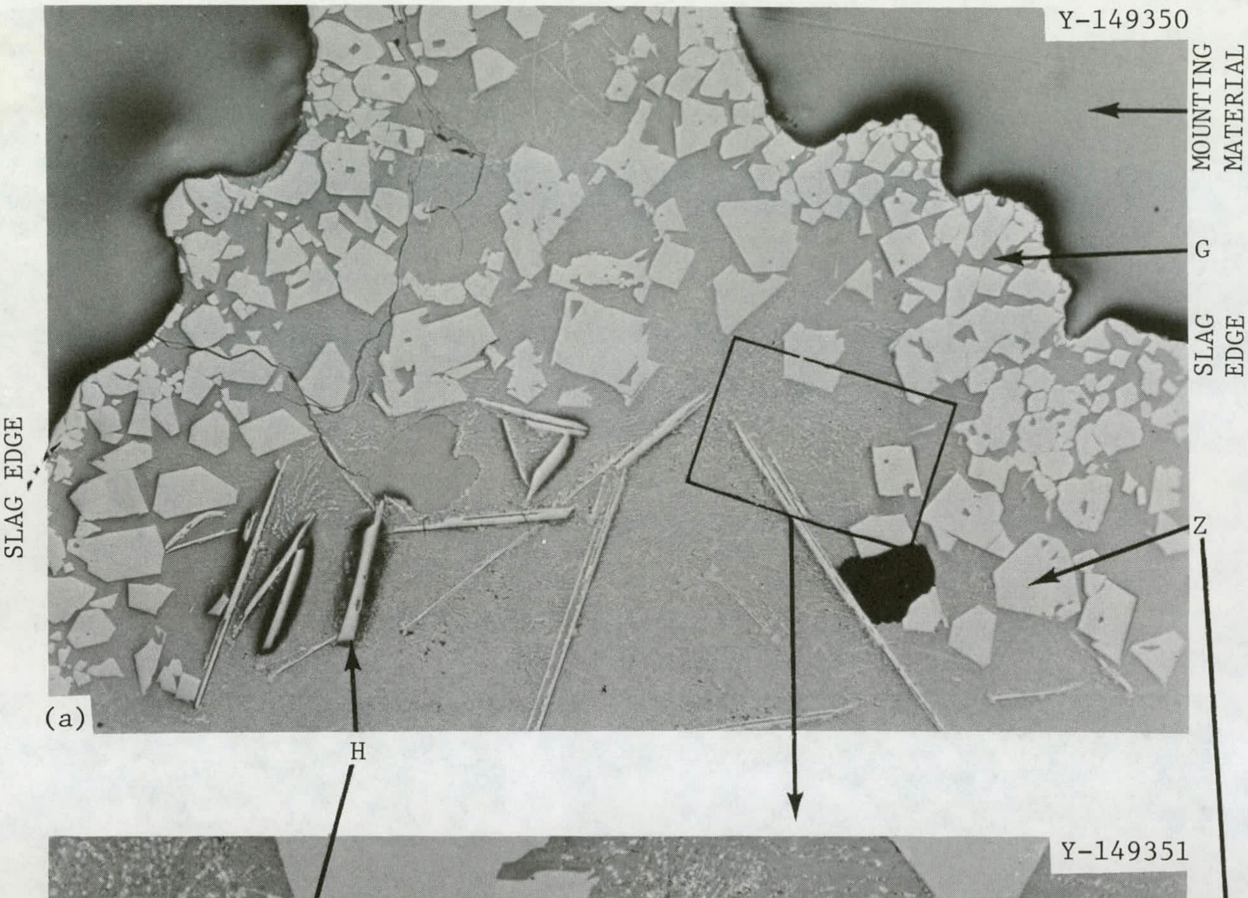

Fig. 40. Optical Micrographs of a Polished Section of Post-Test Flame-Side MAF Specimen. Z: Zn-Fe-Al spinel; G: glass; H: hercynite. (a) Hot surface region shows numerous phases present. 100×. (b) Area outlined in box in (a) at 500× shows other phases.

magnification [Fig. 40(b)] these are found to be surrounded by multiple phases. Four distinct phases were identified, denoted by locations 1-4 on Fig. 40(b). Location 1, the medium gray matrix, contains Al, Si, and Ca as major detectable elements, with minor levels of P, Fe, Zn, and Ti. The very dark areas (location 2) contain largely Al, Si, P, and Ca plus oxygen with additional smaller amounts of Fe, Mn, Zn, and Ti. Lighter gray inclusions as at location 3 contain primarily Al, Si, and Ca with minor amounts of Zn and Fe. Finally, the very reflective material at location 4 contains major amounts of Al, Si, and Fe, plus Ca, Zn, P, K, and Ti.

SUMMARY AND INTERPRETATION OF RESULTS

Summary of Results

Exposure of aluminosilicate refractories and insulations for about 500 hr at 1300-1400°C (2370-2550°F) to combustion of a domestic residual oil containing large amounts of Fe, Ca, Zn, Ni, Pb, and sulfur as impurities results in significant chemical reactions between these materials and several of the impurities. A mixed layer of crystalline and glassy reaction products is produced on the original surface. The kinetics of penetration of the various refractories and insulations by these products has not been evaluated hence their long-term physical stabilities in such an environment are presently unknown. However, the data presented in the test results section allow assessment of the relative stabilities of these ceramic materials under the condition which prevailed during the test.

Results of pre- and posttest analyses are summarized in Tables 15 and 16. Table 15 illustrates gross elemental changes which occurred in regions near the hot face of flame-side specimens during the test. This listing is based on those elements which appear to be present in sufficient quantities in the tested materials to result in generation of new phases. All of these ceramic materials have become significantly contaminated by Fe, Ca, Ni, and Zn. Those having very high initial Al_2O_3 compositions (HAB, HAF) experienced increases in Si and P contents.

Table 15. Summary of Changes in Chemical Constituents of Materials Tested in RTF Test 1

Material Designation[a]	Elements Showing Major Increases
HAB	Fe, Si, Ca, P, Mg, Zn, Ni
PBM	Fe, Ca, Mg, Zn, Ni
MBB	Fe, Ca, Na, Mg, Zn, Ni
MBM	Fe, Ca, Zn, Ni
HAF	Fe, Si, Ca, P, Mg, Mn, Zn, Ni, Cr
MAF	Fe, Ca, Na, Mg, Mn, Zn, Ni, Cr

[a] See Table 1 for explanation of designation.

Cr, Na, Mn, and Mg contents also have increased significantly along with others which usually appear in small quantities in the new phases.

Table 16 summarizes the phase assemblages determined by x-ray diffraction, SEM in conjunction with EDX, and optical microscopy in conjunction with electron microprobe analysis for all of the refractories and insulations included in this test.

The reacted surfaces of all these ceramics contained well-developed crystals of an oxide spinel containing Fe, Zn, and Al, plus minor amounts of Na and Ni. These crystals appear to have developed in the presence of a siliceous melt rich in calcium and silicon in addition to those just mentioned. Often this glassy phase contained P, S, and other trace elements. Immediately behind the layer containing these spinel crystals, hercynite was often observed. The matrix phase surrounding these crystals may be either crystalline or glassy. Slightly further back into the specimen where impurity contents are lower the original α-Al_2O_3, mullite, and cristobalite phases were observed after the test.

Interpretation of Results

The existence of the posttest phase assemblages described above can be rationalized by examination of the ZnO-Al_2O_3-SiO_2 and FeO-Al_2O_2-SiO_2 (ref. 10) phase equilibrium diagrams. These are similar in respect to all phases present with the sole exception of iron-cordierite ($2FeO \cdot 2Al_2O_3 \cdot 5SiO_2$) which does not have an analog ZnO compound.[11]

Table 16. Summary of Phases Present in Materials Tested in RTF Test 1

Material Designation[a]	Phases Initially Present			Phases Present After Test		
	Major	Medium	Minor	Major	Medium	Minor
HAB	α-Al_2O_3	Mullite		α-Al_2O_3	Mullite	Zn-Fe-Al spinel Hercynite ($FeAl_2O_4$) Glassy matrix rich in Si, Ca, Al, Fe, and Zn near hot face Crystalline silicates in cooler regions
PBM	$AlPO_4$ Mullite α-Al_2O_3			α-Al_2O_3 Mullite		Same as for HAB plus very minor $Al_2O_3 \cdot TiO_2$—$Fe_2O_3 \cdot TiO_2$ (ATFT)
MBB	Mullite		Cristobalite	Mullite		Same as for the HAB except no hercynite Cristobalite
MBM	Mullite	α-Al_2O_3		Mullite		α-Al_2O_3 Same as for HAB
HAF	Metastable aluminas			α-Al_2O_3		Fe-Zn-Al spinel Glassy silicates and phosphates rich in Ca and other impurities Hercynite Crystalline silicates in cooler regions
MAF	Glass or microcrystalline mullite			Mullite		Same as for HAB

[a] See Table 1 for explanation of designations.

The $ZnO-Al_2O_3-SiO_2$ diagram, Fig. 41, is taken from work by Bunting.[11] The figure has been redrawn and slightly revised. The dotted boundary curve between the more recently postulated[12] mullite-Al_2O_3 eutectic and Bunting's curve between mullite and Al_2O_3 has been completed. Also, an isotherm where mullite was thought by Bunting to convert to Al_2O_3 and a solid solution has been eliminated for clarity of presentation. However, the $Al_2O_3-SiO_2$ phase equilibrium diagram is yet subject to disagreement among researchers, particularly with regard to the melting behavior of mullite. For instance, Aksay and Pask[13] maintain that, as Bunting had proposed, mullite does melt incongruently. Hence we could on that basis have left the mentioned isotherm on Bunting's diagram. However, for purpose of this discussion, the actual melting behavior is of no consequence since our test temperature was well below the melting point of mullite. The remainder of the diagram is as originally presented.

Plotted on the $Al_2O_3-SiO_2$ join in Fig. 41 are initial compositions of the materials tested. The mullite-base mortar was not chemically defined as to Al_2O_3/SiO_2 ratio, but it consisted of mullite and $\alpha-Al_2O_3$ initially and so must be on the Al_2O_3-rich side of the mullite composition.

Consider now that the residual oil combustion products contain a high ratio of ZnO/SiO_2 and FeO/SiO_2 and that these are deposited continuously on the specimen surfaces. The actual ratios are unknown, but from posttest analytical results showing large increases in Zn and Fe relative to Si, we can assume they are quite high. Arbitrarily choosing a minimum mole ratio of ZnO/SiO_2 or FeO/SiO_2 of 9:1 fixes the composition of the relevant combustion products at about 90% ZnO (FeO) on the $ZnO-SiO_2$ ($FeO-SiO_2$) join. Connecting this general composition of combustion product to the original compositions yields a locus of compositions possible in the reacted materials.

When these loci are considered, possible phases present depend on local compositional values on the composition loci. Very near the surface where the combustion product concentration is highest the local concentration is within the $ZnO-Zn_2SiO_4-ZnAl_2O_4$ or $Zn_2SiO_4-ZnAl_2O_4-SiO_2$ compatibility triangles (or the FeO analogs). However, free ZnO (FeO) and Zn_2SiO_4 (Fe_2SiO_4) were never observed in our posttest specimens.

ORNL-DWG 77-20647

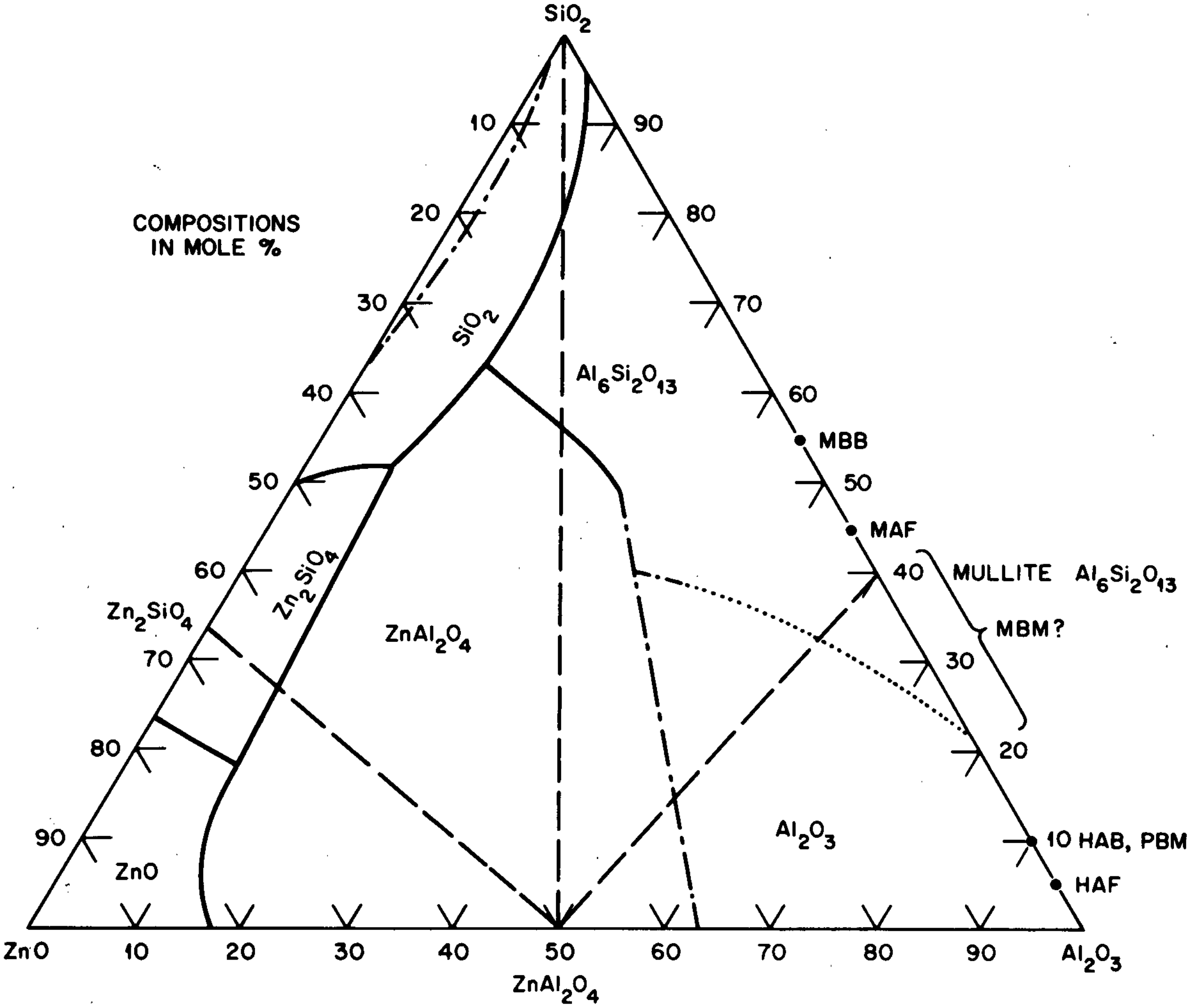

Fig. 41. ZnO-Al$_2$O$_3$-SiO$_2$ Equilibrium Diagram.

Hence these compatibility triangles are eliminated. Closer toward the alumina-rich portion of the diagrams are two more relevant composition triangles, mullite-SiO_2-$ZnAl_2O_4$ ($FeAl_2O_4$) and Al_2O_3-mullite-$ZnAl_2O_4$ ($FeAl_2O_4$). The 90% Al_2O_3 brick (HAB), phosphate-bonded mortar (PBM), 95% alumina fiber (HAF), and mullite-bonded mortar (MBM) specimens all exhibit posttest phase compositions within the latter triangle (see Table 16). Hercynite ($FeAl_2O_4$) and the Zn-Fe-Al spinel (probably a solid solution of Fe in $ZnAl_2O_4$) would coexist with Al_2O_3 as observed. The mullite-based brick (MBB) and 55% Al_2O_3 fiber (MAF) specimens would exist within the mullite-SiO_2-$ZnAl_2O_4$ ($FeAl_2O_4$) triangle. Again reference to Table 16 illustrates that at least for the MBB specimen, these three phases are present. The absence of free silica (cristobalite or tridynite) from the MAF specimen is probably due to formation of siliceous glasses with the other elements present.

The other phases observed in these specimens after testing such as the aluminosilicate crystalline and glassy phases are difficult to analyze and locate with reference to equilibrium diagrams. This is at least in part due to the presence of a wide range of solid solution possible in the Fe-Al-Si-O systems, and is further complicated by the other impurities present, particularly Ca. This element occurs largely in the glassy matrix surrounding the Zn-Fe-Al bearing spinel phases.

Some further observations relevant to this study are gleaned from literature relating to Zn and Fe attack of refractories in roofs of steel-melting arc furnaces and blast furnaces. A study of the deterioration of aluminosilicate refractories in blast furnace stacks[14] indicated that ZnO (derived from charge materials) reacts to form $ZnAl_2O_4$ and Zn_2SiO_4. Further, reacting ZnO with hercynite ($FeAl_2O_4$) leads to $ZnAl_2O_4$ formation. Hence it would appear that $ZnAl_2O_4$ is more stable than $FeAl_2O_4$ under these conditions so that the spinel crystals observed in this study are probably first formed as $ZnAl_2O_4$, with the iron then diffusing into the structure to form a solid solution. Fe was often observed by EDX and probe measurements to have diffused deeper within the ceramic test materials than had the Zn. This iron has reacted with the alumina to yield the hercynite found directly behind the surface layer.

Another similar study[15] found that reaction of ZnO with blast furnace firebrick (42% Al_2O_3) yielded $ZnAl_2O_4$ but not Zn_2SiO_4. When Zn_2SiO_4 is made to form in the laboratory, the required silica is obtained by preferential mullite decomposition rather than reaction with available free silica. This may explain our finding of free silica remaining in the MBB specimen (Table 16). Also, the presence of larger amounts of glassy matrix phases in mullite-based materials is explained by the degradation of mullite by Zn and Fe.

An examination of high alumina-content brick from electric arc-furnace steel melting roofs indicated[16,17] that CaO and FeO or Fe_2O_3 reaction leads to formation of hercynite and/or magnetite spinels, sometimes together in solid solution. Anorthite ($CaO{\cdot}Al_2O_3{\cdot}2SiO_2$) or glassy phases were produced when calcium was available. The authors determined that differences in constitution of reaction phases and the extent of degradation caused by them in various refractory brick were mainly a consequence of the alumina/silica ratio. High alumina (85%) brick reacted strongly with CaO and Fe_2O_3, leading to formation of phases adversely affecting refractory performance. Lowering the alumina content provided more silica to react with the CaO and Fe_2O_3, and these brick performed better in this environment. On the other hand, very high alumina (90-95%) brick also performed well in the present test. Hence, there may exist some optimum Al_2O_3/SiO_2 ratio in brick which will yield good performance in the presence of Ca and Fe impurity without incurring the economic penalty involved with expensive, very high alumina content refractories and insulations. In our mullite-based materials we have seen similar indications. Mullite is stable in the presence of silica and $ZnAl_2O_4$ or $FeAl_2O_4$ as shown by its presence in the slag layer [see for instance Fig. 24(b)]. The interlocking nature of the needle-shaped crystals holds the silicate melt matrix in place and provides a diffusion barrier against further ingress of impurities. Consequently, this brick seemed to perform no worse than the higher alumina brick under the conditions of this test.

A further factor involved in slag penetration into refractories is the open porosity. Our observations of depth of attack into the test specimens are in accord with the common knowledge that the lower the open porosity, the slower is the penetration under fixed conditions. This was very obvious in comparing, for instance, the behavior of HAB brick and PBM mortar specimens of similar composition: the more porous mortar exhibited a much deeper reacted zone. The fiber specimens are, in this respect, nearly the worst possible case since they consist of mostly open porosity and rely on this characteristic to provide their relatively low thermal conductivities. The more highly siliceous mullite-based fibers (MAF) performed as well as if not better than the much more expensive higher alumina content fibers in this test because a dense surface layer was formed on the MAF specimen. For optimal physical stability in such situations as these, the cheaper mullite-based fibers of as high a density as tolerable by the thermal conductance design for the furnace wall should be selected for the hot face. Of course there are many processes where the MAF type of insulation cannot be employed, due to its inherently lower temperature limitations compared with the HAF type of material. A dual insulation construction could also possibly be desirable where MAF fibers are used to face a HAF construction.

There is a final point about the 95% alumina fibers. Investigations of the rate of reaction between ZnO and various types of alumina have shown[18,19] that the metastable forms react much faster to form $ZnAl_2O_4$ than do α-Al_2O_3. Perhaps the relatively poor behavior of the HAF specimens in this test (Fig. 32) is related to this fact. It would suggest that prior to exposure to residual oil combustion products of the type employed in this test, furnaces lined with this material should be heated with a clean fuel to convert the fiber to the α-Al_2O_3 form.

CONCLUSIONS

Selected aluminosilicate refractories and insulations were exposed to combustion products of a domestic residual fuel oil containing Ca, Fe, and Zn as major impurities under controlled conditions of temperature and atmosphere. Analysis of these materials after an accumulated exposure of about 500 hr at about 1375°C (2500°F) indicated that all were being degraded by the fuel oil impurities. Conclusions based on the analyses are as follows:

1. Zn, Fe, and Ca are the primary elements involved in the reactions observed in this test. Spinel phases containing Zn and Fe are formed with aluminum oxide whether it occurs as pure α-Al_2O_3 or in combination with silica as mullite. The calcium forms a glassy matrix with silica and alumina.
2. Increasing the Al_2O_3/SiO_2 ratio of refractory materials does not necessarily lead to better refractory performance under these specified conditions. An optimum level of silica may exist which will yield materials of good service life without incurring the extra expense required for very high alumina content ceramic materials.
3. Mortar materials suffer in performance compared to denser firebrick due to their porous nature, which allows easier penetration of impurity bearing gases and melts.
4. Fiber insulations are readily penetrated by combustion products, leading to detrimental reactions. The extent of penetration is determined by the material density and permeability with the denser materials being preferable for improved stability.
5. The long-term stability of fiber blanket insulations under these conditions is questionable. Large accumulations of combustion products which freely penetrate the voids between the fibers lead to continual material degradation. The denser materials (e.g., brick) form more protective surface layers and appear more suitable although their long-term usefulness should be assessed with longer tests. The desirability of a multimaterial furnace wall design in which the insulation is protected by a thin layer of denser refractory on the hot face is indicated by the results of this test.

ACKNOWLEDGMENTS

The authors wish to express their gratitude to J. F. Willmering, Jr. of the Ceramic Technology Group, ORNL, who prepared the materials, operated the refractory test facility, and performed posttest specimen preparation. Special thanks are due R. S. Crouse and T. J. Henson of the Metallography Group for the many hours they spent performing SEM, EDX, and microprobe analyses. W. H. Warwick of the Metallography Group prepared and photographed the polished sections, and O. B. Cavin provided x-ray diffraction service.

The authors also wish to express their appreciation to Gail Garbarini, Division of Industrial Energy Conservation, DOE, for her support of this program.

The manuscript was edited by Deborah Hawkins, and prepared for publication by the Technical Publications Department.

REFERENCES

1. G. C. Wei and V. J. Tennery, *Impact of Alternate Fuels on Industrial Refractories and Refractory Insulation Applications: An Assessment*, ORNL/TM-5592 (September 1976).
2. G. C. Wei, L. A. Harris, and V. J. Tennery, *Analysis of High-Duty Fireclay Refractories Exposed to Coal Combustion*, ORNL/TM-5909 (December 1977).
3. G. C. Wei and V. J. Tennery, *Effects of Alternate Fuels Report No. 2, Analysis of Basic Refractories Degraded by Residual Oil Combustion Products*, ORNL/TM-6088 (February 1978).
4. G. C. Wei and V. J. Tennery, *Effects of Alternate Fuels Report No. 3, Analysis of High-Duty Fireclay Refractories Degraded by Residual Oil Combustion Products*, ORNL/TM-6184 (April 1978).
5. *Impact of Alternate Fuels on Refractories and Refractory Insulations, Proceedings of a Seminar, Washington, D.C., September 21, 1976, Energy Research and Development Administration, Division of Industrial Energy Conservation*, ORNL/TM-5895 (May 1977).
6. *Steam, Its Generation and Use*, 37th edition, Babcock and Wilcox, New York, 1963.
7. F. A. Williams and C. M. Cawley, "Impurities in Coal and Petroleum," in *Mechanism of Corrosion by Fuel Impurities*, H. R. Johnson and D. J. Littler, Eds., Butterworths, London, 1963.
8. R. S. Tebble and D. J. Craik, *Magnetic Materials*, p. 288, Wiley-Interscience, 1969.
9. A. G. Crouch, "The Corrosion of Bauxite-Based Refractories by Products of Residual Fuel Oil Combusion," *Trans. Br. Ceram. Soc.* 69(2): 67-72 (1970).
10. E. M. Levin, C. R. Robbins, and H. F. McMurdie, *Phase Diagrams for Ceramists*, American Ceramic Society, 1964.
11. E. N. Bunting, "Phase Equilibria in the System SiO_2-ZnO-Al_2O_3," *J. Res. Nat. Bur. Stand.* 8: 279-87 (1932).

12. S. Aramaki and R. Roy, "The Mullite-Corundum Boundary in the Systems $MgO-Al_2O_3-SiO_2$ and $CaO-Al_2O_3-SiO_2$," *J. Am. Ceram. Soc.* 42: 644-5 (1959).

13. I. Aksay and J. A. Pask, "The Silica-Alumina System: Stable and Metastable Equilibria at 1.0 Atmosphere," *Science* 183: 69-71 (1974).

14. H. M. Richardson, "The Deterioration of the Refractory Linings in the Lower Stack of the Blast Furnace," pp. 349-59 in *Proceedings of the* X^{th} *International Ceramic Congress*, Stockholm, Sweden, June 12-18, 1966 (1967).

15. H. M. Richardson and G. R. Rigby, "Reaction of Zinc and Zinc Oxide with Firebricks," *Trans. Br. Ceram. Soc.* 52: 405-16 (1953).

16. E. I. Greaves and J. R. Lakin, "The Behaviour of High Alumina Bricks in Arc Furnace Roofs," pp. 367-75 in *Proceedings of the* X^{th} *International Ceramic Congress*, Stockholm, Sweden, June 12-18, 1966 (1967).

17. E. I. Greaves and J. R. Lakin, "Constitutional Changes in High-Alumina Bricks in Arc-Furnace Roofs," *Trans. J. Br. Ceram. Soc.* 70(1): 39-51 (1971).

18. T. Tsuchida, R. Furuichi, and T. Ishii, "Reactivity of η-, γ-, and α- Al_2O_3 for $ZnAl_2O_4$ Formation," *Z. Anorg. Allg. Chem.* 415: 175-84 (1975).

19. T. Tsuchida, R. Furuichi, and T. Ishii, "Reactivity of δ- and θ-Al_2O_3 for $ZnAl_2O_4$ Formation," *Z. Anorg. Allg. Chem.* 423: 180-84 (1976).

INTERNAL DISTRIBUTION

1–2. Central Research Library
3. Document Reference Section
4–5. Laboratory Records Department
6. Laboratory Records, ORNL RC
7. ORNL Patent Office
8. M. Baker
9. R. S. Carlsmith
10. G. L. Copeland
11. R. S. Crouse
12. R. G. Donnelly
13. J. I. Federer
14. W. Fulkerson
15. T. G. Godfrey
16. R. J. Gray
17–19. M. R. Hill
20. W. J. Lackey
21–22. T. S. Lundy
23. D. L. McElroy
24. L. E. McNeese
25–29. R. E. Pasto
30. H. Postma
31. M. W. Rosenthal
32–56. V. J. Tennery
57. S. M. Tiegs
58. T. N. Tiegs
59. D. B. Trauger
60. G. C. Wei
61. R. W. Balluffi (consultant)
62. P. M. Brister (consultant)
63. W. R. Hibbard (consultant)
64. N. E. Promisel (consultant)

EXTERNAL DISTRIBUTION

65. D. Allen
Southern Portland Cement Co.
P. O. Box 937
Victorville, CA 92305

66. E. M. Anderson
Babcock and Wilcox Co.
P. O. Box 1260
Lynchburg, VA 24505

67. R. W. Anderson
Diversified Insulation, Inc.
P. O. Box 188
Hamel, MI 55340

68. Janet E. Bailey
Ford Motor Company
Glass Technical Center
25500 West Outer Drive
Lincoln Park, MI 48146

69. B. H. Baker
ARMCO Steel Corp.
Res. Center South
Middletown, OH 45043

70. W. T. Bakker
Fossil Energy Div.
Department of Energy
20 Massachusetts Ave., NW
Washington, DC 20545

71. S. Banerjee
General Refractories Co.
P. O. Box 1673
Baltimore, MD 21203

72. L. Baumer
Ownes-Illinois, Inc.
P. O. Box 1035
Toledo, OH 43666

73. N. Bernoth
C-E Refractories Co.
Box 828
Valley Forge, PA 19482

74. J. M. Bevilacqua
Carborundum Co.
P. O. Box 808
Niagara Falls, NY 14302

75. D. R. Bissell
Drexel Refractories Co.
Box 50
Kittanning, PA 16201

76. J. A. Bonar
Carborundum Co.
Niagara Falls, NY 14302

77. A. Brown
General Motors Corp.
GM Technical Corp.
Manufacturing Development
Warren, MI 48090

78. B. R. Brown
E.I. DuPont de Nemours & Co., Inc.
1007 Market St.
Wilmington, DE 19898

79. David Brown
Transco Inc.
700 Melvin Ave., Suite 2
Annapolis, MD 21401

80. Dr. V. L. Burdick
SUNY College of Ceramics
Alfred Univ.
Alfred, NY 14802

81. C. E. Burley
Reynolds Metal Co.
P. O. Box 27003
Richmond, VA 23261

82. F. Campbell
Babcock and Wilcox Co.
Box 923
Old Savanna Rd.
Augusta, GA 30903

83. S. C. Carniglia
Kaiser Aluminum & Chemical Corp.
P. O. Box 870
Pleasonton, CA 94566

84. A. N. Copp
Basic Refractories
(Sub. of Basic, Inc.)
845 Hanna Bldg.
Cleveland, OH 44115

85. J. A. Crookston
A. P. Green Refractories Co.
Green Blvd.
Mexico, MO 65265

86. M. S. Crowley
Standard Oil Co. (Indiana)
Naperville, IL 60540

87. L. J. Davies
Canadian Refractories Div.
Dresser Industries Canada LTD.
P. O. Box 1750, Station B
Montreal, Quebec, Canada
113B3L3

88. W. J. Englert
PPG Industries Corp.
Melting and Forming Lab.
Ferry St.
Creighton, PA 15030

89. C. R. Enoch
Resco Products, Inc.
Box 108
Norristown, PA 19404

90. W. X. Fay
General Refractories Co.
50 Monument Rd.
Bala-Cynwyd, PA 19004

91. M. P. Fedock
Republic Steel Corporation
Research Center
6801 Brecksville Road
Cleveland, OH 44131

92. A. D. Fentzke
Emhart Corp.
Hartford Div.
Box 2809
Hartford, CT 06101

93. L. E. Ferreira
Interpace Corp.
Corporate Headquarters
Box 1111
Parsippany, NJ 07054

94. R. E. Ferris
Kaiser Res. Center
Box 870
Pleasanton, CA 94566

95–104. G. Garbarini
Division of Industrial
Energy Conservation
Department of Energy
20 Massachussetts Ave., NW
Washington, DC 20545

105. H. H. Greene
Ohio Lime Co.
128 E. Main St.
Woodville, OH 43469

106. Richard Grekrila
Res. Center
Westinghouse Electric Corp.
Beulah Rd.
Pittsburgh, PA 15235

107. F. Hamel
Gulf Research and Development Co.
P. O. Box 2038
Pittsburgh, PA 15230

108. R. S. Harris
Anchor Hocking Co.
Lancaster, OH 43135

109. Douglas Harvey
Department of Energy
20 Massachusetts Ave., NW
Washington, DC 20545

110. S. P. Hepburn
ICI Fiber Materials
Concord Pike and New Murphy Rd.
Wilmington, DE 19849

111. J. P. Holt
Valley Minerals Products
915 Olive St.
St. Louis, MO 63101

112. A. V. Illyn
Babcock and Wilcox Co.
P. O. Box 923
Augusta, GA 30903

113. H. L. Johns
Zircoa Products
31501 Solon Rd.
Solon, OH 44139

114. K. K. Kappmeyer
Applied Res. Lab.
United States Steel Corp.
Monroeville, PA 15146

115. R. V. Kilgore
Gunning Refractories Co.
(Sub. of BMI, Inc.)
Box 38
Pedro, OH 45659

116. W. D. Kingery
Dept. of Materials Science and
Engineering
M.I.T.
Cambridge, MA 02139

117. Charles W. Kistler, Jr.
Battelle Columbus Laboratories
505 King Avenue
Columbus, OH 43201

118. L. Krietz
Plibrico Co.
1800 N. Kingsburg St.
Chicago, IL 60614

119. L. J. Kuhlman
Monsanto Co.
800 N. Lindbergh Blvd.
St. Louis, MO 63166

120. R. G. LaBar
Alcoa Res. Labs.
Aluminum Co. of America
Alcoa Center, PA 15069

121. Richard A. Landy
North American Refractories Co.
Curwensville, PA 16833

122. J. Langensiepen
Brockway Glass Co.
Central Lab.
Brockway, PA 15824

123. D. H. Larson
Inst. of Gas Technology
3424 S State Street
IIT Center
Chicago, IL 60616

124. F. A. Layne
Gem Refractories Co.
16th and Georgia St.
Sebring, OH 44672

125. R. Limes
Republic Steel Corp.
1441-T Republic Bldg.
P. O. Box 6778
Cleveland, OH 44101

126. C. Lindsay
Tennessee Valley Authority
303 Union Bldg.
Knoxville, TN 37902

127. D. E. McBride
Zircoa
31501 Solon Rd.
Box 39217
Cleveland, OH 44139

128. J. R. McGaughey
Bickley Furnaces, Inc.
550 State Road
Philadelphia, PA 19114

129. T. D. McGee
Iowa State University
Materials Sciences and Engineering Dept.
Ames, IA 50010

130. R. W. Marshell
North American Manufacturing Co.
4455 E 71st St.
Cleveland, OH 44105

131. F. M. Maupin
A.P. Green Refractories Co.
Green Blvd.
Mexico, MO 65265

132. W. Mead
Temtek-Allied Div.
Ferro Corp.
One Erieview Plaza
Cleveland, OH 44114

133. E. D. Miller
Lava Crucible-Refractories Co.
1045 Oliver Bldg.
Pittsburgh, PA 15222

134. J. I. Moates
General Shale Products Corp.
P. O. Box 3547, C.R.S.
Johnson City, TN 37601

135. R. J. Moffat
Pullman-Swindell
(Div. of Pullman, Inc.)
441 Smithfield St.
Pittsburgh, PA 15222

136. J. E. Moore
Kaiser Refractories Co.
(Div. of Kaiser Aluminum and Chemical Corp.)
P. O. Box 47
Columbiana, OH 44408

137. A. Moser
A. Moser, Inc.
5700 SW 7th St.
Plantation, FL 33317

138. J. E. Neal
Johns-Manville Corp.
Box 5108, Greenwood Plaza
Denver, CO 80217

139. R. Neeley
Chattanooga Glass Co.
400 W 45th St.
Chattanooga, TN 37410

140. J. A. Nelson
University of Illinois
Urbana, IL 61801

141. R. E. Nelson
C-E Minerals Co.
901 E 8th Ave.
King of Prussia, PA 19406

142. William S. Netter
Monsanto Company
800 N. Lindbergh Blvd.
St. Louis, MO 63166

143. D. Olenchut
Jones and Laughlin Steel Corp.
3A, Gateway Center
Pittsburgh, PA 15230

144. H. Orr
Trane Thermal Co.
Brook Rd.
Conshohocken, PA 19428

145. J. Osborne
Div. of Industrial
Energy Conservation
Department of Energy
20 Massachusetts Ave., NW
Washington, DC 20545

146. Roger C. Oxford
Babcock and Wilcox Co.
P. O. Box 923
Augusta, GA 30903

147. P. Papa
Cornhart Refractories Co.
1600 W Lee St.
Louisville, KY 40210

148. J. D. Parsons
Chicago-Wellsville Fire Brick Co.
1467 Elston Ave.
Chicago, IL 60622

149. G. Passell
AFC Corp.
Canfield, OH 44406

150. C. M. Pelanne
Johns-Manville Corp.
Box 5108
Denver, CO 80217

151. S. C. Porter, Jr.
Globe Refractories Co.
(Div. of C-E Refractories Co.)
Box D
Newell, VA 26050

152. G. V. Prible
C-E Refractories Co.
(Div. of Combustion Engineering,
Inc.)
Box 828
Valley Forge, PA 19482

153. C. J. Ranhke
Power Train and System Research
Ford Motor Co.
20,000 Rotunda Drive
Dearborn, MI 48121

154. P. H. Reed
New Castle Refractories Co.
Box 471
New Castle, PA 16103

155. R. Reeds
John Zink Co.
4401 S. Peoria St.
Tulsa, OK 74105

156. D. M. Rice
Davis Fire Brick Co.
Box 235
Oak Hill, OH 45456

157. R. Rose
H. K. Porter Co.
Porter Bldg.
601 Grant St.
Pittsburgh, PA 15219

158. R. P. Ross
Glasrock Products, Inc.
2210 Marietta Blvd., NW
Atlanta, GA 30318

159. G. R. Rowland
Hartford Refractories, Emhart
Corp.
P. O. Box 2809
Hartford, CT 06101

160. C. K. Russell
Res. Center
United States Steel Corp.
125 Jamison Lane
Mail Stop 43
Monroeville, PA 15146

161. E. C. Sargent
Kolb Refractories Co.
Box 95
East Greenville, PA 18041

162. M. Savitz
Department of Energy
20 Massachusetts Ave., NW
Washington, DC 20545

163. B. L. Schmidt
Anchor Hocking Co.
Lancaster, OH 43130

164. F. E. Schmidt
E.I. duPont de Nemours & Co., Inc.
Experimental Station
Bldg. 304
Wilmington, DE 14898

165. W. E. Scruggs
Monsanto Co.
800 N. Lindbergh Blvd.
St. Louis, MO 63166

166. R. L. Shultz
Armco Steel Corp.
Research Center South
Middletown, OH 45043

167. H. D. Smith
Wellsville Fire Brick Co.
Highway 19W
Wellsville, MO 63384

168. T. E. Smith
Southern Div.
Martin-Marietta Cement Co.
1800 Daniel Bldg.
Birmingham, AL 35223

169. W. J. Smothers
Homer Res. Labs.
Bethlehem Steel Corp.
Bethlehem, PA 18016

170. R. R. Smyth
FluiDyne Engineering Co.
5900 Olson Memorial Highway
Minneapolis, MN 55422

171. Gordon E. D. Snyder
General Refractories Co.
U.S. Refractories Div.
600 Grant St., RM 3000
Pittsburgh, PA 15219

172. I. Snyder
Dow Chemical Co.
2020 Dow Center
Midland, MI 48640

173. D. Stefl
Freeport Brick Co.
Drawer F
Freeport, PA 16229

174. D. F. Stock
Harbison-Walker Refractories Co.
Dresser Industries, Inc.
Two Gateway Center
Pittsburgh, PA 15222

175. W. E. Swearingen
Koppers Co., Inc.
Pittsburgh, PA 15219

176. Larrie H. Sweet
Manager Technical Development
Carborundum Co.
P. O. Box 808
Niagara Falls, NY 14302

177. C. A. Taylor
Shell Oil Co.
1 Shell Plaza, Box 2463
Houston, TX 77001

178. C. H. Taylor
National Crucible Co.
Queen St. and Mermaid Lane
Philadelphia, PA 19118

179. E. A. Thomas
Charles Taylor Div.
NL Industries, Inc.
8361 Broadwell Road
P. O. Box 44040
Cincinnati, OH 45244

180. C. J. Thompson
Bartlesville Energy Res. Center
P. O. Box 1398
Bartlesville, OK 74003

181. L. J. Trostel, Jr.
Norton Co.
One New Bond St.
Worcester, MA 01606

182. B. S. Tucker
The Refractories Inst.
1102 One Oliver Plaza
Pittsburgh, PA 15222

183. R. Van der Linden
Johns-Manville Products Corp.
Box 5108
Denver, CO 80217

184. M. L. Van Dreser
Center for Technology
Kaiser Aluminum and Chemical Corp.
Box 870
Pleasanton, CA 94566

185. Theodore Vojnovich
Res. Labs.
Westinghouse Electric Corp.
Beulah Rd.
Pittsburgh, PA 15235

186. R. L. Walter
H. J. Heinz Co.
P. O. Box 57
Pittsburgh, PA 15230

187. R. F. Whitford
North American Refractories Co.
1012 National City E 6th Bldg.
Cleveland, OH 44114

188. R. D. Whiting
Coors Porcelain Co.
600 9th St.
Golden, CO 80401

189. R. Wilcox
Chevron Res. Center
225 Bush St.
San Francisco, CA 94120

190. J. R. Wilson
Shell Development Co.
Box 1380
Houston, TX 77001

191. J. Wosinsky
Corning Glass Works
Box 432
Corning, NY 14830

192. Russell L. Yeckley
Harbison-Walker Refractories
2 Gateway Center
Pittsburgh, PA 15222

193. S. Young
Babcock and Wilcox Co.
Old Savanna Rd.
Box 923
Augusta, GA 30903

194. C. E. Zimmer
Babcock and Wilcox Co.
Lynchburg, VA 24505

195–196. Research and Technical Support Division
Oak Ridge Operations Office
Department of Energy
P. O. Box E
Oak Ridge, TN 37830

197–223. Technical Information Center
P. O. Box 62
Oak Ridge, TN 37830